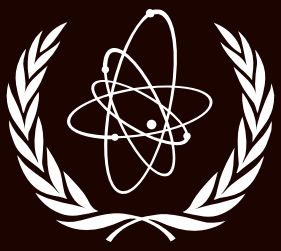

IAEA

International Atomic Energy Agency

Hands-on Training Courses Using Research Reactors and Accelerators

VIENNA, 2014

TRAINING COURSE SERIES 57

HANDS-ON TRAINING COURSES USING RESEARCH REACTORS AND ACCELERATORS

The following States are Members of the International Atomic Energy Agency:

AFGHANISTAN
ALBANIA
ALGERIA
ANGOLA
ARGENTINA
ARMENIA
AUSTRALIA
AUSTRIA
AZERBAIJAN
BAHAMAS
BAHRAIN
BANGLADESH
BELARUS
BELGIUM
BELIZE
BENIN
BOLIVIA
BOSNIA AND HERZEGOVINA
BOTSWANA
BRAZIL
BRUNEI DARUSSALAM
BULGARIA
BURKINA FASO
BURUNDI
CAMBODIA
CAMEROON
CANADA
CENTRAL AFRICAN REPUBLIC
CHAD
CHILE
CHINA
COLOMBIA
CONGO
COSTA RICA
CÔTE D'IVOIRE
CROATIA
CUBA
CYPRUS
CZECH REPUBLIC
DEMOCRATIC REPUBLIC OF THE CONGO
DENMARK
DOMINICA
DOMINICAN REPUBLIC
ECUADOR
EGYPT
EL SALVADOR
ERITREA
ESTONIA
ETHIOPIA
FIJI
FINLAND
FRANCE
GABON
GEORGIA
GERMANY
GHANA
GREECE
GUATEMALA
HAITI
HOLY SEE
HONDURAS
HUNGARY
ICELAND
INDIA
INDONESIA
IRAN, ISLAMIC REPUBLIC OF
IRAQ
IRELAND
ISRAEL
ITALY
JAMAICA
JAPAN
JORDAN
KAZAKHSTAN
KENYA
KOREA, REPUBLIC OF
KUWAIT
KYRGYZSTAN
LAO PEOPLE'S DEMOCRATIC REPUBLIC
LATVIA
LEBANON
LESOTHO
LIBERIA
LIBYA
LIECHTENSTEIN
LITHUANIA
LUXEMBOURG
MADAGASCAR
MALAWI
MALAYSIA
MALI
MALTA
MARSHALL ISLANDS
MAURITANIA
MAURITIUS
MEXICO
MONACO
MONGOLIA
MONTENEGRO
MOROCCO
MOZAMBIQUE
MYANMAR
NAMIBIA
NEPAL
NETHERLANDS
NEW ZEALAND
NICARAGUA
NIGER
NIGERIA
NORWAY
OMAN
PAKISTAN
PALAU
PANAMA
PAPUA NEW GUINEA
PARAGUAY
PERU
PHILIPPINES
POLAND
PORTUGAL
QATAR
REPUBLIC OF MOLDOVA
ROMANIA
RUSSIAN FEDERATION
RWANDA
SAN MARINO
SAUDI ARABIA
SENEGAL
SERBIA
SEYCHELLES
SIERRA LEONE
SINGAPORE
SLOVAKIA
SLOVENIA
SOUTH AFRICA
SPAIN
SRI LANKA
SUDAN
SWAZILAND
SWEDEN
SWITZERLAND
SYRIAN ARAB REPUBLIC
TAJIKISTAN
THAILAND
THE FORMER YUGOSLAV REPUBLIC OF MACEDONIA
TOGO
TRINIDAD AND TOBAGO
TUNISIA
TURKEY
UGANDA
UKRAINE
UNITED ARAB EMIRATES
UNITED KINGDOM OF GREAT BRITAIN AND NORTHERN IRELAND
UNITED REPUBLIC OF TANZANIA
UNITED STATES OF AMERICA
URUGUAY
UZBEKISTAN
VENEZUELA
VIET NAM
YEMEN
ZAMBIA
ZIMBABWE

The Agency's Statute was approved on 23 October 1956 by the Conference on the Statute of the IAEA held at United Nations Headquarters, New York; it entered into force on 29 July 1957. The Headquarters of the Agency are situated in Vienna. Its principal objective is "to accelerate and enlarge the contribution of atomic energy to peace, health and prosperity throughout the world''.

TRAINING COURSE SERIES No. 57

HANDS-ON TRAINING COURSES USING RESEARCH REACTORS AND ACCELERATORS

INTERNATIONAL ATOMIC ENERGY AGENCY
VIENNA, 2014

COPYRIGHT NOTICE

For further information on this publication, please contact:

Physics Section
International Atomic Energy Agency
Vienna International Centre
PO Box 100
1400 Vienna, Austria
Email: Official.Mail@iaea.org

HANDS-ON TRAINING COURSES USING RESEARCH REACTORS AND ACCELERATORS
IAEA, VIENNA, 2014
IAEA-TCS-57
ISSN 1018–5518

Printed by the IAEA in Austria
May 2014

FOREWORD

The enhancement of nuclear science education and training in all Member States is of interest to the IAEA since many of these countries, particularly in the developing world, are building up and expanding their scientific and technological infrastructures. Unfortunately, most of these countries still lack sufficient numbers of well-educated and qualified nuclear specialists and technologists. This may arise from, amongst other things: a lack of candidates with sufficient educational background in nuclear science who would qualify to receive specialized training; a lack of institutions available for training nuclear science specialists; a lack of lecturers in nuclear related fields; and a lack of suitable educational and teaching materials. A related concern is the potential loss of valuable knowledge accumulated over many decades due to the ageing workforce.

An imperative for Member States is to develop and offer suitable graduate and postgraduate academic programmes which combine study and project work so that students can attain a prerequisite level of knowledge, abilities and skills in their chosen subject area. In nearly all academic programmes, experimental work forms an essential and integral component of study to help students develop general and subject specific skills. Experimental laboratory courses and exercises can mean practical work in a conventional laboratory or an advanced facility with an operational particle accelerator or research reactor often accompanied by computer simulations and theoretical exercises.

In this context, available or newly planned research reactors and particle accelerators should be seen as extremely important and indispensable components of nuclear science and technology curricula. Research reactors can demonstrate nuclear science and technology based on nuclear fission and the interaction of neutrons and photons with matter, while particle accelerators can demonstrate nuclear science and technology based on charged particle induced nuclear and atomic reactions. The extent and level of education and training offered by research reactor/particle accelerator facilities can be tailored to suit the interests of the implementing organization.

This publication is intended to provide resource material to support practical educational and training curricula in nuclear science and technology in Member States and, in particular, those activities utilizing research reactors or particle accelerators. It was prepared using the outputs of expert and consultancy meetings held in Ghana (September 2007) and in Austria (December 2009), and from various IAEA lectures and practical training courses given at the International Centre for Theoretical Physics (ICTP), Italy, and the Atominstitut, Vienna University of Technology, Austria.

The IAEA acknowledges the valuable contributions of the individual participants as well as experts who reviewed this publication, particularly N. Dytlewski (Austria). The IAEA officers responsible for this publication were A. Simon and D. Ridikas of the Division of Physical and Chemical Sciences.

EDITORIAL NOTE

This publication has been prepared from the original material as submitted by the contributors and has not been edited by the editorial staff of the IAEA. The views expressed remain the responsibility of the contributors and do not necessarily reflect those of the IAEA or the governments of its Member States.

Neither the IAEA nor its Member States assume any responsibility for consequences which may arise from the use of this publication. This publication does not address questions of responsibility, legal or otherwise, for acts or omissions on the part of any person.

The use of particular designations of countries or territories does not imply any judgement by the publisher, the IAEA, as to the legal status of such countries or territories, of their authorities and institutions or of the delimitation of their boundaries.

The mention of names of specific companies or products (whether or not indicated as registered) does not imply any intention to infringe proprietary rights, nor should it be construed as an endorsement or recommendation on the part of the IAEA.

The IAEA has no responsibility for the persistence or accuracy of URLs for external or third party Internet web sites referred to in this publication and does not guarantee that any content on such web sites is, or will remain, accurate or appropriate.

CONTENTS

1. INTRODUCTION 1

1.1. Research Reactors 1
1.2. Particle accelerators 2
1.3. Structure and safety precautions 2

2. REACTOR PHYSICS EXPERIMENTS 4

2.1. Measurement of the thermal neutron flux density 4

2.1.1. Theoretical background 4
2.1.2. Experimental theory 5
2.1.3. Experimental procedure 7
2.1.4. Recommended equipment 8
2.1.5. Safety precautions 8

2.2. Measurement of the fast neutron flux density in the core centre 8

2.2.1. Theoretical background 8
2.2.2. Experimental procedure 9
2.2.3. Recommended equipment 10
2.2.4. Safety precautions 10

2.3. Determination of the material and void feedback on reactivity 12

2.3.1. Experimental procedure 12
2.3.2. Recommended equipment 13
2.3.3. Safety precautions 13

2.4. Measurement of the absorption cross-section 14

2.4.1. Theoretical background 14
2.4.2. Experimental procedure 14
2.4.3. Recommended equipment 14
2.4.4. Safety precautions 15

2.5. Determination of the reactivity and the reactor period 15

2.5.1. Theoretical background 15
2.5.2. Experimental procedure 17
2.5.3. Recommended equipment 18
2.5.4. Safety precautions 18

2.6. Measurement of the background radiation around the operating reactor 19

2.6.1. Experimental procedure 19
2.6.2. Recommended equipment 19
2.6.3. Safety precautions 20

2.7. Critical experiment 21

2.7.1. Theoretical background 21
2.7.2. Experimental procedure 21
2.7.3. Recommended equipment 22
2.7.4. Safety precautions 22

2.8. Control rod calibration and determination of excess reactivity in the core 23

2.8.1. Theoretical background 23
2.8.2. Experimental procedure 25
2.8.3. Recommended equipment 26
2.8.4. Safety precautions 26
2.9. Calibration of the shim rod in the sub-critical region 27
2.9.1. Theoretical background 27
2.9.2. Experimental procedure 28
2.9.3. Recommended equipment 28
2.9.4. Safety precautions 29
2.10. Reactivity values of fuel elements in various core positions 29
2.10.1. Theoretical background 29
2.10.2. Experimental procedure 29
2.10.3. Recommended equipment 30
2.10.4. Safety precautions 30
2.11. Reactor power calibration and temperature coefficient of the reactivity 31
2.11.1. Theoretical background 31
2.11.2. Experimental procedure 32
2.11.3. Recommended equipment 33
2.11.4. Safety precautions 33
2.12. Demonstration of a reactor pulse with different reactivity insertion 34
2.12.1. Theoretical background 34
2.12.2. Experimental procedure 34
2.12.3. Recommended equipment 35
2.12.4. Safety precautions 35
2.13. Gamma spectroscopy of TRIGA fuel 36
2.13.1. Theoretical background 36
2.13.2. Experimental procedure 36
2.13.3. Recommended equipment 38
2.13.4. Safety precautions 38
3. REACTOR INSTRUMENTATION AND CONTROL EXPERIMENTS 39
3.1. Neutron flux density measurement using compensated ionisation chambers 40
3.1.1. Theoretical background 40
3.1.2. Experimental procedure 42
3.1.3. Safety precautions 44
3.2. Neutron Flux Density measurement with fission chambers 44
3.2.1. Theoretical background 44
3.2.2. Experimental procedure 46
3.2.3. Safety precautions 48
3.3. Neutron flux density measurement with self-powered neutron detectors 48
3.3.1. Theoretical background 48
3.3.2. Experimental procedure 51
3.3.3. Safety precautions 51

4. ACCELERATOR APPLICATIONS EXPERIMENTS 52
4.1. Stopping power of light ions in solid materials 52
4.1.1. Theoretical background 52
4.1.2. Experimental procedure 53
4.1.3. Recommended equipment 57
4.1.4. Safety precautions 57
4.2. Non-Rutherford scattering near the $^{12}C(p,p)^{12}C$ resonance energy 57
4.2.1. Theoretical background 57
4.2.2. Experimental procedure 58
4.2.3. Recommended equipment 60
4.2.4. Safety precautions 61
4.3. Measurement of the hydrogen concentration in thin films 61
4.3.1. Theoretical background 61
4.3.2. Experimental procedure 63
4.3.3. Concluding remarks 65
4.3.4. Recommended equipment 66
4.3.5. Safety precautions 66
4.4. Proton-induced gamma ray emission analysis of Na and Al 66
4.4.1. Theoretical background 66
4.4.2. Use of standards 67
4.4.3. PIGE analysis of Na and Al 68
4.4.4. Experimental procedure 70
4.4.5. Recommended equipment 70
4.4.6. Safety precautions 70
4.5. Nuclear reaction analysis of light elements 71
4.5.1. Theoretical background 71
4.5.2. Experimental procedure 72
4.5.3. Experiments and calculations 73
4.5.4. Recommended equipment 74
4.5.5. Safety precautions 75
4.6. Rutherford backscattering spectrometry of heavy element layers on a silicon substrate 75
4.6.1. Theoretical background 76
4.6.2. Experimental procedure 78
4.6.3. Energy calibration 79
4.6.4. Measurements 79
4.6.5. Data analysis 80
4.6.6. Concluding remarks 80
4.6.7. Recommended equipment 81
4.6.8. Safety precautions 81
5. ACCELERATOR NUCLEAR INSTRUMENTATION EXPERIMENTS 82
5.1. Measurement of the efficiency curve of an X ray detector 82
5.1.1. Theoretical background 82
5.1.2. Experimental procedure 85

5.1.3. Recommended equipment 87
5.1.4. Safety precautions 87
5.2. Energy and efficiency calibration of a gamma ray detector 88
5.2.1. Theoretical background 88
5.2.2. Experimental procedure 90
5.2.3. Concluding remarks 91
5.2.4. Recommended equipment 92
5.2.5. Safety precautions 92
5.3. Energy calibration of a silicon charged-particle detector 92
5.3.1. Detector choice 93
5.3.2. Measurements 95
5.3.3. Recommended equipment 96
5.3.4. Safety precautions 96
5.4. Accelerator energy calibration using the 27Al(p,γ)28Si reaction 96
5.4.1. Theoretical background 96
5.4.2. Experimental instructions 97
5.4.3. Recommended equipment 99
5.4.4. Safety precautions 99
REFERENCES 100
ABBREVIATIONS 102
CONTRIBUTORS TO DRAFTING AND REVIEW 103

1. INTRODUCTION

During the past 60 years, research reactors and particle accelerators have been instrumental in the education, training and qualification of nuclear professionals and technologists, as much of our nuclear knowledge and technology has been acquired from research and practical applications of research reactors and ion beam accelerators. The applications they provide today are mature, offering a broad range of products and services in materials science, environment, nutrition, cultural heritage, natural resources, human health, and industry, as well as manpower development opportunities in areas such as radiation protection and nuclear instrumentation.

In recognition of the potential of research reactors and ion beam accelerators to build knowledge and expertise, many Member States, particularly the developing countries, are increasing investments in this enabling technology. The impetus comes from a growing need to build and maintain the flow of nuclear knowledge and skills by providing a sufficient supply of well-trained and educated nuclear scientists, technologists and specialists. The utility of these nuclear facilities however depends on factors such as power level, operational characteristics, safety and security regulations, accessibility, available staff and other resources.

This publication provides key hands-on experiments in nuclear science and technology, being of primordial importance for the training and education of tomorrow's nuclear professionals and technologists. The publication should be regarded as a guidance document for the trainers as well as for the trainees and can be extended and/or adopted to the educational objectives of the specific training programme. The content has been compiled from various IAEA lecture and practical training courses conducted at ICTP, Trieste, Italy and Atominstitut, Vienna University of Technology, Austria.

1.1. RESEARCH REACTORS

A research reactor (RR) serves primarily as a neutron source. Many different types and power levels of RRs have been developed, and at present, a total of 246 RRs operate in 56 different countries [1]. More than 50% of these RRs are older than 40 years, and the number of operational facilities is steadily decreasing. To meet the current and future demands of industry, many of these RRs are being refurbished including the conversion from high-enriched fuel to low-enriched fuel. 70% of all operational RRs are used for education and training purposes at different levels, being the most frequent application of these facilities. Due to their inherent safety and flexibility in performing various reactor physics experiments, TRIGA-type RRs are perhaps the most often used facilities for education and training purposes. They are often located on university campuses and therefore play the major role in both undergraduate and graduate education of students.

Sections 2 and 3 of this publication describe some common standard experiments which are usually performed inside and outside the small power RR core. The described experiments have been applied many times at the 250 kW TRIGA Mark II facility, operated by the Atominstitut in Vienna, Austria. The utilization of small power RRs certainly can be increased by the implementation of these experiments as part of a comprehensive education and training (E&T) courses delivered by universities or other institutions. Section 2 describes reactor physics experiments and section 3 describes reactor instrumentation and control experiments.

1.2. PARTICLE ACCELERATORS

There are about 163 low-energy electrostatic accelerators in operation distributed over 50 countries [2]. These accelerators can be sub-divided into 4 categories: EN-FN-MP-UD[1], Pelletron®, single-ended and Tandetron™, representing the wide variety of machine technologies in use today, both modern and older design.

Much of our knowledge of the low-energy properties of the nucleus has come from using ion beams from accelerators. Nuclear reactions and particle scatterings observed from bombarding nuclei with various ion beam species over wide energy ranges have helped delineate the atomic and nuclear data and interaction mechanisms involved, and in cases where interactions are particularly strong, have spawned analytical applications which are in widespread use today. Section 4 describes key accelerator-based experiments which have become the backbone of ion beam analysis of materials, and Section 5 describes experiments utilising associated nuclear instrumentation.

1.3. STRUCTURE AND SAFETY PRECAUTIONS

The content of this publication is organised as follows. Each of the selected experiments is described with its related theoretical background and detailed experimental procedures. In addition, when applicable, templates to record and analyse data are included as a suggestion to be used for the experiments. Each experiment has a list of required equipment considered necessary to perform the experiment, as well as radiological safety issues to be aware of and precautions that need to be taken.

As experiments on RRs and particle accelerators may involve the handling of radioactive materials, the use of sealed and/or unsealed radiation sources, including some operating equipment that produces radiation, there are potential safety hazards to personnel and equipment. All personnel undertaking such activities must be fully aware of the potential safety hazards and the correct procedures to be used to minimise any risks involved. Supervising staff must be familiar with their own internal system of safety management, external safety regulations, operational limits and conditions, environmental codes of practice, etc.

Safety is a broad and encompassing area that includes emergency procedures, responsibilities, compliance with regulatory requirements, etc. It is highly recommended that a safety regime be adopted that includes training for trainers and trainees dealing with potentially hazardous scenarios and conditions. Every laboratory will have its own internal procedures of safety management or, in some cases, an umbrella system with specific safety and radioprotection functions as part of the operating RR or accelerator facility.

An effective laboratory management system should ensure safe and efficient facility operations, and ensure that all applicable regulatory and legislative requirements are satisfied at all times. If a safety management system is not in place, the minimum safety issues that should be planned for by facility managers are effective procedures for dealing with

[1] EN-FN-MP-UD are large machines built during the 1960s and 1980s. Model EN (rated terminal voltage of 5 MV), FN (7.5 MV), MP (10 MV), UD (> 10 MV, vertical Tandem).

emergencies. This includes fire, exposure to radiation, and general laboratory and industrial accidents.

It is essential that each laboratory has safeguards to ensure radiological hazards are safely and effectively managed to reduce the risk of accidents. Such hazards with RRs and accelerators include:

- Transport, handling and storage of radioactive and/or irradiated materials;
- Radiation produced from neutron or ion beam reactions with certain materials;
- Neutron or ion beam reactions inducing long half-life radioactivity in materials;
- Contaminated equipment and personnel if not correctly managed.

Facility managers should, as part of their management duties, undertake their own risk assessment based on the best local and international standards and practices. International standards provide a good scope and reference for the expectations and criteria for risk assessments. Some basic philosophies regarding safety risk management include identifying risks, assessment of their potential impacts, how the risk management strategy is controlled, and evaluating the measures put in place to reduce the risk. An assessment of the activities should consider:

- What might go wrong? What action should be taken in that case?
- Is there anything wrong with the way the experiment is being done?
- What if the personnel did something differently, how would it affect the risk?
- How could the work practice potentially cause injuries or damage?
- What hazards already exist that may contribute to the risk?
- What needs to be done in order to minimise or remove the risk?

2. REACTOR PHYSICS EXPERIMENTS

Although the below RR experiments are described in sufficient detail and in principle no additional references should be needed, the reader might find useful to consult the References [3-11] for complementary reading.

2.1. MEASUREMENT OF THE THERMAL NEUTRON FLUX DENSITY

The measurement of the thermal neutron flux density distribution in the core is of significant importance. The measured flux density values are applied for calibration of nuclear channels, assessment of absolute power, power distribution in the core, identification of hot spots and calculation of fuel burn up. It is also important to know the thermal flux density at irradiation sites from the reactor user's points of view. Since the flux density distribution is proportional to the power, one can determine the reactor power by measuring the relative flux density distribution in the reactor and the absolute flux density level in a certain reactor location. In comparison with ionization chambers or fission chambers, activation detectors which detect neutrons by induced activity are insensitive to gamma rays and can be used in locations where other detectors could not be used because of their small dimensions.

2.1.1. Theoretical background

The spatial distribution of the neutron flux density uses the diffusion approximated one group neutron balance equation:

$$-D\Delta\phi(\vec{r},t)+\Sigma_a(\vec{r})\times\phi(\vec{r},t)-k_\infty\Sigma_a(\vec{r})\times\phi(\vec{r},t)=-\frac{\partial n(\vec{r},t)}{\partial t} \quad (1)$$

Here D is diffusion coefficient, Σ_α is macroscopic absorption cross-section and k_∞ is the infinite multiplication factor of the system. The flux density ϕ is taken as zero at the extrapolated boundary of the reactor core because of its boundary conditions. For the stationary case, Eq. (1) can be transformed into

$$\Delta\phi(\vec{r})+B_m^2\times\phi(\vec{r})=0 \quad (2)$$

$$B_m^2=\frac{k_\infty-1}{L^2} \quad (3)$$

Where
L is the diffusion length;
B_g^2 is the geometric buckling; and
B_m^2 is the material buckling of the reactor system.

The solution of Eq. (2) determines the geometrical buckling while the solution of Eq. (3) determines the material buckling. For a critical reactor core:

$$B_m^2=B_g^2 \quad (4)$$

The infinite multiplication k_∞ is defined as the ratio of the number of neutrons in generation i to the number of neutrons in the preceding generation i-1. It is given as

$$k_\infty = \eta \cdot \varepsilon \cdot p \cdot f \quad , \tag{5}$$

Where

$\eta = \nu \times \frac{\Sigma_f}{\Sigma_a}$ is the reproduction factor (>1);

ε is the fast fission factor (>1);

p represents the resonance escape probability (<1); and

f is the thermal utilization factor (<1).

For a finite reactor system, the effective multiplication factor k_{eff} becomes

$$k_{eff} = k_\infty \times P_T \times P_F \quad , \tag{6}$$

Where

P_T represents the non-leakage probability of the thermal neutrons and;

P_F is the non-leakage probability of the fast neutrons.

The subject probabilities are expressed by

$$P_T = \frac{1}{1 + L^2 B^2} \qquad P_F = e^{-B^2 \tau} \quad , \tag{7}$$

where τ is the Fermi age for thermal neutrons. For a bare cylindrical core Eq. (2) is solved by

$$\phi(\vec{r}) = R(r) \times Z(z) \tag{8}$$

where

$$Z_m(z) = A_m \cos\left(\frac{m \times z \times \pi}{H}\right) \tag{9}$$

$$R_n(r) = A_n \times J_0\left(\frac{x_n r}{R}\right)$$

In Eq. (9), H represents an extrapolated height of the core, R shows an extrapolated radius of the core, J_0 is Bessel function of first kind of order zero and x_n is n^{th} zero solution of J_0. The stationary neutron flux density distribution is therefore

$$\phi(\vec{r}) = \phi_0 \times J_0\left(\frac{2.405 r}{R}\right) \cos\left(\frac{\pi z}{H}\right) \tag{10}$$

2.1.2. Experimental theory

The neutron flux density is measured by the gold foil activation method. The activation rate of a thin foil for mono-energetic neutrons is given by

$$C = N \times \sigma_a \times \phi \times d \tag{11}$$

Where C is activation rate, N is number of nuclei/cm^3, σ_a is the activation cross-section and d is the foil thickness. In the thermal region, most of the materials possess a *1/v* activation cross-section. Therefore, the activation is proportional to the neutron density

$$C = \int N \times \sigma_a(v) \times \phi(v) dv = \int N \times \frac{k}{v} n(v) v dv = k \times n \tag{12}$$

Because of the radioactive decay, some corrections are required to implement:

$$\frac{dB(t)}{dt} = C \times F - \lambda \times B(t) \tag{13}$$

Where $B(t)$ is the number of radioactive nuclei and λ is the decay constant. The second term in Eq. (13) describes those nuclei already decaying during activation since the activity is given as $A(t) = \lambda B(t)$. The time dependent activity is obtained by integrating Eq. (13):

$$A = A_\infty \left(1 - e^{-\lambda t_1}\right) \qquad A_\infty = C \times F \tag{14}$$

Here t_1 represents the activation time. For the time between end of activation and start of the measurement, the radioactive decay needs also to be taken into consideration. Therefore,

$$A = A_\infty \left(1 - e^{-\lambda t_1}\right) \times e^{-\lambda t_2} = A_\infty \times T^{-1} \tag{15}$$

Here t_2 is the decay time. In order to perform only thermal activation, a cadmium (Cd) difference measurement is required, i.e. a Cd-covered foil is activated under the same conditions, as an uncovered foil and the difference between their activities are determined. The Cd absorbs all neutrons in the thermal region (i.e. below energy of 0.4 eV). Since this value of the Cd cut-off energy is not perfectly correct, a correction is required by the Cd-correction factor F_{Cd}.

$$C_{th} = C_t - F_{Cd} \times C_{Cd} \tag{16}$$

C_t represents the activity of the uncovered foil, F_{Cd} is the cadmium-correction factor and C_{Cd} shows the activity of the Cd-covered foil. The activity measurement can be performed using a 4π–β counter.

Further, two more factors have to be taken into account. These are the self-absorption of the β radiation in the foil and the sensitivity of the counter. The self-absorption can be expressed as

$$S = \frac{\int_0^\theta e^{-dx} dx}{\theta} = \frac{1 - e^{\alpha\theta}}{\alpha\theta} \tag{17}$$

Where α is foil absorption coefficient for β rays [cm^2/g] for ^{197}Au and θ is foil thickness [g/cm^2].

The sensitivity R of the counter is determined by measuring the same gold foil twice i.e. once deposited on the sample holder of the counter giving R_1 and the other covered on the top with a second sample holder giving R_2.

$$R = \frac{R_2}{R_1} \tag{18}$$

Therefore, the activity and activation are related through

$$A = \frac{R \times F \times S \times C}{T} \tag{19}$$

Here F is the area of the foil.

If a Maxwell-Boltzmann spectrum of thermal neutrons is assumed, then activation of a foil and the thermal neutron flux density for *1/v* absorbers are connected through the following relation:

$$C = \frac{\sqrt{\pi}}{2} N \sigma_0 d \ \phi_{th} \sqrt{\frac{T_0}{T_N}} G \tag{20}$$

Where the σ is cross-section at 2200 m/s (T_0 = 293.6 K), T_N is the neutron temperature and G is the neutron self-shielding factor. For thin foils, this approximates to

$$G = \frac{1}{2N\sigma_0 d + 1} = \frac{1}{2\mu\theta + 1} \tag{21}$$

and

$$N\sigma_0 d \ \cong \ \mu.\theta$$

Here μ is the neutron mass absorption coefficient (for Au ~ 0.3 cm^2g^{-1}). If the Au foil is very thin then the thermal neutron flux density is calculated as

$$\phi = \frac{2T}{RFS\mu\theta\sqrt{\pi}G} \sqrt{\frac{T_N}{T_0}} (A_t - F_{Cd} A_{Cd}) \tag{22}$$

2.1.3. Experimental procedure

As foil material, Au foils are used with a weight of 40 mg/cm^2 and a diameter of 5 mm. The activity is measured by a 4π counter, according to

$$^{197}_{79}Au + n \rightarrow ^{198}_{79}Au \xrightarrow[2.7d]{\beta^-} {}^{198}_{80}Hg \tag{23}$$

The foil activation is carried out at low reactor power (10 W for a TRIGA Mark II reactor). The neutron flux density distribution is usually determined both in the radial and axial directions. Therefore, the foils are required to be fixed on specially designed sample holders which are inserted into the experimental holes of the grid plate. For the Cd-difference measurement in radial dimension, the Cd-covered Au foil is fixed at least 15 mm away from the uncovered foil to avoid flux depression. For the vertical flux density measurement in the central irradiation channel (in case of a TRIGA reactor), the uncovered and the covered foils are measured separately, due to lack of space. In order to obtain the same reactor power and irradiation time, two identical foils are activated, one with the Cd-covered foils and other with

the uncovered foils. All results are normalised to these standards. The reactor is brought to a power of 10 W with a fixed period of 20 s, so that the activation of the foils during the reactor start-up is also considered. All foils are counted in a 4π-counter, the counter plateau is determined first and the background of the counter has also been taken into account.

2.1.4. Recommended equipment

This experiment measures the flux density distribution and is performed in the reactor core. It needs the following equipment:

- An appropriate number of gold and cadmium foils. The weight and size of the foils can be different for different power (resulting in different flux levels) of the reactors;
- A gamma detector to measure the foil activity;
- Aluminium sample holders to attach the foils during activation;
- A contamination monitor.

2.1.5. Safety precautions

The standard regulations for control of radiation exposure in the laboratory for health and safety should be demonstrated to the experimenters. The general radiation protection safety measures for each student during this experiment are:

- Personal dosimeter for each course participant provided by the health physics group;
- Use of lab coat and gloves during the handling of irradiated foils;
- The irradiated foils should only be handled after a proper decay time;
- Spend as little time as possible in the controlled area;
- Each course participant should wash his/her hands after the completion of the experiment and should check for possible contamination using a hand-foot monitor.

2.2. MEASUREMENT OF THE FAST NEUTRON FLUX DENSITY IN THE CORE CENTRE

2.2.1. Theoretical background

Fast neutrons in a reactor core are neutrons of higher energy. The strongest source for fast neutrons is the thermal reactor core. The energy distribution in a reactor core is divided in three different energy regions: (fast energy range, the fast flux Φ_f), epithermal energy range (the epithermal flux Φ_{ep}), and thermal energy range (thermal flux Φ_{th}), which describes the neutrons in thermal equilibrium. Figure 1 shows the typical energy distribution of fission neutrons.

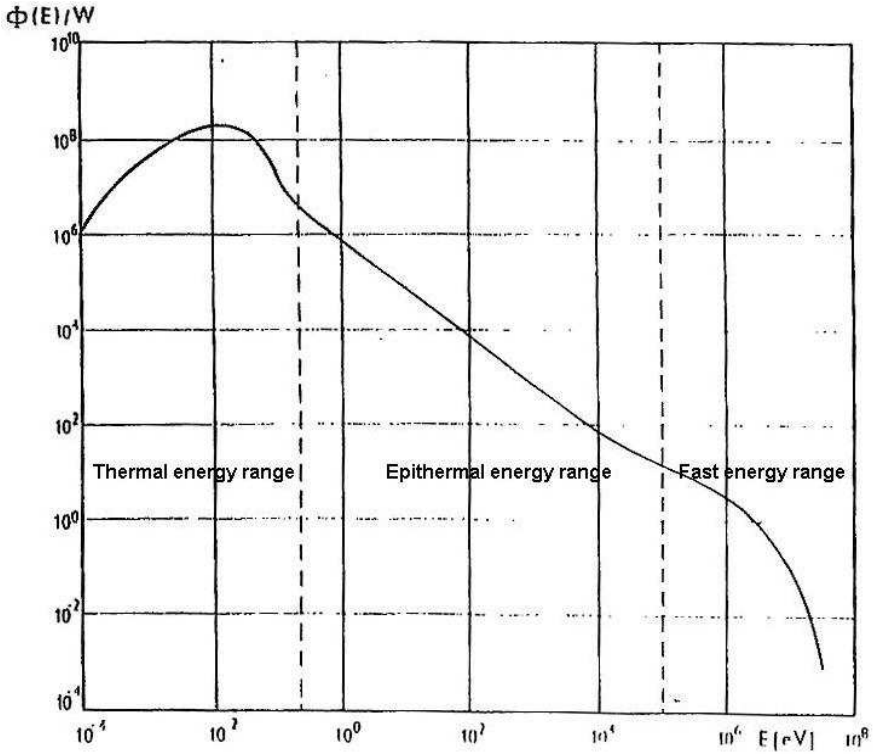

FIG. 1. Typical neutron energy spectrum in a reactor core.

$$\Phi(E)dE = \Phi_{th}\frac{E}{(kT)^2}e^{-\frac{E}{kT}}dE + \frac{\Phi_{ep}}{E}\Delta(E)dE + \Phi_f\frac{\sqrt{\pi}}{2}\frac{\sqrt{E}}{T_f}e^{-\frac{E}{T_f}}dE \quad (24)$$

Where $\Phi_{th,}$ Φ_{ep} and Φ_f represent the flux density in thermal, epithermal and fast energy range ($E_{th} < 0.2$ eV, 0.2 eV$< E_{ep} <$ 2 MeV, $E_f >$ 2 MeV) respectively. The fast and the thermal region are described through a Maxwell-Boltzmann distribution, as the epithermal region is characterised through a *1/E* distribution.

To measure the flux density of the fast neutrons, strong nuclear reactions with high threshold energies are used. This means that only neutrons above a certain energy limit contribute to the activation of the foil. Such reactions involve (n,p), (n,α), (n,f) and (n,2n) reactions. The threshold energy limit depends on the foil materials and should be between 1–20 MeV. To select a certain material, the following characteristics have to be considered.

- The distribution of the cross-section as a function of the energy must be known;
- The reaction should generate radioactive nuclei which can be clearly identified and the activity can be absolutely determined;
- The nuclei should have a half-life longer than some minutes.

It is noticeable that a precise fast flux measurement is much more complicated than a thermal flux, because the cross-sections in that region are much smaller with larger uncertainties.

2.2.2. Experimental procedure

Iron as a sensor material is selected for this experiment. Its activity can be measured in a 4π-β-detector. The effective absorption energy is high enough (6 MeV), and the half-life (2.58 h) is ideal for a short irradiation time. After the irradiation of the foils, a decay time between 30 and 60 minutes is recommended. The foil is placed with a Plexiglas sample holder in a

graphite cylinder in the centre of the core. The fast flux is then calculated with the following equation:

$$\Phi_{fast} = \frac{A_{Cd} M}{G N_A} \sigma^{-1} \left[\left(1 - e^{-\ln 2 t_{activation} / T_{1/2}} \right) e^{-\ln 2 t_{decay} / T_{1/2}} \right]^{-1} \quad (25)$$

All the relevant constants are taken from Table 1. N_A is the Avogadro number and σ is the cross-section in cm^2. The experiment is performed through the following steps:
In the experimental procedure, the iron foils are cleaned and measured for their accurate weight. Two foils are inserted into the sample holder and the water filled graphite cylinder is positioned in the core. This sample is irradiated at 3 kW for 10 minutes. This cylinder is left to cool for 2–3 hours and then measured in the 4π–β-detector. The fast flux is calculated using Eq. (25).

2.2.3. Recommended equipment

To perform this experiment on the reactor core, the following main equipment/apparatus are required:

- An appropriate number of iron foils for irradiation;
- Plexiglas sample holders and graphite cylinder to position the foils in the core centre;
- Beta or gamma detector to measure the foil activity.

2.2.4. Safety precautions

The standards safety regulations for control of internal and external radiation exposure in the laboratory for health and safety should be demonstrated to the experimenters before performing the experiment. The general radiation protection safety measures for each student during this experiment are:

- Personal dosimeter for each course participant provided by the health physics group;
- Use of lab coat and gloves during the handling of irradiated foils;
- The irradiated foils should only be handled after a proper decay time;
- Spend as little time as possible in the controlled area;
- Each course participant should wash his/her hands after the completion of the experiment and should check for possible contamination using a hand-foot monitor.

TABLE 1. THE MOST IMPORTANT PARAMETERS OF SOME RELEVANT FOIL MATERIALS FOR FAST FLUX DENSITY MEASUREMENTS

Element	$T_{1/2}$*	Reaction	n-energy	σ_{eff} [mb]	σ_{eff} [mb]	σ_{eff} [mb]	σ_{eff} [mb]	σ_{eff} [mb]	M atomic weight	G Foil weight [g]	Atoms per foil	Abundance
Ti	3.43 d	$^{47}Ti(n,p)^{47}Sc$	3.1 MeV	16.3	51.5	48	50-60	40.87				0.073
	85 d	$^{46}Ti(n,p)^{46}Sc$	3.9 MeV	10.5	520	25	15	23.5	47.867	2.214×10^{-3}	2.786×10^{19}	0.08
	44 h	$^{48}Ti(n,p)^{48}Sc$	7.6 MeV	0.272	58	10	8	10.608				0.738
Mg	15 h	$^{24}Mg(n,p)^{24}Na$	6.8 MeV	1.53	200	45	35	44.62	24.305	8.541×10^{-2}	2.116×10^{21}	0.7899
Co	10.48 m	$^{59}Co(n,\gamma)^{60}Co$	132 eV	20000	-	58	-	846	58.933	4.369×10^{-3}	4.465×10^{19}	1
	2.6 h	$^{59}Co(n,\alpha)^{56}Mn$	6.8 MeV	0.156	28.2	3	3	2.8				1
Fe	314 d	$^{54}Fe(n,p)^{54}Mn$	3.1 MeV	82.5	320	150	120-150	185.6	55.845	3.858×10^{-2}	4.161×10^{20}	0.058
	2.58 h	$^{56}Fe(n,p)^{56}Mn$	6.0 MeV	1.07	118	12	15	13.11				0.9172

N_A=Avogadro number, N_A= 6.02252×10^{23} mol^{-1}
*h = hours, d = days, m = months

2.3. DETERMINATION OF THE MATERIAL AND VOID FEEDBACK ON REACTIVITY

The operational safety of the reactor needs the information of reactivity effects on the core caused by small perturbations. In this experiment, the small perturbations are created in the Central Irradiation Channel (CIC) of the TRIGA Mark II reactor core to investigate their effects on the core reactivity. Three different kinds of perturbations are considered in this measurement. A cylindrical void (air), heavy water (D_2O) and cadmium (Cd) samples are inserted into the CIC separately and their neutronics behaviour along the axial length of the core is analysed by moving the sample in axial steps.

2.3.1. Experimental procedure

This experiment is performed in the CIC of the reactor core. Three cylindrical samples were prepared for this perturbation study. The void and heavy water sample have a typical volume of 66.42 cm^3 while the cadmium sample has a volume of 1.25 cm^3. All three samples are placed in a polyethylene bottle with negligible neutron absorption cross-section. This experiment is performed at low power of 10 W. First of all, the void sample is inserted into the CIC and moved vertically in 5 cm steps from bottom to top of the core. For each 5 cm step, the reactivity effect is recorded using the regulating control rod position. This experiment is carried out in auto-mode of the reactor control system to maintain the power at 10 W. The same procedure is repeated for heavy water and cadmium samples. Table 2 may be used as template for this experiment.

The void effects from the bottom to the top of the CIC of the TRIGA Mark II research reactor show that the void coefficient increases from bottom to centre and then decreases from centre to top. At bottom and top ends of the reactor core the void coefficient is slightly negative while in the centre of the CIC it is positive. The reason of this trend is due to the fact that both ends of the core provide leakage routes to the neutrons, while there no leakage route is available from the centre of the reactor core.

The heavy water introduces positive reactivity in the centre and negative reactivity in the bottom and top regions of the core. This is due to its relatively smaller absorption cross-section than ordinary water along the axial length of the CIC of the TRIGA Mark II reactor core.

When the cadmium capsule is moved from bottom to top of the reactor core along CIC, it shows a very strong reactivity effect due to its high absorption cross-section for thermal neutron throughout the axial length of the CIC. It is interesting to note that cadmium introduces a stronger negative reactivity in the centre than at the bottom and top ends of the core. This behaviour is due to the dominant effect of neutron absorption over the leakage.

TABLE 2. EXPERIMENTAL RESULTS OF MATERIAL AND VOID COEFFICIENT OF REACTIVITY

Position in cm (vertical)	Cylinder with H_2O (Reference)		Cylinder with H_2O and cadmium cylinder			
	Control rod	Reactivity change	Control rod	Reactivity change	Influence total / added	
0						
5						
10						
15						
20						
25						
30						
35						
40						
45						
50						

2.3.2. Recommended equipment

This experiment is performed in the CIC of the reactor core and the following main equipment/apparatus are required:

- An appropriate amount of heavy water, cadmium and light water samples;
- A dosimeter and count rate monitor for measuring dose rate and activity control;
- Sample holders (polyethylene bottles) to keep the samples in the CIC for irradiation;
- The control rod calibration curves from reactor operation group.

2.3.3. Safety precautions

This experiment is performed in the reactor hall and needs to follow the following radiation protection instructions:

- Personal dosimeter for each course participant provided by the health physics group;
- Use of lab coat and gloves during the handling of irradiated foils;
- Spend as little time as possible in the controlled area;
- Each course participant should wash his/her hands after the completion of the experiment and should check for possible contamination using a hand-foot monitor.

2.4. MEASUREMENT OF THE ABSORPTION CROSS-SECTION

One of the important applications of RR is material testing. Inside the reactor core, every sample introduces its own positive or negative reactivity according to its nuclear cross-section characteristics. Due to this fact, a reactor may be used to measure the neutron cross-section of unknown samples. This fact was also very important in the past to test the nuclear properties of different new materials, e.g. the gadolinium content in graphite, etc.

2.4.1. Theoretical background

The reactivity change due to a non-fissile material can be defined as:

$$\rho \approx -\Sigma_a V \Phi^2(r_0) \tag{26}$$

Where $\Phi(r_0)$ is the one group flux, Σ_a is the macroscopic absorption cross-section and V is the volume of the sample. To compare with different samples, the characteristics of the cross-section should be similar. If one wants to compensate the absorption in the epithermal region, the Cd-difference measurement is required.

The size of the sample in the reactor core depends on the nature of the measurement. For example, thicker samples are required to measure the effect of sample by the control system (control rods). Therefore, in case of thicker samples, the self-shielding effect must be incorporated in the measurement. To compensate the self-shielding effect, different samples with variable thickness are employed. The zero thickness effect has to then be extrapolated.

2.4.2. Experimental procedure

The reactor power is set at 10 W in an automatic mode. The reactivity of the cylindrical Cd sample (due to maximum reactivity influence) is measured. In the next step, the influence of the sample holder used for this experiment is determined. Then different samples i.e. copper foils and unknown samples (coins) with different thickness are used. Because of the low epithermal absorption no Cd-difference measurement is necessary.

The change of the reactivity in comparison with the macroscopic cross-section is defined as:

$$\frac{\Delta\rho(Cd)}{\Delta\rho(coins)} = \frac{\Sigma_a(Cd)}{\Sigma_a(coins)} \tag{27}$$

Where $\Delta\rho$ denoted change in reactivity and is extrapolated to zero thickness. This is used for evaluating the experimental results. The below Table 3 is recommended in this case.

2.4.3. Recommended equipment

This experiment is performed on the reactor core and the following main equipment/apparatus are required for these measurements:

- An appropriate number of copper and other different samples;
- Sample holders to keep the samples in the reactor core;

- A weighting balance;
- A control rod calibration curve.

TABLE 3. MEASUREMENT OF ABSORPTION CROSS-SECTION

Foil	Total thickness	Weight	Control rod	Δρ ($)
0 (only cylinder) 1 1+2 1+2+3 1+2+3+4				

2.4.4. Safety precautions

This practical exercise is performed on the reactor platform. Therefore, the following safety instructions are obligatory for each participant of the experiment:

- Personal dosimeter for each course participant provided by the health physics group;
- Use of lab coat and gloves during the handling of irradiated foils;
- Spend as little time as possible in the controlled area;
- Each course participant should wash his/her hands after the completion of the experiment and should check for possible contamination using a hand-foot monitor.

2.5. DETERMINATION OF THE REACTIVITY AND THE REACTOR PERIOD

2.5.1. Theoretical background

The reactor period is the time during which the neutrons flux density and hence the reactor power is increased by factor of e (e = 2.7). The change of the neutron flux density per unit time and unit volume follows:

$$\frac{dn}{dt} = neutrons\ \ production\ -\ leakage\ -\ absorption \tag{28}$$

The effective multiplication factor k_{eff} is given as:

$$k_{eff} = k_{\infty} \times P \tag{29}$$

Where P is a non-leakage probability and k_{eff} is the number of fission neutrons per absorbed thermal neutron with consideration of a possible leakage. These k_{eff} neutrons are now available for absorption or fission. Theoretically, the emission of one neutron is necessary to sustain the fission chain reaction and remaining neutrons (k_{eff} - *1*) are available for a power increase or to compensate for any other loss due to experiments. The expression for neutron

absorption per cm^3, per second is given by the relation $(\Sigma_a \times \phi = \Sigma_a \times n \times v)$ times the dependent neutron flux density and is given by:

$$\frac{dn}{dt} = (k_{eff} - 1) \times \Sigma_a \times n \times v \tag{30}$$

And its solution becomes:

$$n = n_0 \times e^{(k_{eff}-1)\times\Sigma_a \times v \times t} \tag{31}$$

$$n = n_0 \times e^{t/T} \tag{32}$$

Where T is the reactor period (s) and t is the chronological time (s). The reactor period from Eq. (32) is given as:

$$T = \frac{1}{\Sigma_a \times v \times (k_{eff} - 1)} = \frac{\ell}{k_{eff} - 1} \tag{33}$$

Where ℓ is the mean neutron lifetime of prompt neutrons in seconds. Eq. (33) shows that T is in the range of 0.1 s if $\ell \approx 10^{-3}$ s and $k_{eff} = 1.01$. A reactor with such a short period would be impossible to control. However a few fission products (i.e. Br, Rb, I) emit so-called delayed neutrons which are extremely important for reactor control. These delayed neutrons can be subdivided into 6 groups as shown in Table 4.

TABLE 4. THE DELAYED NEUTRON PRECURSOR GROUPS FOR THERMAL FISSION IN ^{235}U

Group	Average energy (keV)	Half-life (s)	Fractional contribution of each group $\beta_i \times 10^{-4}$
1	250	55.72	2.1
2	570	22.72	14.1
3	412	6.22	12.6
4	670	2.30	25.3
5	400	0,61	7.4
6	698	0.23	2.7
			β = 64.2

The overall contribution of delayed neutrons to all fission neutrons is only 0.642% for ^{235}U. If t is the mean lifetime of the mother nuclide of group i, β_i is the fraction of delayed neutrons of group i, $\beta_i \times t_i$ is the mean delay time and $\sum \beta_i \times t_i$ is the mean lifetime $\bar{\ell}$ of the delayed neutrons, then the mean lifetime of all neutrons is given as:

$$\bar{\ell} = \Sigma \beta_i t_i + \ell \tag{34}$$

The change of the neutron flux density depends on the production rate of the precursors which emit these delayed neutrons. The change in concentration C_i of the precursor nuclei is as follows:

$$\frac{dC_i}{dt} = \Sigma_a \times \phi \times k_{eff} \times \beta_i - \lambda_i \times C_i \tag{35}$$

Furthermore, the time dependent neutron flux density including delayed neutrons is coupled with C_i in Eq. (36):

$$\frac{dn}{dt} = \Sigma_a \times \phi \times k_{eff} \times (1 - \beta_i) + \Sigma\lambda_i \times C_i - \Sigma_a \times \phi \tag{36}$$

These equations are solved by using:

$$n = A \times e^{t/T}$$

$$C_i = B_i \times e^{t/T} \tag{37}$$

When using the expression, reactivity ρ leads to:

$$\rho = \frac{k_{eff} - 1}{k_{eff}} \tag{38}$$

The In-hour-equation connects reactivity and reactor period as follow:

$$\rho = \frac{\ell}{\ell + T} + \frac{T}{\ell + T} \times \sum_{i=1}^{6} \frac{\beta_i}{1 + \lambda_i T} \tag{39}$$

For simplification a weighted single group of delayed neutrons is sometimes used, in which case the mean lifetime is:

$$\tau = \frac{1}{\lambda} = \frac{1}{\beta} \sum_{i=1}^{6} \frac{\beta_i}{\lambda_i} \quad \sim 13 \text{ s} \tag{40}$$

Then the following simplified equation is obtained:

$$\rho = \frac{\ell}{\ell + T} + \frac{T}{\ell + T} \times \frac{\beta}{1 + \lambda T} \tag{41}$$

2.5.2. Experimental procedure

The reactor is brought to lower power (e.g. 10 W). Then the regulating rod is removed from that position and the reactor period is determined according to the stop-watch method.

The reactivity $\rho = \rho(T)$ is calculated according to Eqs. (39) and (41). For the mean lifetime of the neutrons ℓ the value 10^{-3} s is used. The units of reactivity are measured in either ρ or Dollar (\$)[2]. ρ can be used as an absolute value according to Eqs. (38) and (41) or as a percentage ($\rho_{abs} \times 100\%$). The transfer from percent (%) to dollar (\$) depends on the reactor type. For the TRIGA Mark-II the following value has to be used:

$$\rho(\%) = \rho(\$) \times 0.73 \tag{42}$$

For TRIGA reactors, instead of the absolute value β = 0.64% (= constant for ^{235}U), β_{eff} = 0.73% is used because the delayed neutrons seem to be available at a higher fraction due to the reactor design. This is because the delayed neutrons are produced with a slightly lower energy (≈ 200 keV) than fission neutrons (≈ 2 MeV) and are therefore thermalized faster. The delayed neutron fraction β_{eff} is different for different types of reactors and for different fuels. For the experiment Table 5 can be used.

[2] When reactor physics was developed after World War II the Dollar was the most important currency in the world. As prompt criticality is the most dangerous situation in a reactor, physicists decided to nominate the reactivity value which puts the reactor into the prompt critical state as 1 Dollar.

TABLE 5. MEASUREMENTS OF REACTIVITY AND REACTOR PERIOD

Reg. rod position		t_1	t_2	t_3	t_4	$\bar{t}$	$T = 2.47.\ \bar{t}$	$\Delta\rho$ [¢]*
Start position	Stop position							

¢ = 0.01 $

2.5.3. Recommended equipment

To measure the reactivity and reactor period of the reactor, the reactor is brought to low power. The experimental procedure follows exactly chapter 2.8.1 and 2.8.2. The following main equipment/apparatus are needed for this experiment:

- An appropriate number of digital stop watches;
- A good plotting software (e.g. ORIGIN, MATLAB);
- A regulating control rod calibration curve.

2.5.4. Safety precautions

This experiment is performed in the control room in front of reactor console, where the exact reactor power and the control rod position are recorded according to stop watch method. Therefore the following radiation protection measures are obligatory for each participant of the experiment:

- Personal dosimeter for each course participant provided by the health physics group
- Each course participant should wash his/her hands after the completion of the experiment and should check for possible contamination using a hand-foot monitor.

2.6. MEASUREMENT OF THE BACKGROUND RADIATION AROUND THE OPERATING REACTOR

Keeping in mind the safety of the radiation workers and experimenters around the reactor shield, e.g. at beam tubes, thermal column, etc., it is necessary to measure the background radiation levels around the operating reactor at various power levels. The TRIGA Vienna operates up to 250 kW and is equipped with four beam tubes and one thermal column. All beam tubes and the thermal columns are used for basic and applied academic research. This experiment measures the background level at different reactor positions and at various power levels. These measurements are focused on those positions where staff members or students remain for longer periods of time.

2.6.1. Experimental procedure

The reactor hall is surveyed and the points of interests are selected and marked for measurements. The different marked points are shown in Figure 2 and Figure 3 of the reactor. In performing the measurements, some locations may be found where the background radiation is higher than10 μSv/h. These locations are determined by portable detectors and some additional measurements may be necessary when approaching the controlled areas in the direction of the increasing dose.

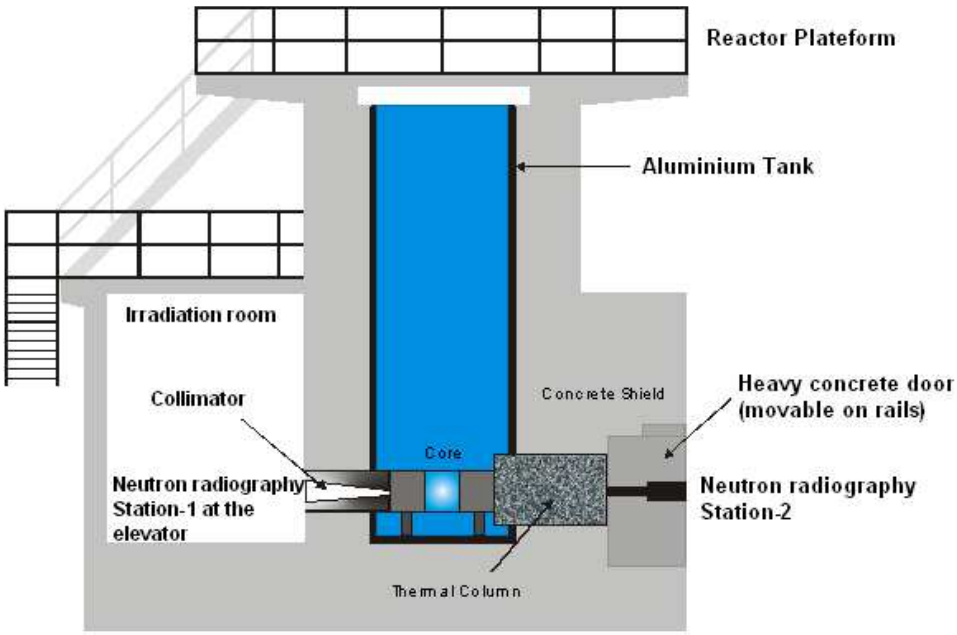

FIG. 2. Vertical cross-section of the TRIGA Mark II reactor.

2.6.2. Recommended equipment

The whole reactor hall including the reactor platform, all four beam ports and thermal column is surveyed for this experiment. The following are the main instruments required during this experiment:

- A portable gamma dose rate and count rate monitor;
- A portable neutron dose rate monitor;
- Radiation safety markers to highlight the selected area.

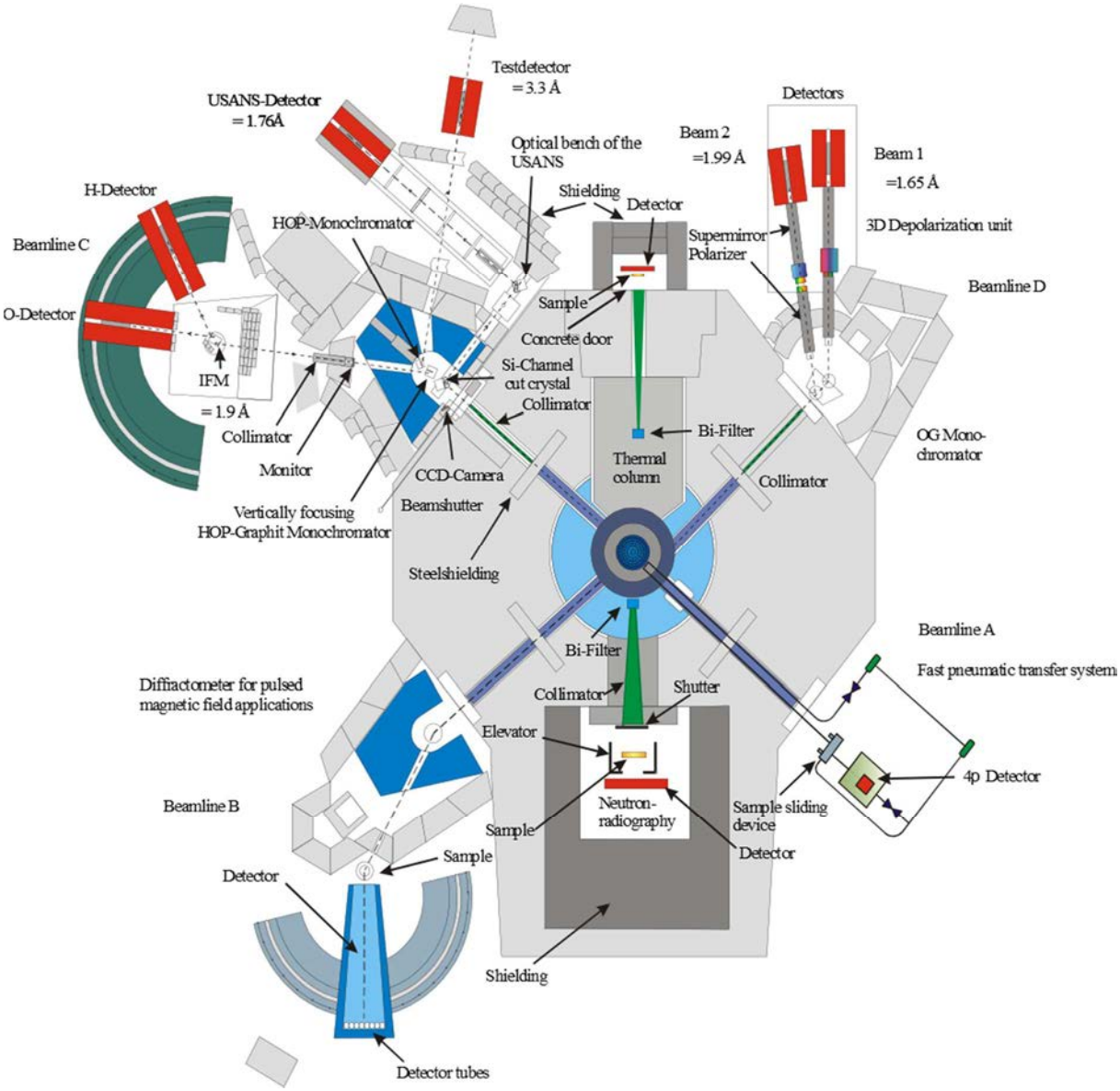

FIG. 3. Horizontal cross-section of the TRIGA Mark II reactor.

2.6.3. Safety precautions

To determine the background radiation level around the reactor hall, this experiment needs the following radiation protection measures for the safety of each participant:

- Personal dosimeter for each course participant provided by the health physics group;
- Spend as little time as possible in the controlled area;
- Each course participant should wash his/her hands after the completion of the experiment and should check for possible contamination using a hand-foot monitor.

2.7. CRITICAL EXPERIMENT

Safety is the top requirement in reactor operation. The criticality condition is an important safety design parameter in any type of reactor and the approach to criticality is the most fundamental experiment in nuclear reactor technology. When a reactor is initially loaded with fuel, the amount of fuel necessary for reactor criticality is usually not known very accurately. Therefore, the prediction of the critical mass by neutronics calculations based on reactor theory is necessary for the safe loading of fuel. The physical characteristics of a nuclear reactor as well as the validation of the calculation methods and the nuclear data employed may also be better understood by the comparison of the predicted and measured critical mass.

2.7.1. Theoretical background

Before the first start-up of any reactor a critical experiment needs to be performed. In this experiment, the reactor core is loaded with fuel elements in a number of steps. An external neutron source (e.g. AmBe source) with strength of typically 10^6 neutrons per second (in case of TRIGA Mark II of Vienna) is installed at one position in the core. These external source neutrons will induce fission in ^{235}U atoms in the surrounding fuel to produce fission neutrons. The relative number of neutrons near the core is measured with a fission chamber. It is well known that the ratio of the neutron number between two successive generations is called the multiplication factor k_∞, defined as:

$$k_\infty = \frac{Number\ of\ neutrons\ in\ generation\ i}{Number\ of\ neutrons\ in\ generation\ i-1}.$$

From Eqs. (5) and (6) one recalls that $k_\infty = \varepsilon \eta p f$, where ε is the fast fission factor, p is the resonance escape probability, η is the reproduction factor and f is the thermal utilization factor. The ideal critical system keeps the number of neutrons constant, or $k_\infty = 1$. In case of a subcritical system (k_∞<1), an increase of the neutron density is also observed because of the presence of the neutron source. Suppose that the source emits Q neutrons per unit time. Then $k^1 \times Q$ neutrons are produced at the end of the first generation and $k^2 \times Q$ at the end of the second generation, etc. This is a geometrical sequence with a multiplication factor <1, and therefore, a finite sum:

$$Q + kQ + k^2 Q + ... = \frac{Q}{1-k} \tag{43}$$

After some time when the neutron distribution in the system becomes uniform, a stable neutron flux is measured which is considerably higher than the source strength. The neutron flux increases further when the multiplication factor approaches to 1. When k becomes equal to 1, the neutron flux would increase steadily if it is not limited by factors such as temperature effects (Doppler Effect) in the fuel.

2.7.2. Experimental procedure

This experiment requires handling of fuel elements, and therefore special care and great attention needs to be ensured during this process to prevent any sort of mechanical damage to the fuel elements. The experiment starts with the 1st stage when ten fuel elements (FE) are removed from the core and stored in the pool storage rack of the reactor tank. In this configuration the reactor becomes well under-critical (or sub-critical with the presence of the external neutron source). The external neutron source stays in the core and should not be

removed during this experiment. All control rods are kept in fully withdrawn positions and the count rate of the fission chamber is measured. The additional fuel elements are very carefully and sequentially loaded to their respective core positions one by one. The count rate from the fission chamber is recorded after each insertion of one fuel element. When a certain number of fuel elements have been added, the reactor core achieves its critical state. This signal of criticality is seen by a steady increase of the count rate. The same experimental procedure is performed keeping all control rods completely inserted in the core. In case of the TRIGA Mark II of Vienna, keeping all three control rods fully inside the core, criticality is not reached after a complete core loading (presently 74 fuel elements). The number of fuel elements necessary for reactor criticality is determined by extrapolation of the criticality curve. In order to do this, the reciprocal count rate has to be compared with the number of fuel elements. Criticality is achieved when the reciprocal count rate approaches to zero. Table 6 is recommended to be used for this experiment.

TABLE 6. NUMBER OF FUEL ELEMENTS (FE) IN THE CORE DURING CRITICALITY EXPERIMENT

No. of FE in core	FE number	FE position	all CR(s) down S_{xxd}	S_B/S_{XXd}	all CR(s) up S_{xxu}	S_B/S_{XXu}
66			S_B =	1	S_B =	1
67						
68						
69						
70						
71						
72						
73						
74						
75						
76						

Note: S_B: Count rate at the start of the experiment (reference value). S_{xxd}: Count rate after adding the xx FE, all rods down. S_{xxu}: Count rate after adding the xx fuel element, all rods up.

2.7.3. Recommended equipment

The experiment is performed directly in the reactor core and involves the removal and reloading of about 10 fuel elements. Mainly it uses the fuel handling tool and fuel storage rack.

2.7.4. Safety precautions

This very important experiment is performed directly with the reactor fuel and includes extensive fuel handling. Special care and great attention needs to be ensured during handling of fuel elements, so their mechanical damage probability is reduced to the minimum. The external neutron source stays in the core and should not be removed during this experiment. The following radiation safety measures should be into account.

- Personal dosimeter for each course participant provided by the health physics group;
- Use of lab coat and gloves during the handling process of various equipment;
- Spend as little time as possible in the controlled area;
- Each course participant should wash his/her hands after the completion of the experiment and should check for possible contamination using a hand-foot monitor.

2.8. CONTROL ROD CALIBRATION AND DETERMINATION OF EXCESS REACTIVITY IN THE CORE

The reactivity of nuclear reactors changes during operation due to various causes. The operating reactor has always to be kept in critical condition (in this case its reactivity is zero) using control rods. The determination of excess reactivity and shut-down margin of a reactor is one of the strictest requirements for safe reactor operation. Thus, control rod calibration of a new built core is the most essential experiment to be performed immediately after the approach to criticality prior to the experiments.

2.8.1. Theoretical background

The reactivity effect of a control rod CR penetration into the reactor core depends on the:

- Neutron flux density at the point of insertion;
- Penetration length into the active core;
- Reactivity worth of control rods as a function of local flux.

As a first approximation, the reactivity worth of a CR is proportional to the square of the thermal neutron flux density at the point of insertion. Thus the efficiency of a given rod placed into the active core is high (reactivity worth) if the local flux is high. Generally, the thermal neutron flux density is highest in the centre and lowest at the edges of the reactor core. Therefore, rods designed for high efficiency are mainly set in the core centre.

It is notable that the CR(s) efficiency is less than it would be from the neutron flux value at the given place without the rod. The neutron absorber significantly reduces the neutron flux so that the rod is actually at a place of weaker than undisturbed flux. This flux distortion is obvious along the radius and the length of the control rod (as shown in Figure 4 and Figure 5).

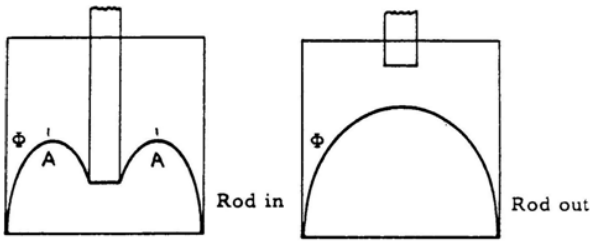

FIG. 4. Radial distribution of the neutron flux with and without a control rod.

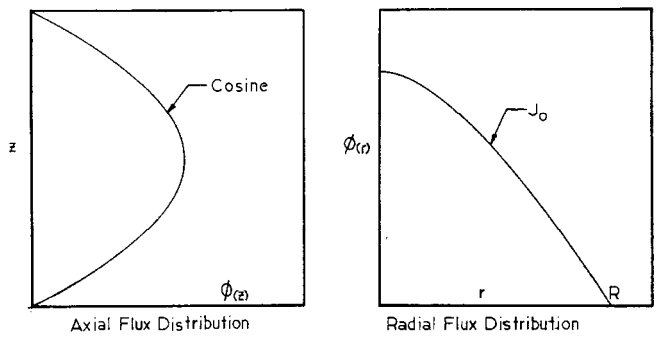

FIG. 5. Axial and vertical distribution of the undisturbed neutron flux.

The flux bias results in:

- Modified spatial distribution of the power density inside the active core, partly altering the performance of the given reactor, and partly affecting the temperature distribution in the core.
- Influence on individual rod worth values (flux-dependent) of the other rods, provided several ones are present in the core. For example, the sum of an individual rod worth values of two safety rods is less than the overall worth. This is the so-called rod interference.

For defining the reactivity worth of control rods as a function of penetration, two extreme positions of the CR(s) are:

- Completely outside the core. In this position, the rod has zero effect on the reactivity.
- Completely inside the core. In this position, the rod has a maximum effect on reactivity. This maximum efficiency is called the total rod reactivity value.

In case of uniform material distribution and symmetric flux distribution, the rod mid-height coincides with the active core mid-height.

There are several methods for determining the characteristic reactivity curve of a control rod. The selection of method depends on the reactor type, the individual rod values, the available instrument and time. The basic problem consists essentially of determining the reactivity for different control rod positions. The current methods are:

- Determination of reactivity based on the reactor period measurement;
- Rod calibration in a sub-critical system;
- Inter calibration method;
- Rod oscillation method;
- Rod drop method.

The first and most frequently used method is the *rod calibration by the reactor period method,* as described below.

It is an absolute method (not relative) to obtain a “reactivity versus rod position” diagram. During this measurement, the reactor is in supercritical operation mode. With the rod in different withdrawn positions, the reactor is operating at low power and the reactor period is determined. The rod to be calibrated is in its fully down position.

The calibration starts when the rod to be calibrated is slightly withdrawn at *P(0)* (power at time 0). After some time t, the reactor power reaches *P(t)*. The two power levels are connected by the following relation:

$$P(t) = P(0)\, e^{t/T} \quad , \tag{44}$$

Where T is the reactor period in seconds and t is the time elapsed between the two power levels (i.e. from 30 W to 45 W = 1.5 times power increase measured with a stop watch). If *P(t) = 1.5 P(0)*, then: $1.5\, P(0) = P(0)\, e^{t/T}$ and $T = t/\ln 1.5 = 2.47\, t$. Here *t* represents the time in seconds during which power is increased by a factor of 1.5.

2.8.2. Experimental procedure

For conducting this experiment, several stop watches are used to measure the time during which the reactor power is increased by factor of 1.5. This time is multiplied by a factor of 2.47 to obtain the reactor period. The In-hour equation relates the reactor period to the reactivity. Thus, the reactivity is determined either from a diagram or from available tables. Continuing the same procedure in a number of rod steps, the total length of the control rod can be calibrated as shown in Figure 6.

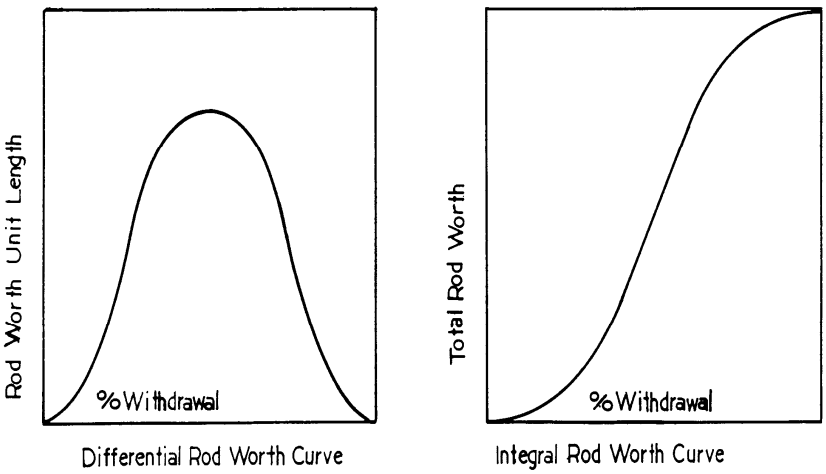

FIG. 6. Differential and integral control rod worth curves.

The exact position of the control rods may be taken from the rod position indicator in the control desk. The obtained reactivity values may be applied to plot the integral and differential characteristic curve. This is an absolute method that produces very accurate results. The drawback is that this experiment is performed in supercritical state and also takes a longer time to measure. Table 7 is suggested for recording the data during this experiment.

Once all CR(s) have been calibrated, the excess reactivity is determined by the following measurements. The reactor is operated at a given power level and all rod positions are recorded. Using the rod calibration curve of each control rod, the reactivity value $\Delta\rho$ is determined by the difference $\Delta\rho$ at the present rod position to the fully out position of the CR. The total core excess reactivity is the sum of the individual $\Delta\rho$ of all rods. The experimental results are recorded and finalised then in Table 8.

TABLE 7. THE PROPOSED TABLE FOR DATA ACQUISITION OF THE CONTROL ROD CALIBRATION EXPERIMENT

Rod position		Time (s)							$T = \bar{t} \times 2.47$	$\Delta\rho$ ($)	$\int\rho$ ($)
start	stop	t_1	t_2	t_3	t_4	t_5	t_6	$\bar{t}$			

TABLE 8. DETERMINATION OF EXCESS REACTIVITY USING CONTROL ROD CALIBRATION CURVE

Reactor power, kW	Transient rod Position $\Delta\rho_T$	Shim rod Position $\Delta\rho_S$	Regulating rod Position $\Delta\rho_R$	Total excess reactivity $\Sigma\ \Delta\rho_T+\Delta\rho_S+\Delta\rho_R$
0.01				
0.1				
1				
10				
100				
250				

2.8.3. Recommended equipment

This experiment needs the following main equipment/apparatus:

- Digital stop watches;
- Graphic plotting software (e.g. ORIGIN, MATLAB);
- A control rod calibration curve.

2.8.4. Safety precautions

This practical exercise is performed in the reactor control room with following radiation safety measures:

- Personal dosimeter for each course participant provided by the health physics group;
- Spend as little time as possible in the controlled area;

- Each course participant should wash his/her hands after the completion of the experiment and should check for possible contamination using a hand-foot monitor.

2.9. CALIBRATION OF THE SHIM ROD IN THE SUB-CRITICAL REGION

Various reactivity effects in nuclear reactors are determined by compensating the given reactivity with the other available control rods to keep the reactor in critical state. Therefore the calibration of the control rod is essential when the control rods are used as reactivity standards to measure the reactivity changes caused by any other perturbation in a reactor. The data of the control rod calibration is important for the reactor operator because the operator can then estimate the reactivity changes by any control rod movement and thus allows operating the reactor within safe limits.

2.9.1. Theoretical background

In the control rod calibration and core excess reactivity experiment, the shim rod can only be calibrated in the region where the reactor is supercritical. In fact, if the transient rod and regulating rod are fully out, then the reactor is still in subcritical state up to a certain shim rod position. This part of the shim rod length (from position 0 to the criticality point) is calibrated through another method called the sub-critical neutron multiplication. The method is based on the fact that the Sb-Be photo-neutron source constantly emits neutrons which are multiplied in the system. The number of neutrons is measured by a fission counter.

If Q is the neutron source strength of the neutron source, k_{eff} is the effective multiplication factor and f is constant of proportionality, then the count rate Z at the fission counter is given by:

$$Z = f\frac{Q}{1-k_{eff}} = C\frac{1}{1-k_{eff}} \ . \tag{45}$$

The effective multiplication factor k_{eff} is connected with the reactivity ρ as:

$$k_{eff} = \frac{1}{1-\rho_{abs}} \tag{46}$$

The ρ_{abs} can be determined by a given reactivity jump (i.e. by dropping a control rod with a well-known reactivity value). Measuring Z, the constant $C = Q \times f$ is determined by using Eq. (47):

$$C = -\frac{Z \times \rho_a}{1-\rho_a} = -\frac{Z \times 0{,}73 \times 10^{-4}\ \rho_{cents}}{1-0{,}73 \times 10^{-4}\ \rho_{cents}} \tag{47}$$

The constant C is determined by following steps:

(1) The transient rod is fully up ($I\uparrow$);
(2) The shim rod is fully down ($T\downarrow$);
(3) The regulating rod is fully down ($R\downarrow$).

With these control rod positions, the count rate Z_1 is measured at the fission counter, (shim and the regulating rod are kept fully down), and then the regulating rod is brought fully up ($R\uparrow$). Now a higher count rate Z_2 ($Z_2 > Z_1$) is obtained. This increase in count rate (ΔZ)

corresponds to total reactivity change $\Delta\rho$ of the regulating rod reactivity value. Therefore, to each ΔZ value, the corresponding $\Delta\rho$ is achieved. With this known Z_2 value of the constant C, the shim rod in the sub-critical region can also be calibrated:

$$\rho_{cents} = -\frac{C}{(Z - C) \times 0{,}73 \times 10^{-4}} \tag{48}$$

2.9.2. Experimental procedure

(1) The transient rod is kept fully withdrawn (up), the shim and regulating rod are in the lowest position (down) and the count rate Z_1 is determined.
(2) The transient rod is held at fully up position. The shim rod is still at fully down while regulating rod is moved fully out and the count rate Z_2 determined.
(3) Now the shim rod is removed in steps from the core. After each step, the count rate is measured through the fission chamber.
(4) Plot the reactivity ρ in cents as function of the shim rod position.

The templates in Tables 9 and 10 are recommended for this experiment.

TABLE 9. REACTIVITY OF THE REACTOR CORE

Rod position	Count rate at fission counter	Excess reactivity of regulating rod
I↑, T↓, R↓	Z1 =	ρ_1 = determined during experiment
I↑, T↓, R↑	Z2 =	$\rho_2 = 0$

$$C = -\frac{(Z_2 - Z_1)(\rho_2 - \rho_1) \times 0{,}73 \times 10^{-4}}{1 - (\rho_2 - \rho_1) \times 0{,}73 \times 10^{-4}} \quad [¢]$$

TABLE 10. SHIM ROD CALIBRATION

Shim rod position	Three values Z	Average value $\overline{Z}$	ρ[¢]

2.9.3. Recommended equipment

This experiment requires

- Graphic plotting software (e.g. ORIGIN, MATLAB);
- A fission ionization chamber fixed inside the core;
- A simple calculator.

2.9.4. Safety precautions

This practical exercise is performed in the reactor control room with following radiation safety measures.

- Personal dosimeter for each course participant provided by the health physics group;
- Spend as little time as possible in the controlled area;
- Each course participant should wash his/her hands after the completion of the experiment and should check for possible contamination using a hand-foot monitor.

2.10. REACTIVITY VALUES OF FUEL ELEMENTS IN VARIOUS CORE POSITIONS

This experiment provides the reactivity values of fuel elements in various core positions. In the TRIGA core lattice, the reactivity worth of fuel elements for a well-thermalized, small, compact and uniform core is proportional to the square of the thermal neutron flux density, integrated over the entire fissile volume of the fuel elements. It also gives an idea of the distribution of neutron flux in the core.

2.10.1. Theoretical background

The neutron flux density distribution in a cylindrical core is calculated by solving the diffusion equation in cylindrical coordinates. The solution (flux) of the diffusion approximated equation is:

$$\phi(r,z) = AJ_0\left(\frac{2.405r}{R}\right)\cos\frac{\pi z}{H} \tag{49}$$

Eq. (49) shows that the neutron flux density decreases both in the axial and radial directions towards the edges of the core. It is obvious that fuel elements in the different core positions have different reactivity values.

2.10.2. Experimental procedure

The fuel and graphite elements are selected at different distances to the core centre. This experiment is performed at low power (10 W) and the regulating rod is used to measure the reactivity worth of the individual fuel or graphite element as the control rod system is set into the automatic mode which automatically compensates reactivity perturbations.

Table 11 may be used as template for recording the experimental results. During operation, the fuel element to be measured is removed from the reactor core and stored into the fuel storage rack. Because of the decrease in fuel amount from the critical core, the reactor power is decreased. The automatic control system adjusts the regulating rod positions again to bring the reactor back to the same power level. The difference of two regulating rod positions (before and after withdrawal of a fuel element) is expressed in terms of reactivity values by using the regulating rod calibration curve. The experiment is repeated with fuel elements in different positions and also if possible with reflector elements.

The reshuffling the fuel elements back to the reactor core is performed slowly to avoid any sudden rise of power and a possible reactor shut-down due to the sudden reactivity increase. For the evaluation of this experiment, the distance of the fuel element from the centre of the core is required. The TRIGA Mark II core has a cylindrical core lattice in which fuel elements are arranged into five concentric rings. For near centre fuel elements the regulating rod reactivity value might be too low, so the shim rod has also to be removed. The changes in the shim rod reactivity value have to be added to the regulating rod reactivity value.

TABLE 11. REACTIVITY VALUES OF FUEL ELEMENTS AS FUNCTION OF CORE POSITIONS

Reactor power: ..... W

Element No.	Core position	Reg. rod position before	Reg. rod position after withdrawal	Reg. Rod position after insertion	Δρ [¢]
		Shim rod position			
		Shim rod position			

2.10.3. Recommended equipment

During this practical exercise, FE(s) and graphite elements are selected and removed from the core one by one by measuring their worth. This experiment needs the following equipment/apparatus:

- A fuel handling tool;
- Graphic plotting software (e.g. ORIGIN, MATLAB);
- A regulating rod calibration curve.

2.10.4. Safety precautions

This measurement is performed in the reactor plate form and needs the following radiation safety measures:

- Personal dosimeter for each course participant provided by the health physics group;
- Use of lab coats and gloves for contamination protection during the experiment;
- On completion, the fuel handling tool should be checked for contamination. If it is clear then should be placed back to its stand in the reactor hall;
- Spend as little time as possible in the controlled area;
- Each course participant should wash his/her hands after the completion of the measurement and should check for possible contamination using a hand-foot monitor.

2.11. REACTOR POWER CALIBRATION AND TEMPERATURE COEFFICIENT OF THE REACTIVITY

The thermal power of a water-cooled reactor can be determined by measuring the temperature increase of the water during a given time interval. The electrical power of a nuclear power plant can be calculated by multiplying the thermal power by its thermal efficiency factor. The efficiency of a nuclear power plant is approximately 37% (European Pressurized Water Reactor).

2.11.1. Theoretical background

The temperature fluctuations during reactor operation are unavoidable and any temperature change influences the core reactivity. With the rise in temperature the mean energy of the thermal neutrons is increased. This influences the neutron absorption, as the neutron cross-section depends on the neutron energy (fuel temperature coefficient). Furthermore, the mean free path and the non-leakage factor depend on the density and therefore on the temperature (density temperature coefficient).

The nuclear temperature coefficient results mainly from the energy dependence of the absorption and scattering cross-sections. The kinetic energy of the neutrons is proportional to the absolute temperature T; therefore the cross-sections vary in the 1/v-region as:

$$\sigma_a = \sigma_{a0}\left(\frac{T_0}{T}\right)^{1/2} \tag{50}$$

The same dependence can be shown for the scattering cross-sections. Therefore, all reactor parameters depending on these factors are also temperature dependent:

$$L^2 = \frac{1}{3\Sigma_a(T)\Sigma_s(T)} \tag{51}$$

$$\tau = \tau_0 - \int_{E_{th0}}^{E_{th}} \frac{1}{3\xi\Sigma_a(T)\Sigma_s(T)\xi}\frac{dE}{E} \tag{52}$$

Therefore k_{eff} or reactivity ρ are temperature dependent:

$$\rho(T) = \frac{k_\infty - 1}{k_\infty} - \frac{B^2}{k_\infty}\left[\tau_0 - \frac{1}{3\xi\Sigma_s\Sigma_t} ln\frac{T}{T_0} + L_0^2\left(\frac{T}{T_0}\right)^{0.6}\right] \tag{53}$$

Additionally, the nuclear temperature coefficient has to be considered. The macroscopic cross-sections are proportional to the number of atoms per unit volume. L^2 and τ are proportional to the inverse density square:

$$L^2 + \tau = L_0^2(d_0/d)^2 + \tau_0(d_0/d)^2 \tag{54}$$

Therefore, k_{eff} and ρ are also dependent on the temperature. As long as the sum of all effects is negative, the temperature coefficient of the reactivity is also negative and the reactor is called self-stabilizing. In contrast, with a positive temperature coefficient, the reactor power increases with increasing temperature, which makes the reactor unstable. The TRIGA type reactors are inherently safe because of very large negative temperature coefficients of the reactivity which comes mainly from the ZrH moderator.

2.11.2. Experimental procedure

Before the start-up of the reactor the pool water is heated electrically by 5 immersion heaters with a known total power of 20 kW. This results in the rise of the water temperature (5.19°C ± 0.03°C) in a certain time interval (5 hours × 20 kW = 100 kWh) which is measured very accurately by thermometers. This procedure provides the calibration of the temperature increase in terms of thermal power. For example, if the reactor is operated at an unknown power (i.e. ~100 kW) with the cooling system shut down, the rise in water temperature is increased and can be compared to that power calibration with the heaters. Thus the thermal power of the operating reactor is calculated easily.

To measure the temperature coefficient of the reactivity it is necessary to operate the reactor first at a low power, i.e. 10 W. The position of all control rods and the FE temperature are noted. Then the reactor power is increased to 100 kW and the control rod positions and fuel element temperature are recorded again. At this higher power level the control rods are withdrawn from the core relative to the 10 W operation of the reactor. The difference of reactivity $\Delta\rho$ is compensated by the increased fuel temperature ΔT. The $\Delta\rho$ can be found from the control rod calibration curve, and the ΔT can be read from the instrumentation. However, the fuel element's temperature is measured by thermocouples installed in the centre of the fuel element axis. This implies that the average fuel elements temperature is less than the measured temperature. The average temperature of the fuel should be calculated if the surface temperature is assumed to be the same as cooling water temperature while the central temperature is taken from the instrument readings.

In first approximation a linear temperature distribution is used, however, for more detailed calculations the actual temperature distribution is calculated. From $\Delta\rho$ and ΔT the $\Delta\rho/\Delta T$ is calculated and represents the temperature coefficient of reactivity. Tables 12 and 13 are used for demonstration of experimental results.

TABLE 12. REACTOR POWER CALIBRATION AND TEMPERATURE COEFFICIENT OF REACTIVITY

Reactor power	Transient rod position	Shim rod position	Reg. Rod position	Water temp.	FE temp.	Δρ [¢]	ΔT [°C]
10 W							
100 kW							

TABLE 13. PROPOSED TABLE FOR POWER CALIBRATION

t [min]	T [°C]	t [min]	T [°C]	t [min]	T [°C]
0		35		70	
5		40		75	
10		45		80	
15		50		85	
20		55		90	
25		60		95	
30		65		100	

2.11.3. Recommended equipment

This experiment needs the following equipment/apparatus:

- Pool water heaters;
- A pool temperature detector;
- A control rod calibration curve;
- Graphic plotting software (e.g. ORIGIN, MATLAB).

2.11.4. Safety precautions

This experiment is performed in the reactor hall and needs the following radiation safety measures:

- Personal dosimeter for each course period provided by the health physics group;
- Spend as little time as possible in the controlled area;
- Each course participant should wash his/her hands after the completion of the experiment and should check for possible contamination using a hand-foot monitor.

2.12. DEMONSTRATION OF A REACTOR PULSE WITH DIFFERENT REACTIVITY INSERTION

The TRIGA reactor is designed to undergo significant power pulses. The transient rod is designed to be pneumatically withdrawn in a very short period of time. Upon rod removal, the reactor power increases to a value that produces a strong fuel temperature increase which compensates the excess reactivity inserted through transient removal. This is the peak power and is reached in few milliseconds. The fuel temperature continues to rise with an increasing loss of reactivity and the reactor power decreases to a comparatively low steady state value. The final steady state power depends on the reactivity insertion and the heat transfer characteristics of the fuel.

2.12.1. Theoretical background

Due to the unique characteristics of the ZrH moderator used in TRIGA reactors, one can withdraw a control rod promptly from the critical core. Any other type of reactor would be severely damaged by such pulse operation. This is routinely performed at the TRIGA and results in a power pulse or power burst. The property of the ZrH moderator making this possible is that the H atoms form oscillations around its lattice position (see Figure 7). The energy of these oscillations is quantised like in a three-dimensional harmonic oscillator (Einstein oscillator). Incident neutrons are moderated and are then in thermal equilibrium with these atoms. During a power burst the fuel temperature rises, the neutrons may be accelerated by the collisions with the H-atoms and the thermal neutron spectrum is hardened. Therefore, the number of fissions and the reactor power is decreased. In case of the TRIGA reactor Vienna, the whole procedure takes about 40 ms while the peak power increases to 250 MW and the peak neutron flux to 1×10^{16} $cm^{-2} \cdot s^{-1}$. A typical power transient is shown in Figure 8.

2.12.2. Experimental procedure

The reactor power is raised to 10 W with the shim rod and the regulating rod; only the pulse rod stays in its down position. After switching the control instrumentation to "pulse mode" the pulse rod (maximum reactivity value ~2 $) is removed the critical core and the power pulse initiated. The power peak value can be varied by changing the shock absorber position which determines how far the pulse rod is fired out from the core and then determines the amount of reactivity inserted into the critical core.

During and after the pulse the FE temperature and maximum power can be read from the instrumentation. The procedure may be repeated with different shock absorber positions.

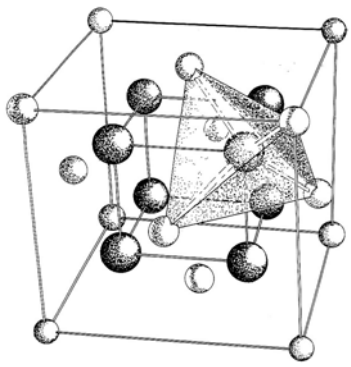

FIG. 7. Unit cell of ZrH_2, 4 Zr atoms (small nuclei) surround 1 H atom (large nuclei).

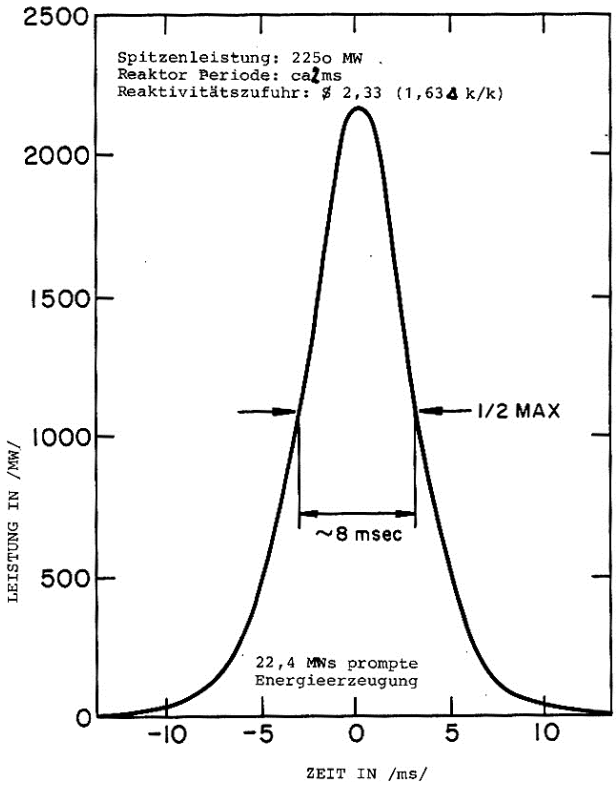

FIG. 8. Typical power transient. It has a peak power of 2250 MW, a reactor period of 2 ms, and a reactivity insertion of 2.33 $, or 1.63 Δk/k.

2.12.3. Recommended equipment

During this special practical exercise, already installed reactor instrumentation is extensively used.

2.12.4. Safety precautions

This experiment is performed in pulse mode operation and needs the following radiation safety measures:

- Personal dosimeter for each course period provided by the health physics group;
- Spend as little time as possible in the controlled area;
- Each course participant should wash his/her hands after the completion of the experiment and should check for possible contamination using a hand-foot monitor.

2.13. GAMMA SPECTROSCOPY OF TRIGA FUEL

Gamma spectrometry is one of the most common methods used for irradiated fuel inspection. By measuring the fission product isotopes (caesium, zirconium etc.) one can correlate the amount (or activity) of these isotopes with their burn up values. Due to the directly proportional relation between its caesium ratio ($^{134}Cs/^{137}Cs$) and burn up value, the gamma spectroscopy of the spent fuel is very attractive for long irradiation histories. This method is also applied to determine the fuel burn up and material composition of an irradiated fuel. This experiment demonstrates the measurement of two caesium isotopes (^{134}Cs, ^{137}Cs).

2.13.1. Theoretical background

The activity is measured by using Eq. (55):

$$NPA = A(t) \times t_{detection} \times Eff_{Detector} \times P_{\gamma} \text{ or } cps = A(t) \times Eff_{Detector} \times P_{\gamma} \quad (55)$$

Where *A(t)* is the measured activity, *NPA* is a net peak area, $t_{detection}$ is detection time, $Eff_{Detector}$ is the detector efficiency and $P\gamma$ is gamma emission probability of the selected energy, while *cps* stands for counts per second. The method of ^{134}Cs measurement is based on ^{134}Cs /^{137}Cs ratio measurements and is developed for safeguards applications. The detector is calibrated by one measurement if both gamma lines (^{134}Cs and ^{137}Cs) are emitted. This relative calibration method is applied from 600 keV to 800 keV gamma energies. For the Cs ratio determination, Eq. (56) is applied. This equation is corrected for the discharge time with related nuclear constants. Discharge time refers to the time when the fuel element is removed from the core.

$$\frac{A_{34}(t_d)}{A_{37}(t_d)} = \frac{cps_{34}}{cps_{37}} \times \frac{P_{\gamma}^{37}}{P_{\gamma}^{34}} \times \frac{E_{\gamma}^{37}}{E_{\gamma}^{34}} \times \frac{e^{\lambda_{34}\, t_d}}{e^{\lambda_{37}\, t_d}} \quad (56)$$

The factor $E_{\gamma}^{37}/E_{\gamma}^{34}$is calculated for each scanned length by the relative efficiency calculation method.

2.13.2. Experimental procedure

The fuel element to be measured is mounted to the fuel inspection unit by the fuel transfer cask where the fuel element can be moved vertically with an adjustable speed. Although this unique fuel elevator system has the ability to scan each millimetre of the SPE accurately in axial direction, a one centimetre scale measurement is selected for convenience. A collimator of 1 cm diameter is used and the distance between detector and fuel rod is kept to about 10 cm. To minimise statistical and counting errors, the time for each measurement is selected from 200 to 300 seconds. The dead time of the detector is recorded up to 16%. This gamma spectroscopic experiment is performed inside the reactor hall but outside the reactor tank. Due to more than adequate shielding of the high density fuel transfer cask, only about 2 to 3 μSv dose rate has been recorded at the contact surface of the cask and the working station. The experimental setup consists of the fuel transfer cask, the fuel inspection unit, beam collimator and coaxial High Purity Germanium (HPGe) p-type detector which are shown in figure 9.

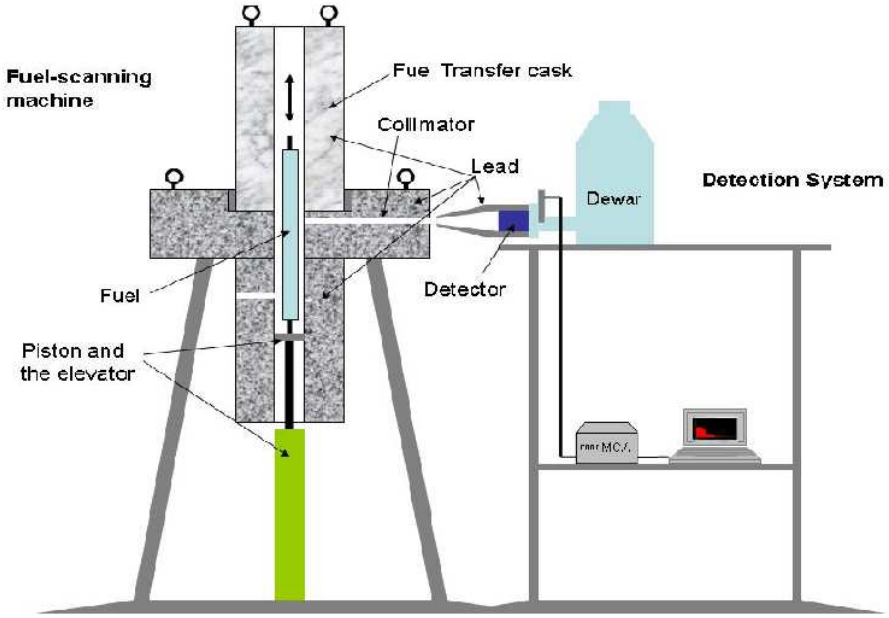

FIG. 9. Experimental set of gamma spectroscopic experiment.

The signal from the detector is transferred to the on-line computer with calibrated gamma spectroscopic software. Using suitable fast electronics, the gamma ray spectrum is measured from 200 to 300 seconds for each centimetre and the spectrum is saved on a removable hard disk of the computer for further detailed analysis i.e. identification of ^{137}Cs peak and corresponding peak area etc. Figure 10 illustrates one example of a typical plenum gamma ray spectrum with ^{137}Cs peaks.

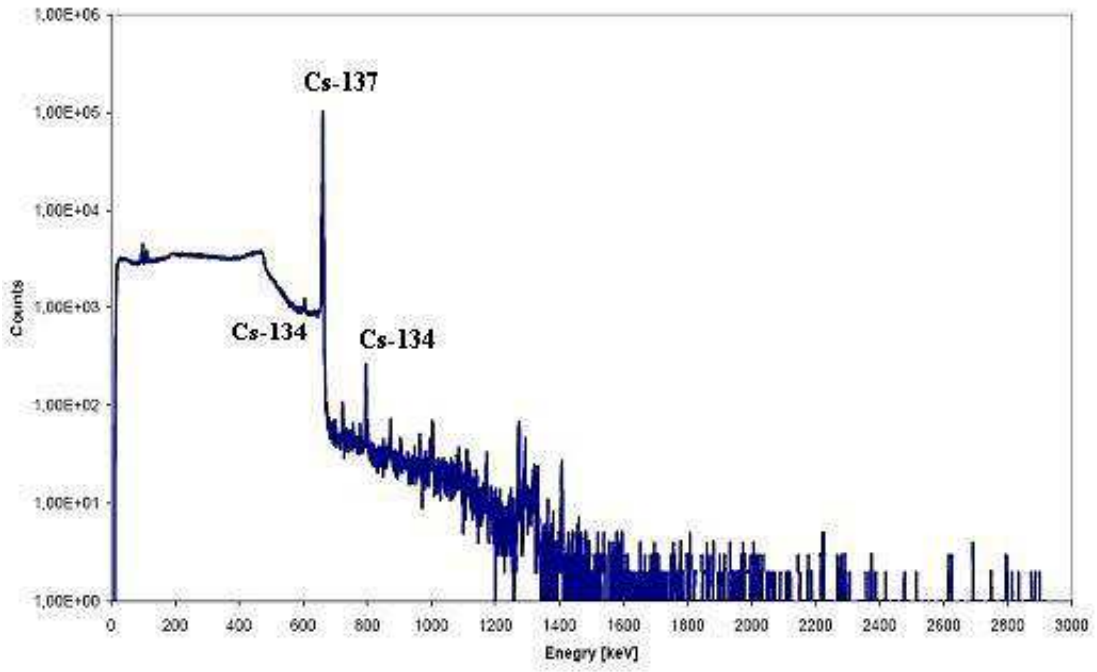

FIG. 10. Typical gamma spectrum of TRIGA fuel element.

2.13.3. Recommended equipment

During this experiment spent FE(s) are transferred from the reactor tank to the fuel inspection unit. It needs the following equipment/apparatus:

- A fuel handling tool;
- A fuel transfer cask;
- A dose rate monitor;
- A fuel Inspection Unit;
- A detector calibration source (e.g. caesium or europium);
- A HPGe gamma detection system;
- Spectrum analysis software.

2.13.4. Safety precautions

Due to high dose rates, the spent FE is transferred to fuel transfer cask. This process completely takes place under water inside the reactor pool. This experiment needs the following safety measures during the experiment:

- Personal dosimeter for each course participant provided by the health physics group;
- Measuring dose rate at each step of the experiment;
- Surface contamination control of the cask during the experiment;
- Use of lab coats and gloves for contamination protection during the experiment;
- Spend as little time as possible in the controlled area;
- Each course participant should wash his/her hands after the completion of the experiment and should check for possible contamination using a hand-foot monitor.

3. REACTOR INSTRUMENTATION AND CONTROL EXPERIMENTS

All types of RR(s) are operated and controlled with an Instrumentation and Control (I&C) system. Modern I&C systems provide automatic and manual reactor operation modes, complete real-time operator display and reduces the spare part replacement problems etc. The information on all aspects of reactor operation is displayed on the Control System Computer (CSC). The colour graphics monitors are used to display real-time operational data in concise, accurate and easily understandable formats. Information displayed on the monitors is recorded in hard copy using the graphics printer in the CSC. During the reactor operation, the reactor control rod position commands are transmitted via a high-speed Ethernet link from the Control System Computer to the Data Acquisition Computer (DAC) and in turn to the rod drive mechanisms. This reduces the complexity, vulnerability, and cost of data transfer.

The TRIGA Mark II reactor is controlled by four nuclear channels; their signals are displayed both at a colour graphic-monitor and at bar graph indicators. The block diagram of the I&C system of the TRIGA reactor has been shown in Figure 11.

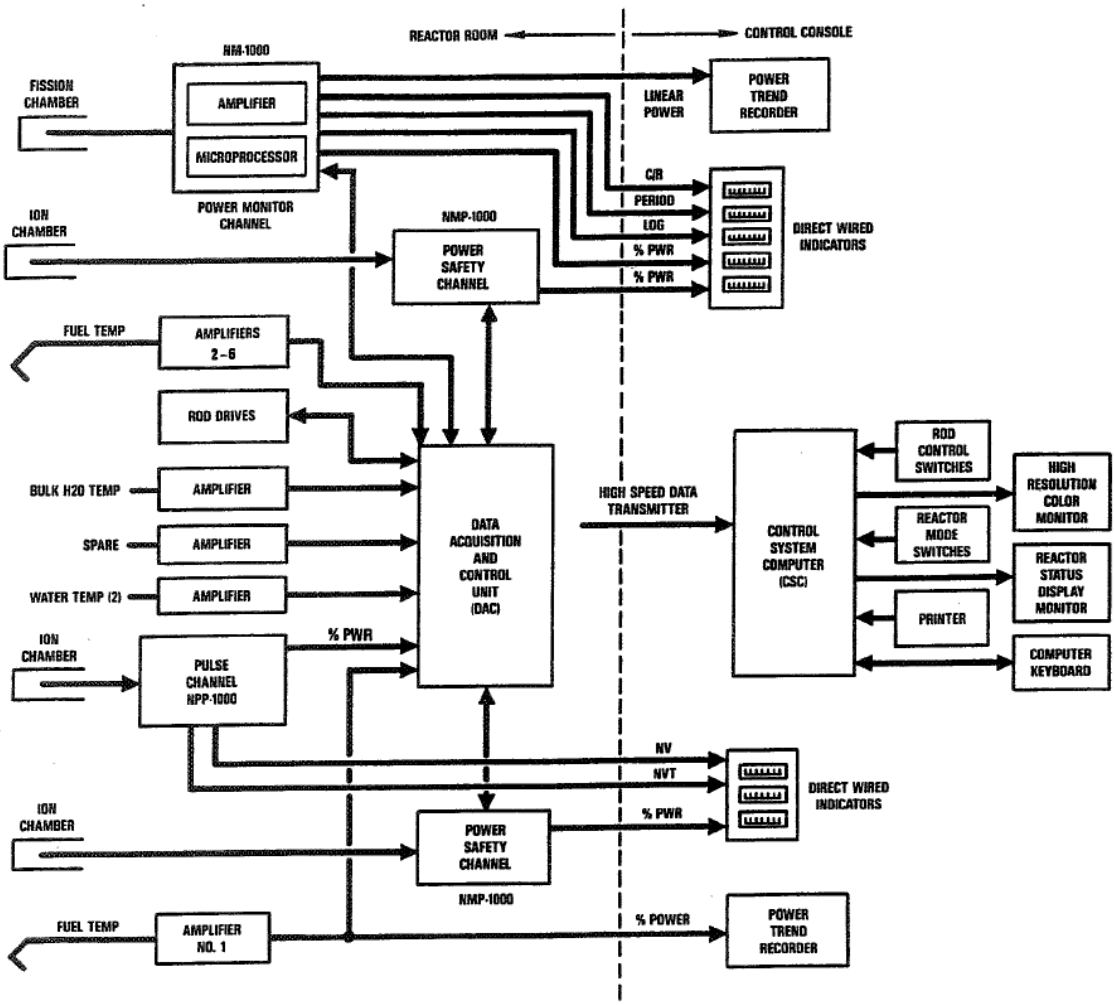

FIG. 11. Block diagram of TRIGA reactor control system.

- The auto-ranging wide-range channel NM-1000 controls the reactor power from the source level (around 5 mW) up to nominal power of 250 kW. It uses a fission chamber which is operated in Campbell mode; the signal is controlled by a microprocessor.
- Two independent linear channels, NMP-Ch and NMP-Ph control the reactor power from the source level up to nominal power. The signals pass over a range switch, which selects the power range. If the signal of one of these two channels exceeds the selected power range by more than 10%, the reactor is shut down automatically. Both channels use Compensated Ionization Chambers (CICh) as sensors.
- For the control of reactor pulse operation, an Uncompensated Ionization Chamber (UICh) is used. This chamber records the shape of the reactor pulse, which is displayed on the graphic monitor. Further pulse data like integrated power and minimum period are calculated from this signal.

3.1. NEUTRON FLUX DENSITY MEASUREMENT USING COMPENSATED IONISATION CHAMBERS

3.1.1. Theoretical background

The neutron flux density is the most important parameter which must be controlled during reactor operation. Its range varies from source level (shut down reactor) to 10^{13} n/cm^2/s or even more at full power operation. However there are four different types of radiations in a reactor core, i.e. prompt, delayed gamma radiation and prompt, delayed neutrons, with a large variety of energies.

In the shutdown situation condition, the delayed gamma radiation and some source neutrons are present. During the start-up procedure, the ratio between gammas and neutrons changes constantly while at full power level, the neutron signal dominating the gamma radiation. Therefore, very special detectors are required to measure the neutron induced signal at different power levels.

In shutdown and low power mode, the optimal detectors are fission chambers (FC); at medium power level, the compensated ionisation chambers (CICh) are used; while at full power level, uncompensated ionisation chambers (UICh) are applied. The UICh is similar to CICh except it does not include the compensating electrode – it is just a chamber with a boron coated electrode. UICh are used at high reactor power level where the gamma induced signal is negligible compared to the neutron induced signal.

The CICh detection system reduces the gamma influence rate and selectively measures neutrons even in a high gamma background. A CICh is a differential chamber comprising three concentric electrodes which define two chambers in the same housing. The first chamber is located between the external positive polarised electrode and the central electrode, which collects the signal. The surfaces of the electrodes are coated with a boron deposit and therefore are sensitive to neutron and gamma rays. The schematic diagram of CICh is shown in Figure 12.

The most probable reaction is $^{10}B(n,\alpha)^{7}Li$ reaction which converts the thermal neutrons into directly detectable alpha particles as shown in following reactions:

$$^{10}_{5}B + ^{1}_{0}n \rightarrow ^{7}_{3}Li^{*} + ^{4}_{2}He \qquad Q = 2.31 \text{ MeV}$$

$$^{10}_{5}B + ^{1}_{0}n \rightarrow ^{7}_{3}Li + ^{4}_{2}He \qquad Q = 2.792 \text{ MeV}$$

The reaction product ^{7}Li may be left in its ground state or in its first excited state. When thermal neutrons are used to induce the reaction, about 94% of all reactions lead to the excited state; the remaining 6% of reaction products leads directly to the ground state. These nuclear reactions produce about 2.31 and 2.792 MeV respectively. Alpha particles and ^{7}Li ionise gas and produce charge pulse or an ionisation current due to the neutron reaction in boron. Also, gamma radiation from fission products produces electrons through photoelectric, Compton and pair production effect in the chamber.

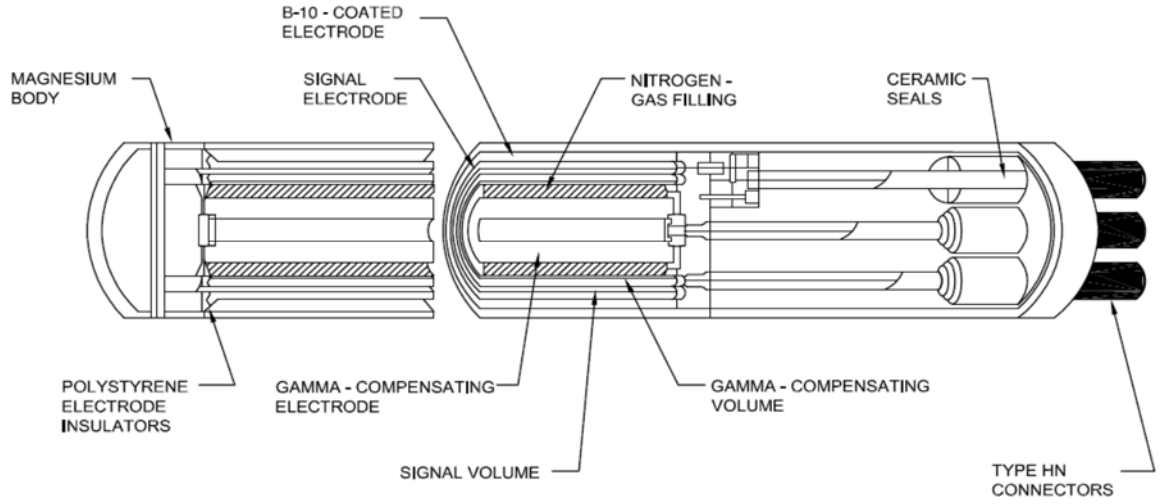

FIG. 12. Cross-section of a Compensated Ionisation Chamber (CICh).

The second chamber is located between the internal negative polarised electrode and the signal electrode. The surface is not coated with a boron deposit and is therefore only sensitive to gammy rays. The current of these two chambers is subtracted from each other due to their opposite polarisation and the resulting current is therefore mainly proportional to the neutron induced signal only as shown below:

Chamber one with boron coating:	n+γ sensitive (+HV)
Chamber two without boron:	γ sensitive (-HV)

By subtracting the two signals, the gamma signal is compensated for, since the chamber is only sensitive to neutrons, namely n + γ - γ → n (signal) (also see Figure 13).

The main characteristics of a CICh are the following:

- It is mainly sensitive to neutrons;
- A typical neutron sensitivity is 10^{-14} A/n.v to 10^{-13}A/n.v, where n.v is the neutron flux density (neutrons/cm^2/s);
- The chamber has to be compensated for after installation in the reactor in the presence of a high gamma field but in the absence of neutrons (i.e. soon after reactor shut down with removed neutron source).

Figure 14 shows a typical compensation plot of a CICh.

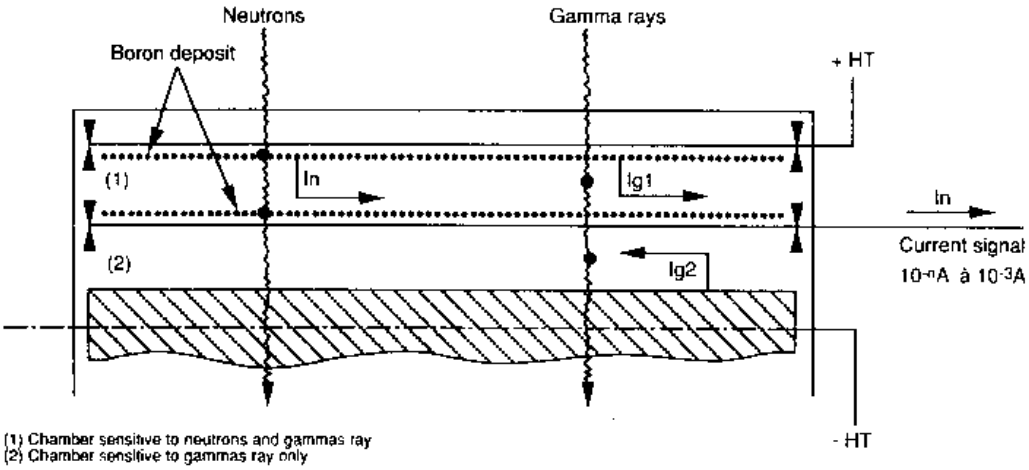

FIG. 13. Compensated ionisation chamber mimic diagram.

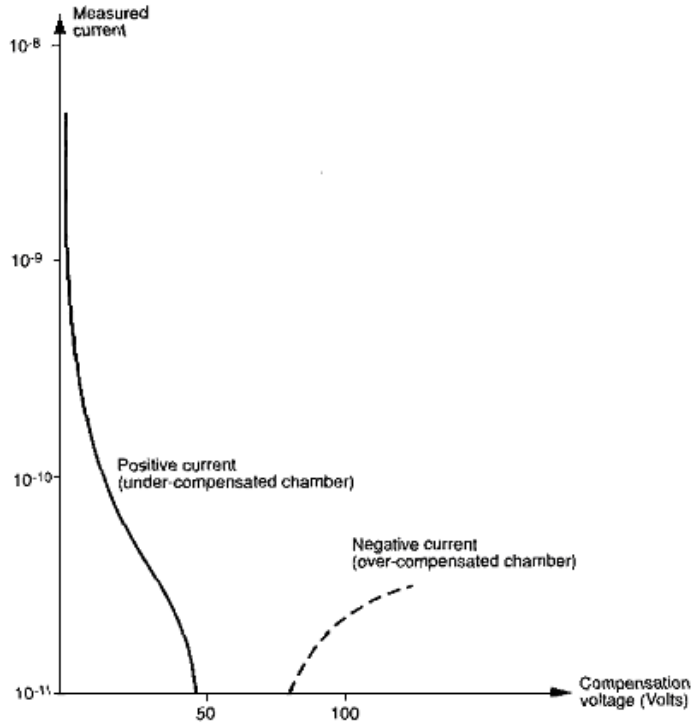

FIG. 14. Typical plot of a compensation curve.

3.1.2. Experimental procedure

- To perform this experiment the reactor is operated at three different power levels. For example, at 10 W, 1 kW, 10 kW, the positive high voltage is increased in steps. The resulting chamber current is recorded until the plateau is reached. The compensating high voltage is kept constant using I&C system. The typical example of the experimental results has been shown in Figure 15. Table 14 can be used for this part of the experiment.

- At fixed positive and negative high voltage the reactor power is increased in steps and the chamber current is recorded.
- Table 15 is suggested for these measurements.

TABLE 14. CHAMBER CURRENT AS A FUNCTION OF + HV AND REACTOR POWER

+ HV	Reactor power 10 W (current A)	Reactor power 1 kW (current A)	Reactor power 10 kW (current A)
+4			
+5			
+6			
+7			
+8			
+9			
+10			
+20			
+30			
+40			
+50			
+100			
+150			
+200			
+300			
+400			
+500			

TABLE 15. CHAMBER CURRENT AS A FUNCTION OF REACTOR POWER.

+HV set at: ..... V -HV set at: V

Reactor power	current [A]
10 W	
100 W	
1 kW	
10 kW	
25 kW	
100 kW	
250 kW	

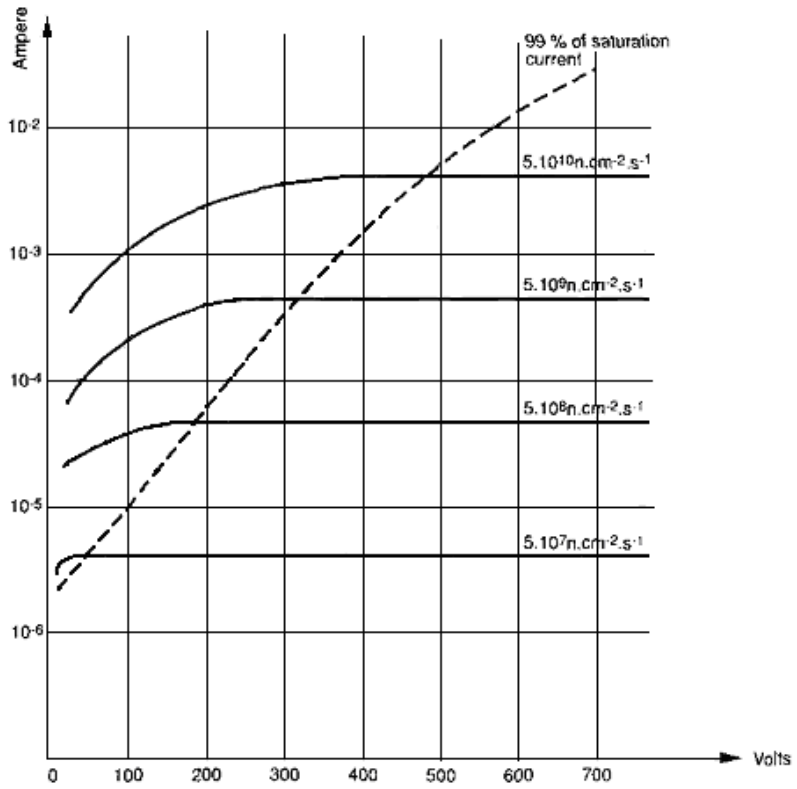

FIG. 15. Saturation curve diagram.

3.1.3. Safety precautions

This experiment is performed in the control room. Therefore the following radiation protection measures are obligatory for each participant:

- Personal dosimeter for each course participant provided by the health physics group;
- Spend as little time as possible in the controlled area;
- Each course participant should wash his/her hands after the completion of the experiment and should check for possible contamination using a hand-foot monitor.

3.2. NEUTRON FLUX DENSITY MEASUREMENT WITH FISSION CHAMBERS

3.2.1. Theoretical background

A wide variety of fission chambers use neutron-induced fission to detect neutrons. They are usually similar in construction to ionisation chambers, except that the coating material is highly enriched ^{235}U. The neutrons interact with the ^{235}U to cause fission. One of the two fission fragments enters the chamber, while the other fission fragment embeds itself in the chamber wall. The fission chamber has a similar structure to that of an ionisation chamber. The main differences between fission and ionisation chamber are:

- The electrode deposit is made of a small amount (approximately 1 mg) of 93% enriched uranium;
- The neutron interaction with uranium results in a fission process with a much higher reaction energy than with the neutron-boron interaction;

- The interaction of the chamber with gamma radiation is smaller, therefore FC can be readily applied to detect a small amount of neutrons in a high gamma background field (i.e. in the reactor shutdown or start-up mode, reactor power level below 10 W) etc.;
- Using a pulse height discriminator, the small pulses from gamma interaction can be filtered away from the large neutron induced pulses;
- The typical neutron sensitivity is from 10^{-14} A/nv to 10^{-12} A/nv;
- Fission chambers can be operated either in pulse mode or in current mode; in special cases they could also use current fluctuations (Campbell mode).

One advantage of using ^{235}U coating rather than boron is that the fission fragment has a much higher energy level than the alpha particle from a boron reaction. Neutron-induced fission fragments produce many more ionisations in the chamber per interaction than the neutron-induced alpha particles. This allows the fission chambers to operate in higher gamma fields than an uncompensated ion chamber with boron lining. Fission chambers are either used in current mode or pulse mode. They are especially useful as pulse chambers, due to the very large pulse size difference between neutrons and gamma rays. Because of the fission chamber's dual use, it is often used in 'wide range' channels in nuclear instrumentation systems. So-called Campbell detectors using specially isolated FC are capable of operating from the source range up to full reactor power.

In research reactors and small nuclear power plants, fission chambers are positioned outside around the core to monitor the neutrons (Figures 16 and 17). In large nuclear power plants the information collected from outside the core on the neutron flux density distribution inside the core is not sufficient; therefore miniature FC's have been developed to be positioned inside the core. These miniature FC(s) are the size of a pencil and are usually positioned in tubes entering the core from the top or bottom. In large nuclear power plants there may be typically around 100 to 200 such FC's distributed inside the core. The signals are collected and evaluated in a computer system to optimise the power distribution, but the signals may also be used for fast reactor shut-down in case of any power deviation from demand power.

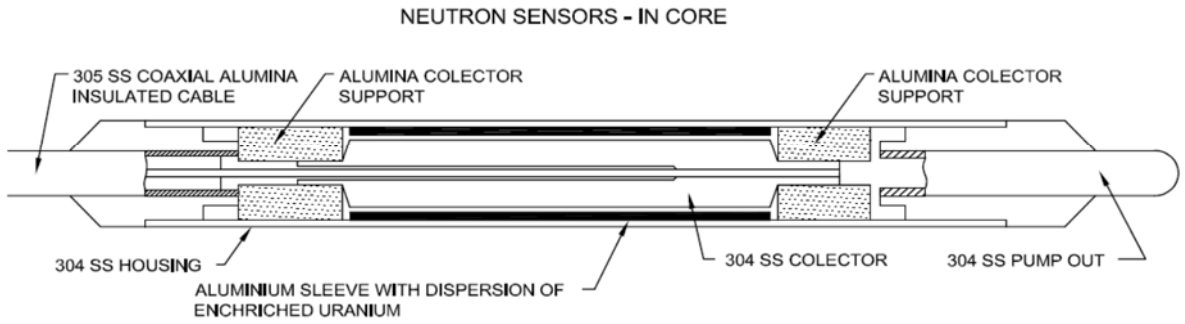

FIG. 16. Cross-section of a miniature in-core fission chamber.

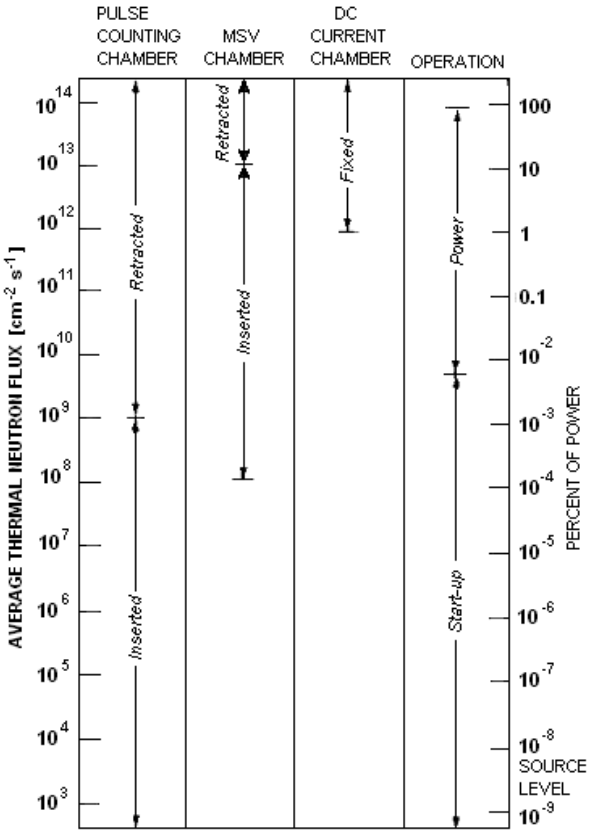

FIG.17. Ranges of in-core fission chambers.

3.2.2. Experimental procedure

While the reactor is shut down and the neutron source is removed from the core (no neutrons available for detection) the pulses of the fission chamber (gamma background and noise) are counted as a function of the discriminator setting. The discriminator is then set at the position when no more pulses are counted. Table 16 can be used for the results of this experiment.

(1) The neutron source is inserted into the core, the reactor is operated at a low power level (1 W) and the FC is lowered to the bottom of the guide tube.
(2) The counts are registered for about 30 s (three times calculating the average count rate).
(3) The FC is removed in 10 cm steps from the core. The measurement is repeated until the FC is so far away from the core that no more counts are registered.
(4) Table 17 is suggested for this part of the experiment.

When the reactor is shut down, the count rate of the FC as a function of time is measured to follow the neutron flux density decrease. Table 18 can be used for this experiment.

TABLE 16. FISSION CHAMBER COUNT RATE AS A FUNCTION OF THE DISCRIMINATOR SETTING TYPE FC 165

Discriminator setting	Counts per 30s
0	
1	
1.5	
2	
2.5	
3	
3.5	
4	

TABLE 17. RANGE OF NEUTRONS IN THE CORE REGION USING A FISSION CHAMBER FC 165

Position from core mid-plane [cm]	Counts per 30s
0	
+10	
+20	
+30	
+40	
+50	
+60	
+70	
+80	
+90	
+100	

TABLE 18. NEUTRON COUNT RATE AFTER REACTOR SHUT DOWN

Staring time in seconds after reactor shut down Measuring time 10 s	Count rate per 10 s
0-10	
30-40	
60-70	
90-100	
210-130	
150-160	
180-190	
210-220	

3.2.3. Safety precautions

This experiment is performed in the control room. Therefore the following radiation protection measures are obligatory for each participant:

- Personal dosimeter for each course participant provided by the health physics group;
- Spend as little time as possible in the controlled area;
- Each course participant should wash his hands after the completion of the experiment and should check for possible contamination using a hand-foot monitor.

3.3. NEUTRON FLUX DENSITY MEASUREMENT WITH SELF-POWERED NEUTRON DETECTORS

3.3.1. Theoretical background

The principle of measuring neutron-induced electrons through (n,β) reaction was known and patented in early 1938. Neutron detectors operating without any external voltage were reported in 1961, but the practical application in neutron flux measurement techniques was first reported in 1964. During the following years a large number of papers on self-powered neutron detectors were published. As these detectors operated without any external voltage, they were called self-powered neutron detectors (SPND).

Most of the new emitter materials were developed between 1969 and 1974. Besides the most important emitter materials Co, Rh and V, other emitter materials such as Ag, Al, Au, B, Ce, Er, Gd, Hf, Pd, Pt, Os, Ta, Ti, W and Yb were also investigated. Another part of the developmental work concentrated on new geometric detector forms where detector bundles with different emitter lengths were used to measure the axial power distribution in the core. The characteristics data of some common emitter material is given in Table 19.

TABLE 19. SOME CHARACTERISTIC DATA OF β–EMITTER MATERIALS

Isotope	Natural abundance (%)	Neutron cross-section (b)	Half-life	Maximum β-decay MeV	Burn up in % per month at 10^{14} /cm^2/s
^{27}Al	100	0.23	2.3 min	2.9	0.006
^{107}Ag	48.65	35	2.3 min	1.8	0.9
^{109}Ag	51.35	89	24 s	2.8	2.3
^{11}B	80.2	0.005	0.02 min	13.4	
^{51}V	99.76	4.8	3.76 min	2.5	0.12
^{103}Rh	100	150	4.4 min/42 s	2.5	3.9
^{59}Co	100	37	10^{-14} s	-	1.0
^{55}Mn	100	13.3	2.58 h	2.8	0.34

Isotope	Natural abundance (%)	Neutron cross-section (b)	Half-life	Maximum β-decay MeV	Burn up in % per month at 10^{14} /cm^2/s
^{7}Li	92.6	0.037	0.85 s	13.0	
Natural Er	100	162			4.0
Natural Hf	100	102			3.2
Natural Pt	100	10			0.25

The most common detector form is a coaxial cylinder with an emitter in the centre which is surrounded completely by an insulator. The outer sheath acts as case and collector as shown in Figures 18 and 19. The detector geometry can be adapted for special applications; small plates, hooks or spirals are offered by the industry. Table 19 gives a summary of commonly used emitter materials for self-powered neutron detectors.

The emitter material must have an appropriate neutron absorption cross-section, which is usually a compromise between detector sensitivity and detector burn-up. The detector signal decreases with burn-up and the burn-up rate depends mainly on the absorption cross-section of the emitter and local flux density values. Other emitter material selection criteria are the energy of the radiation emitted after a neutron capture, the half-life of the produced nuclides, their daughter products and the melting point. According to these criteria the complete nuclide chart has been searched for possible emitter materials and the most common nuclides are given in Table 19.

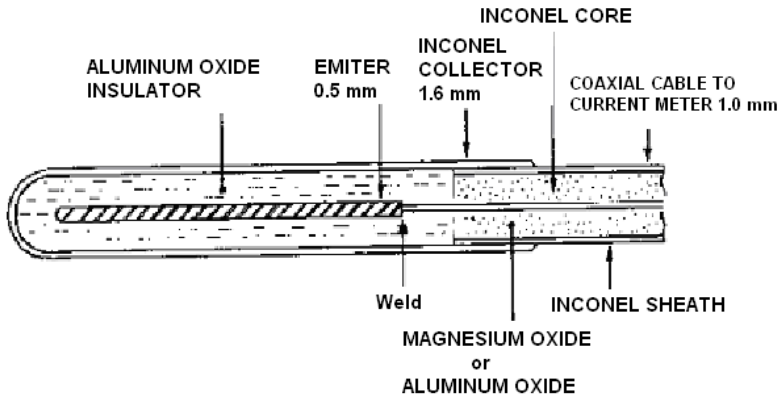

FIG. 18. Cross-section of a self-powered neutron detector.

The insulator usually consists of a high-temperature resistant material (like Al_2O_3) and must have a thickness that allows the produced electrons ((n, γ) (γ, e)) to reach the collector. An optimisation of the detector geometry, especially the emitter diameter and the insulator thickness, is necessary.

The collector has to collect the emitted electrons and gives the detector its mechanical stability. It must be corrosion resistant and should not undergo dimensional changes at high temperatures. After a neutron capture in the emitter a ((n,γ) (γ,e)) reaction produces electrons. The constant loss of electrons from the emitter produces a current between emitter and collector, which can be measured directly by an ammeter. The current is proportional to the rate of absorption of neutrons in the emitter and thus proportional to the local neutron flux. A typical detection sensitivity is 10^{-21} A/nv.

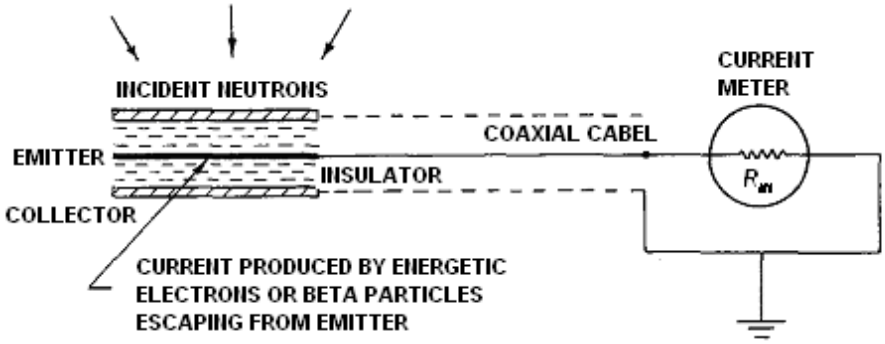

FIG. 19. Scheme of a self-powered neutron detector.

In some emitter materials the electrons are produced with a time delay according to the half-life of the nuclide. Therefore the detector gives a delayed response to a neutron flux variation and a constant signal is measured only after the saturation activity of the emitter material has been reached. Typical delayed self-powered neutron detectors are Rh and V detectors, which have a response time of several minutes. For this reason they cannot be used in the reactor protection system as shown in Figure 20.

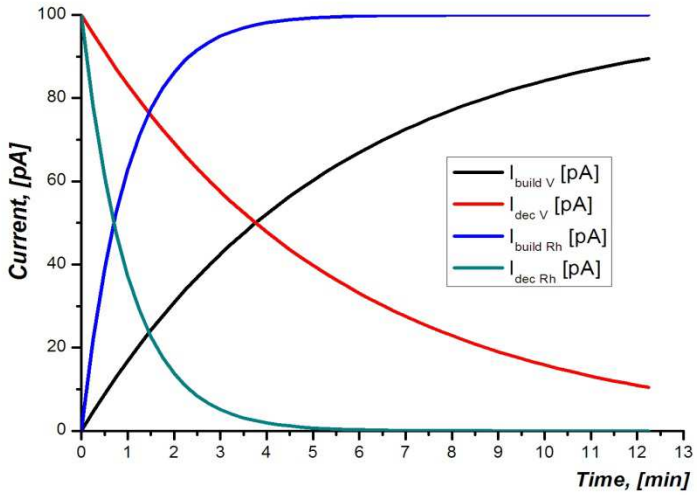

FIG. 20. SPND response to step change in neutron flux.

If the ((n, γ) (γ, e)) reactions take place immediately (i.e. 10^{-14} s for a Co detector), the detector responds promptly to any neutron flux change and can be used in the reactor protection system. As the prompt self-powered neutron detectors are very important for power reactor instrumentation, the signal composition will be analysed more closely.

The main part of the signal is prompt and is produced by the reaction $^{59}Co(n, \gamma)^{60}Co$. In addition, heavier nuclides like ^{60}Co and ^{61}Co are produced in the emitter material. The gamma radiation emitted from this nuclear reaction produces electrons in the emitter by photo, Compton, pair-production processes or by internal conversions, which penetrates the insulator and are collected by the collector. Now the prompt signal $I_{pr,n}$ resulting from the direct nuclear reaction has to be distinguished from the delayed signal I_β from the produced heavier isotopes. These isotopes usually emit β-radiation and delayed gamma radiation, both producing an unwanted delayed detector signal together with the prompt signal.

The other sources of radiation disturbances are neutron capture gamma rays from the reactor core and the prompt ($I_{pr,\gamma}$) and delayed ($I_{del,\gamma}$) gamma radiation from nuclear fission. These

radiation components penetrate the detector and cable from outside and produce secondary electrons registered as detector noise.

The polarity of this noise signal depends on the atomic numbers of collector, insulator and emitter. Therefore, the total detector signal is composed of three parts, namely $I_{tot} = I_{pr,n} + I_{pr,\gamma} + I_{del,\gamma} + I_{\beta}$. From the above mentioned components contained in $I_{pr,\gamma}$ one component (prompt gamma radiation from fission) depends on the fission rate. The component from neutron capture gamma rays depends on the location where the detector is installed in the reactor core. Therefore, $I_{pr,\gamma}$ depends on the reactor type and detector core position. For one special location of a new Co detector, $I_{pr,n}$ is about 83% and $I_{pr,\gamma}$ about 17% of the total signal. For other emitter materials these values depend on the atomic number of the emitter. The composition of the two different noise signals ($I_{del,\gamma}$ and I_{β}) can accidentally produce a total signal I_{tot}, which may be approximately constant over several years even if the true detector signal $I_{pr,n}$ decreases according to the detector burn-up. Thus the signal to noise ratio is decreased while the total signal is constant. The behaviour of I_{tot} depends very much on the local neutron flux and the above mentioned effects of burn-up compensation by the creation of noise signals, and is predominant at a flux level of about 1×10^{14} $cm^{-2} \cdot s^{-1}$. From a safety point of view this effect is not acceptable; therefore, a periodic calibration of the detector signal as well as an investigation of its composition is necessary. This can be done either during reactor operation with movable detector systems or during reactor shutdown periods when the prompt detector signal is zero.

3.3.2. Experimental procedure

A SPND is installed in the centre of the reactor core and the reactor is started to a power level of 30 to 50 kW. According to the selected emitter material the current of the SPND will increase due to the activation of the emitter material. It takes about 10 half-lives until a constant signal is obtained. Then the reactor is shut down and the decrease of the signal is observed, which again depends on the half-life of the emitter material. From these values the emitter material can be identified.

3.3.3. Safety precautions

This experiment is performed in the control room. Therefore the following radiation protection measures are obligatory for each participant:

- Personal dosimeter for each course participant provided by the health physics group;
- Spend as little time as possible in the controlled area;
- Each course participant should wash his/her hands after the completion of the experiment and should check for possible contamination using a hand-foot monitor.

4. ACCELERATOR APPLICATIONS EXPERIMENTS

4.1. STOPPING POWER OF LIGHT IONS IN SOLID MATERIALS

4.1.1. Theoretical background

Energetic ions lose energy when passing through materials due to Coulomb interactions with atomic electrons and nuclei. At MeV ion energies, the dominant energy loss mechanism is through interactions with electrons (electronic stopping power). At keV and lower energies, the transfer of energy to the atomic nuclei becomes more important (nuclear stopping power). The sum of these two energy loss processes is the total stopping power *S(E)*, which is defined as the rate of energy lost per unit distance:

$$S(E) = \frac{dE}{dx} \tag{57}$$

In the MeV energy region, nuclear stopping only contributes a few percent to total stopping power. In this region, the electronic stopping power *S(E)* is described by the Bethe-Bloch equation [12, 13]:

$$S(E) = 4\pi r_0^2 mc^2 \frac{Z_1^2}{\beta^2}\frac{Z_2}{M_2} N_A \ln\left(\frac{2mc^2}{I}\beta^2 - U\right) \tag{58}$$

$$\beta = \frac{v_1}{c}$$

Where r_0 is the classical electron radius (2.8 fm), Z_1 and Z_2 are the projectile and target atomic number, M_2 the mass of the target atom, N_A Avogadro's number, I the mean ionisation potential of the target material, U a shell correction factor, and β the ratio of projectile speed to the speed of light.

In practice, a semi-empirical model of stopping powers is used SRIM [14], which uses best-fits on experimentally measured data. This freely-available and widely-used software is used to calculate stopping powers for different ion/material combinations. For this experiment, the stopping power of protons in aluminium is used, with the calculations of SRIM plotted in Figure 21.

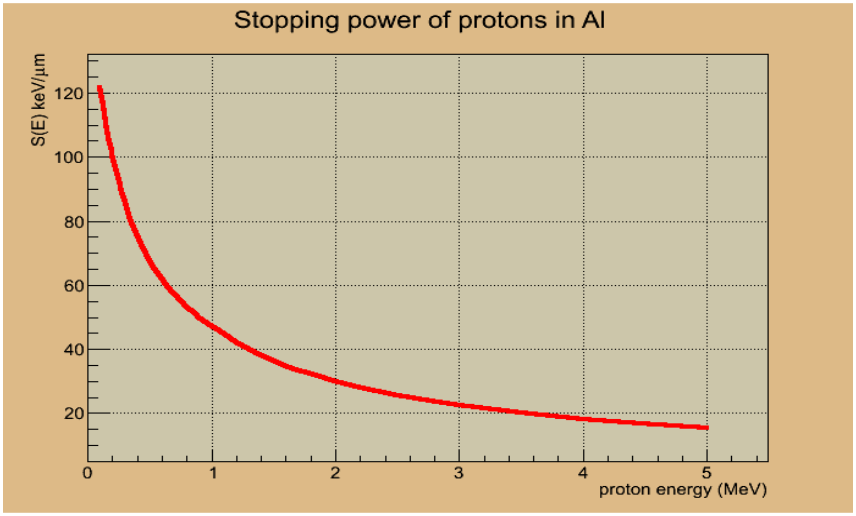

FIG. 21. Stopping power of protons in aluminium calculated by SRIM.

A commonly encountered experimental situation is shown in Figure 22. An ion beam of energy E_0 traverses a material of thickness Δx, exiting with an energy loss of ΔE.

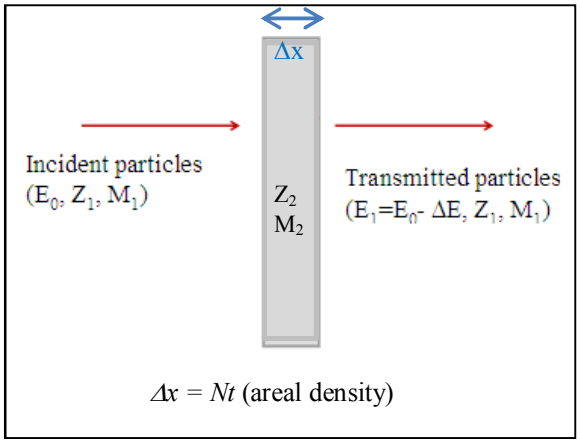

FIG. 22. Schematic diagram of the incident ion (Z_1, M_1) passing through a homogeneous material with thickness Δx composed of atoms with atomic number Z_2 and mass M_2.

The energy E_1 of the ion after passing through the thickness Δx is given by Eq. (59):

$$E_1 = E_0 - \Delta E = \int_0^x \frac{dE}{dx}\,dx \tag{59}$$

To find the material thickness Δx producing a given energy change ΔE, one must invert $\frac{dE}{dx}$ and integrate over energy:

$$\Delta x = \int_{E_1}^{E_0} \left(\frac{dE}{dx}\right)^{-1} dE \tag{60}$$

This integration can be done numerically or by slab analysis. For thin targets in which $\frac{dE}{dx}$ does not significantly change as the ion beam passes through the material, the stopping power can be taken as a constant and to be that value at the surface of the material. Eq. (60) thus becomes:

$$\Delta x = \frac{\Delta E}{\left(\frac{dE}{dx}\right)_{E=E_0}} = \frac{\Delta E}{S(E_0)} \tag{61}$$

4.1.2. Experimental procedure

The measurements must be carried out in a vacuum chamber. The chamber should be light-tight as the charged particle detector is sensitive to light (when bias is applied). In the experiment shown in Figure 23; 2 MeV protons are scattered from a (95 ± 5) nm thick, self-supporting gold target (d_{Au}=184 μg/cm^2) into a particle detector placed at an angle of 45°.

These scattered protons are incident on a foil of unknown thickness. The transmitted protons are detected in the particle detector. The measured energy spectra are shown in Figure 24.

The energy loss of beam particles in the foil should be smaller than the energy resolution of the particle detector (~ 15 keV). The diameter of the incident beam on the target was 3 mm, and the proton beam current is kept below 10 nA during the measurement. Two options for the experimental setup are shown in Figure 23.

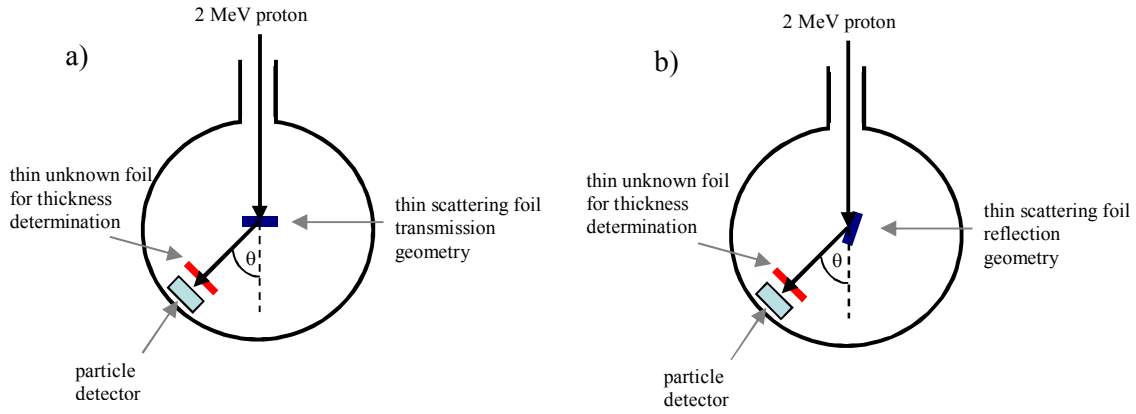

FIG. 23. Setup of the experiment for foil thickness determination: a) with a scattering foil in the transmission geometry, b) with a scattering foil in the reflection geometry.

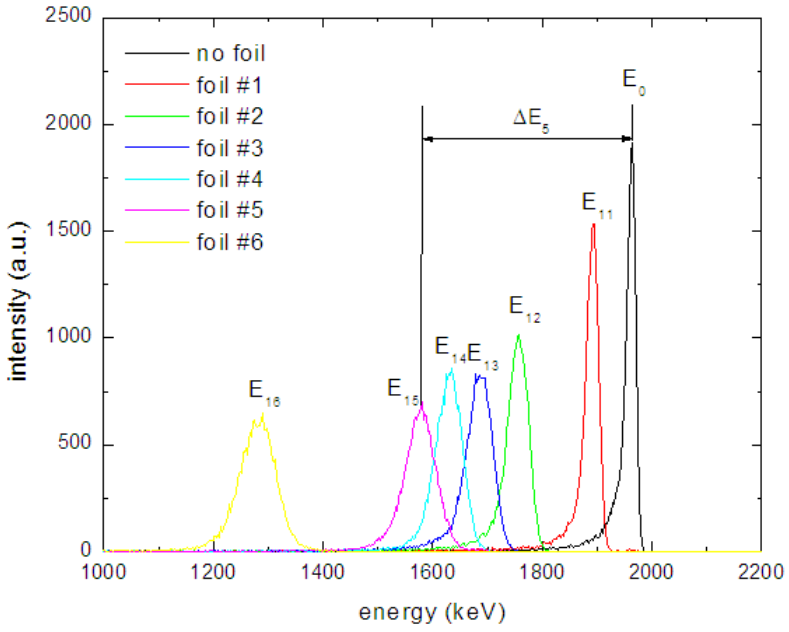

FIG. 24. Energy spectra of 2 MeV protons scattered from thin gold foil after passing through aluminium foils of different thicknesses and scattered with no foil in front of detector (black line).

The final energy of the ion after passing through the thin aluminium foil can be found from the peak position in the energy spectrum, as shown at Figure 24. First, the position and the width of the peak in the energy spectrum of 2 MeV protons scattered from the thin Au foil is measured using the particle detector. This defines the initial condition E_0. Next, foils of

different thicknesses are placed in front of the particle detector. The peak position and its width are determined for each foil. It is assumed that the energy calibration of the particle detector is well-known. If not, it should be done before measurement e.g. by measuring forward scattering spectra from the thin gold foil at a minimum of two different proton energies and constructing a linear calibration using the reaction kinematics.

Aluminium foils have been used for these measurements; however, more readily available thin foils of other materials (e.g. Mylar™ or Kapton™) can be used. The prerequisite condition is that the foils are thin enough so that 2 MeV protons can be transmitted through them into the detector. Different thicknesses can be obtained by adding together different combinations of the available thin foils. The areal density of the thin foils can be determined by precise weighing and measurement of the foil area. The foil density (g/cm^3) should be known to obtain a nominal physical thickness. These foil thicknesses will be compared with those determined from the energy loss experiment.

In this experiment, 6 aluminium foils of different thicknesses are measured, as shown in Figure 24. The thickness of foils #3 - #6 was determined by weighting, while the thicknesses of foils #1 and #2 were given by the foil supplier. All spectra were accumulated to the approximately same number of detected protons. The peak in the energy spectrum of 2 MeV protons forward scattered from the gold foil (black line) and detected by the particle detector is defined by the position of energy E_0. Subsequently, spectra are recorded with different aluminium foils placed in front of the particle detector. The energy E_{1n} when foil #n is placed in front of particle detector is denoted in Eq. (62):

$$E_{1n} = E_0 - \Delta E_n \tag{62}$$

Here ΔE_n is the energy loss of protons in the n^{th} foil as is shown on Figure 24.

The foil thicknesses determined from the stopping power measurements, together with the thicknesses that are given by foil suppliers or weighed, are given in Table 20. The average uncertainty is dominated by uncertainty in the stopping power (< 4% for H in Al) and uncertainty in the centroid position of the peak to be < 7%.

TABLE 20. COMPARISON OF THICKNESSES OF DIFFERENT Al FOILS FROM ENERGY LOSS MEASUREMENTS IN COMPARISON WITH FOIL THICKNESSES GIVEN BY FOIL PRODUCERS OR FROM WEIGHT MEASUREMENTS (1 μm Al = 6024 × 10^{15} at/cm^2)

Foil #	ΔE (keV)	t_{Al} (10^{15} at/cm^2)	t_{Al} (from Eq. (61)) (μm)	t_{Al} (from Eq. (60)) (μm)	t_{Al} (from weight or supplier) (μm)
1	70.5	13930	2.3	2.3 ± 0.2	2.0 ± 0.1
2	206.9	39860	6.9	6.6 ± 0.5	5.0 ± 0.3
3	276.9	52660	9.2	8.7 ± 0.6	8.5 ± 0.4
4	331.7	62430	11.1	10.3 ± 0.7	10.2 ± 0.5
5	383.9	71530	12.8	11.9 ± 0.8	11.7 ± 0.7
6	680.7	119550	22.7	19.8 ± 1.4	19.3 ± 1.0

For the thinnest foil, foil #1, the energy loss ΔE is 70.5 keV and using S(2000 keV) = 29.93 keV/μm, the calculated thickness is 2.36 μm using the surface approximation (Eq. 61). This result is in very good agreement with that given by the foil supplier. It is seen that as the foil

thickness increases the surface approximation becomes less valid. Better agreement is obtained if changes in the stopping power are taken into consideration and used in a more exact calculation (Eq. 60).

As can be seen in Figure 24, the transmitted energy spectra become Gaussian-shaped and broader as the foil thickness increases (i.e. energy loss becomes larger). This effect is energy straggling, which arises from the statistical nature of the energy loss process. By fitting the experimental energy spectra (not including the long tails) with a Gaussian function to determine the standard deviation of the energy distributions, one can extract the contribution of the energy loss straggling in the foil from other energy degrading contributions (such as detector energy resolution, or geometrical effects).

The Bohr theory of energy straggling [15] yields the equation:

$$\Omega_B^2 = 0.26 Z_1^2 Z_2 Nt\left[10^{18} at/cm^2\right] \tag{63}$$

Where Ω_B is the energy standard deviation and Nt is the target areal density. The standard deviation Ω relates to the FWHM δE through the relation:

$$\delta E = 2.355\Omega \tag{64}$$

Example: Using Eqs. (63) and (64), 2 MeV protons transmitted through 10 μm Al have a FWHM δE of approx. 33 keV.

The measured experimental energy width δE_{exp} is comprised of all the different energy broadening effects added together in quadrature. For an ideal foil:

$$\delta E_{exp}^2 = \delta E_0^2 + \delta E_B^2 + \delta E_{det}^2 \tag{65}$$

Where δE_0 is the width of the incident proton beam, δE_B the Bohr straggling width and δE_{det} the detector energy resolution (a few keV). Experimental values obtained for δE_B from Eq. (65) are compared with the Bohr formula Eqs. (63) and (64), and are given in Table 21.

TABLE 21. EXPERIMENTAL AND CALCULATED BOHR ENERGY STRAGGLING

Al thickness (μm)	δE_B (experimental) keV FWHM	δE_B (calculated) keV FWHM
2.3 ± 0.2	20.0	16.2
6.6 ± 0.5	38.9	27.5
8.7 ± 0.6	51.8	33.4
10.3 ± 0.7	53.7	36.4
11.9 ± 0.8	66.5	40.0
19.8 ±1.4	78.5	55.5

Bohr straggling in Eq. (63) depends on the target thickness, but not on the ion energy. This description is valid in cases where the energy loss of ions in the target is large enough that the energy distribution can be described by a Gaussian shape, and small energy loss compared to the incident energy, i.e. when $0.01 < \Delta E/E < 0.2$. This condition is fulfilled for all foils except foil #6. From Table 21 it is seen that the experimentally obtained values for energy straggling are up to 60% larger than values predicted by Bohr's theory in the region where Bohr's theory should be valid (foils #1 - #5). Other theories were developed within the energy validity

region of the Born approximation such that of Livingston and Bethe [16], but they are not considered here. The difference between experiment and theory can partly be due to other effects arising from differences between a perfect foil and a real foil, such as material inhomogeneity and surface roughness, and other energy degrading terms not included in Eq. (65).

4.1.3. Recommended equipment

- A sample holder in front of the particle detector to hold thin foils for stopping power measurements;
- Thin foils of known areal density;
- A thin high-Z foil for scattering proton beam into detector;
- A particle detector placed at front angles and corresponding electronic chain with multichannel analyser;
- SRIM or SIMNRA software.

Thin foils are very fragile and should be handled with care to avoid breakage. Evacuating the vacuum chamber quickly with a rotary vacuum pump can cause a fast movement of air which also can break the foils. The roughing evacuation should be done slowly.

4.1.4. Safety precautions

The proton beam can produce high yields of X rays from collimators and beam-defining apertures if high currents are used and large amounts of the proton beam are incident on these beam trajectory defining components. A radiation survey should be made prior to undertaking measurements and if necessary, use the appropriate shielding and working distance to minimise any potential exposure risks.

4.2. NON-RUTHERFORD SCATTERING NEAR THE $^{12}C(p,p)^{12}C$ RESONANCE ENERGY

At ion energies above the Coulomb barrier, cross-sections for elastic backscattering are strongly dependent on ion energy, and deviate significantly from the classical Rutherford formula. For the elastic scattering reaction $^{12}C(p,p)^{12}C$ there is a resonance in the cross-section with peak maximum positioned at 1734 keV and FWHM of ~ 40 keV. As non-Rutherford cross-sections can be much higher (in some cases up to 100 times) than Rutherford ones, this can be utilised in practical applications to increase the analytical sensitivity of the backscattering technique. The intense resonance for ^{12}C or ^{16}O with helium ion beam is a commonly-used tool for depth-profiling carbon and oxygen in various substrates [17, 18].

4.2.1. Theoretical background

In this experiment, the yield of protons backscattered from a thin carbon foil is measured as a function of the proton energy (calculated from the magnetic field of the analysing magnet) in the energy range from 1610–1810 keV. The cross-section is calculated from the yield measurements.
The differential cross-section for backscattered protons at a scattering angle θ is given by Eq. (66):

$$\frac{d\sigma_C}{d\Omega}\left(E-\frac{\Delta E_C}{2},\theta\right)=\frac{A_C}{Q\Omega(\theta)N_C} \tag{66}$$

Where E is incident proton energy, ΔE_C is energy loss in the carbon film, A_C is the area under the carbon peak (yield), Q is the number of incident protons, $\Omega(\theta)$ the detector solid angle and N_C the number of carbon atoms per unit area (atoms/cm^2). The energy loss of protons ΔE_C in the 20 μg/cm^2 carbon foil used in this experiment was calculated using SRIM [14] as ~4 keV. The energy of the protons in the carbon foil is taken as that at the middle of the foil.

4.2.2. Experimental procedure

Figure 25 shows the experimental geometry. The measurements must be carried out in a vacuum chamber. The chamber should be light tight as the charged particle detector is sensitive to light (when bias is applied). A collimated proton beam with energy varied from 1600 to 1800 keV is incident on a thin carbon foil (10-20 μg/cm^2). A particle detector is placed at a backward angle (135°-170°) to detect the backscattered protons. The proton beam transmitted through the carbon foil is collected in a reliable Faraday Cup. The backscattering yield for the ^{12}C(p,p)^{12}C reaction is measured between 1610 keV and 1810 keV in steps of 10 keV.

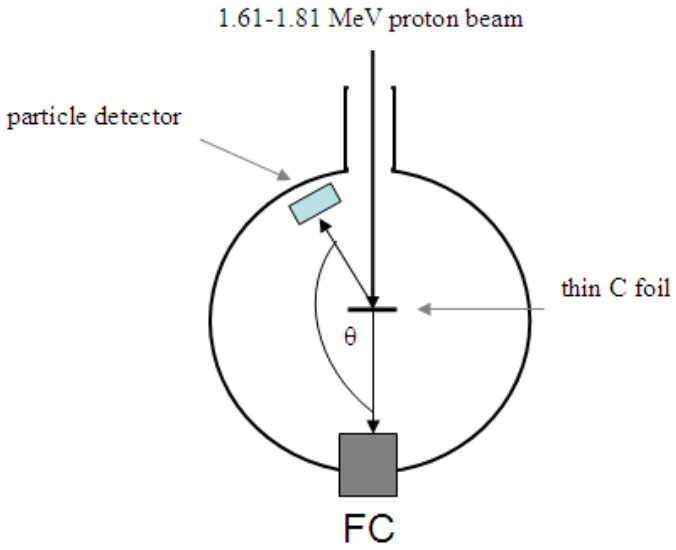

FIG. 25. Experimental setup for backscattering of protons from the 20 μg/cm^2 carbon foil.

All spectra are collected to the same number of incident particles i.e. to the same collected charge in the Faraday Cup (Q = 0.5 μC in this case). It is important that the target is as thin as possible to avoid the broadening of the narrow resonance. In this case, the energy loss of 1610–1810 keV protons in a 20 μg/cm^2 carbon is ~ 4 keV, which is 10% of the resonance FWHM. The spectrum of protons backscattered from the carbon foil for several proton energies is shown in Figure 26. It is clear that yield is very sensitive to the incident proton energy.

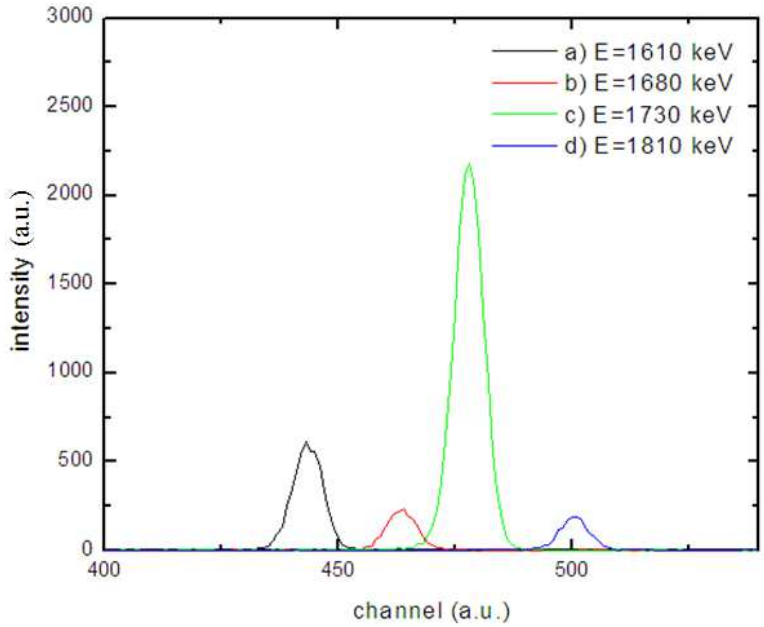

FIG. 26. Backscattering spectra of protons from a thin carbon foil for several incident energies: a) 1610 keV, b) 1680 keV, c) 1730 keV and d) 1810 keV. All spectra are normalised to the same number of incident protons (Q = 0.5 μC).

If the solid angle of particle detector is not known, absolute cross-section values cannot be calculated and only relative cross-section values obtained. The solid angle can be determined from a backscattering spectrum of heavy element such as Au, W, etc. for which cross-sections are pure Rutherford. For this system, $\Omega(\theta)$ is (7.6 ± 0.3) msr. For 0.5 μC the number of incident particles is 3.125×10^{12} protons. N_c for 20 μg/cm^2 carbon foil is 1000×10^{15} at/cm^2.

The measured differential cross-sections for $^{12}C(p,p)^{12}C$ scattering at 165° are shown on Figure 27 together with the evaluated cross-sections using SigmaCalc program from IBANDL [19], and cross-sections calculated using the Rutherford formula. The data is tabulated in Table 22. It can be seen that the Rutherford cross-section is completely erroneous for this reaction. Also, the present measurements are energy-shifted ~8 keV towards higher energies and could be attributed to a small inaccuracy in the accelerator energy calibration.

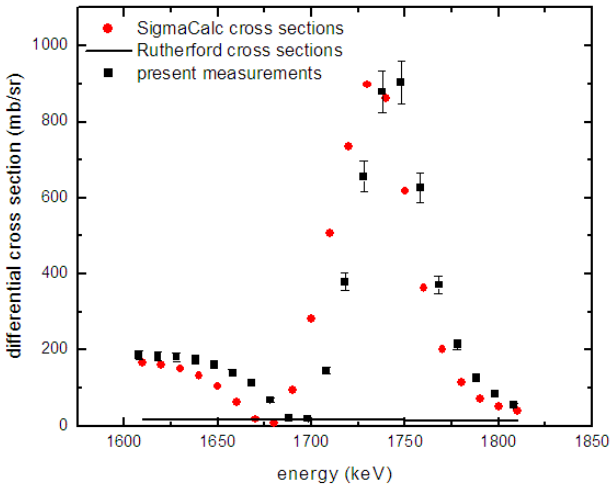

FIG. 27. Differential cross-sections for proton scattering from carbon at 165°.

The evaluated cross-sections are those obtained from the parameterisation of all the available experimental data for this reaction in the framework of nuclear physics models to obtain a set of best and recommended cross-section values. According to SigmaCalc, the cross-section resonance maximum is at 1734 keV.

The uncertainty in the calculated cross-section is ~ ± 7%, arising from:

- the statistical errors of the number of counts (peak areas) for backscattered protons;
- charge collection error 2%;
- solid angle determination 3%;
- target thickness 5%.

TABLE 22. DIFFERENTIAL CROSS-SECTIONS FOR $^{12}C(p, p)^{12}C$ AT 165°, MEASURED VALUES, SigmaCalc AND RUTHERFORD VALUES

E (keV) experimental	A_c	σ (mb/sr) present measurements	E (keV) tabulated	σ (mb/sr) SigmaCalc	σ (mb/sr) Rutherford
1608	4875 ± 70	186 ± 12	1610	167	18.4
1618	4793 ± 79	183 ± 12	1620	161	18.1
1628	477 0± 69	182 ± 12	1630	151	17.9
1638	4570 ± 68	174 ± 11	1640	133	17.7
1648	4241 ± 65	162 ± 10	1650	105	17.5
1658	3683 ± 61	140 ± 9	1660	64	17.3
1668	2978 ± 55	114 ± 7	1670	18	17.1
1678	1801 ± 43	69 ± 5	1680	8	16.9
1688	556 ± 25	21 ± 2	1690	95	16.7
1198	520 ± 23	20 ± 2	1700	281	16.5
1708	3846 ± 62	147 ± 9	1710	508	16.3
1718	9959 ± 100	380 ± 24	1720	735	16.1
1728	17217 ± 131	656 ± 41	1730	898	15.9
1738	23071 ± 152	879 ± 55	1740	862	15.7
1748	23740 ± 152	904 ± 56	1750	618	15.6
1758	16473 ± 129	628 ± 39	1760	364	15.4
1768	9751 ± 99	372 ± 23	1770	202	15.2
1778	5640 ± 76	215 ± 14	1780	116	15.0
1788	3331 ± 58	127 ± 8	1790	72	14.9
1798	2202 ± 47	84 ± 5	1800	51	14.7
1808	1445 ± 39	55 ± 4	1810	41	14.5

4.2.3. Recommended equipment

- A sample holder with thin self-supporting carbon foil;
- A particle detector placed at any backscattering angle (135–170°);
- A preamplifier, bias supply, spectroscopy amplifier, ADC and MCA;
- SRIM.

Thin foils are very fragile and should be handled with care to avoid breakage. Note, that evacuating the vacuum chamber quickly with a rotary vacuum pump can cause a fast

movement of air which also can break the foils. The roughing evacuation should be done slowly.

4.2.4. Safety precautions

The proton beam can produce high yields of X rays from collimators and beam-defining apertures if high currents are used and large amounts of the proton beam are incident on these beam trajectory defining components. A radiation survey should be made prior to undertaking measurements and if necessary, use the appropriate shielding and working distance to minimise any potential exposure risks.

4.3. MEASUREMENT OF THE HYDROGEN CONCENTRATION IN THIN FILMS

The hydrogen content and depth profile in materials can be measured using the Elastic Recoil Detection Analysis (ERDA) method. In this method, an ion beam with mass greater than hydrogen (e.g. ^{4}He, ^{7}Li, ^{12}C ions) is used in a two-body collision to knock hydrogen atoms in a forward direction. The knocked-on hydrogen atoms and forward scattered ion beam are incident on a charged particle detector placed at a forward angle. A stopping foil is placed in front of the charged particle detector to stop the scattered ion beam and transmit the knocked-on hydrogen atoms. Heavy ions have larger stopping powers than protons, allowing the thickness of the stopping foil to be tailored to stop the heavy ions yet transmit the recoiled protons. In this experiment, the hydrogen content in a thin foil of the polycarbonate material Mylar™ will be measured and compared with that of 36 at.% from its known stoichiometry $C_{10}H_8O_4$.

4.3.1. Theoretical background

The experimental geometry is shown in Figure 28. A heavy ion beam of several MeV energy (in this experiment 10 MeV $^{12}C^{3+}$ ions) is incident on a polymer material such as Kapton™ ($C_{22}H_{10}N_2O_5$) or Mylar™ ($C_{10}H_8O_4$). Two possibilities for the positioning of the target exist as shown in Figure 28. For thin transmission targets and in cases when one wishes to measure the total amount of H, the transmission geometry as shown in Figure 28a) can be applied. For thin hydrogen containing layers on a thick substrate, and in cases when the depth distribution of hydrogen in the sample is to be measured, the target should be tilted as shown in Figure 28b) and reflection geometry should be used.

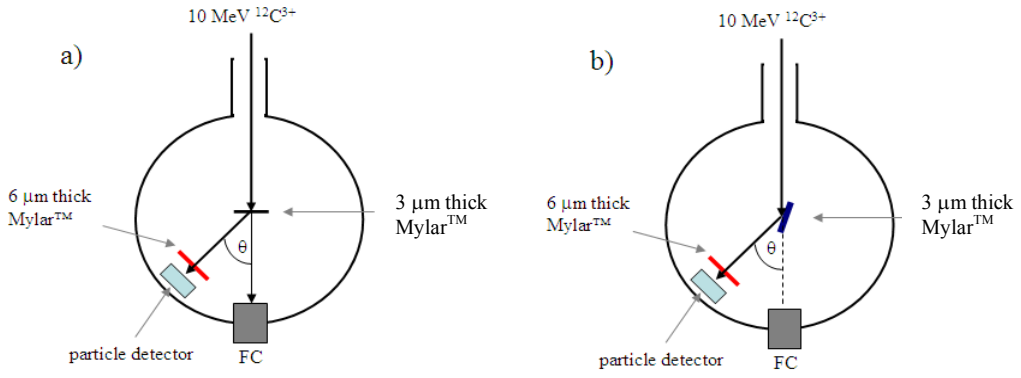

FIG. 28. Two possible configurations for the measurement of hydrogen content in the thin foil a) transmission and b) reflection geometry.

This experiment uses the transmission geometry shown in Figure 28a with the reaction kinematics shown in Figure 29.

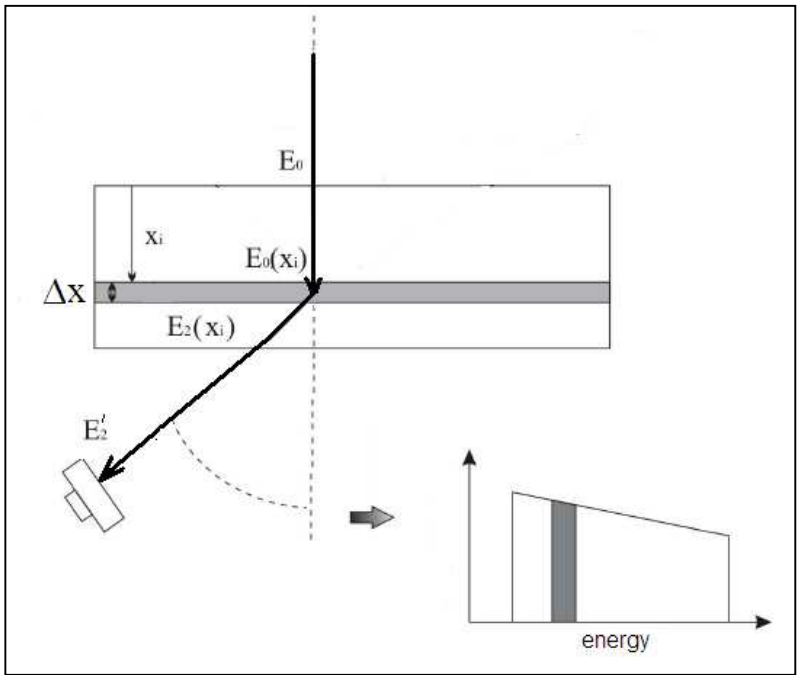

FIG. 29. Schematic presentation of the transmission geometry and idealised measured ERDA energy spectrum.

The incident ion beam with atomic number Z_1, mass M_1 and energy E_0 enters the sample under angle α (in our case and transmission geometry $\alpha=0$). At depth x_i, the incident ion has energy $E_0(x_i)$ given in Eq. (67):

$$E_0(x_i) = E_0 - \int_0^{x_i} \left(\frac{dE_0(x)}{dx} \right)_{in} dx \tag{67}$$

Where $\frac{dE_0(x)}{dx}$ is the stopping power of the ion beam in the sample.

At this depth x_i and energy $E_0(x_i)$, the incident ions recoil atoms j with atomic number Z_2 and mass M_2 into the solid angle $\Delta\Omega$ and angle β. The yield of recoiled atoms Y from this sub-layer Δx is given by Eq. (68):

$$\frac{dY}{dx}\Delta x = Q\Delta\Omega \frac{d\sigma(\bar{E}_0(x_i),\beta)}{d\Omega}\Delta x n_j \tag{68}$$

Where Q is the number of incident ions, n_j is atomic density of j atoms in the target, $\Delta\Omega$ is the solid angle, and $\frac{d\sigma(\bar{E}_0(x_i),\beta)}{d\Omega}$ is the differential cross-section for recoil of mass M_2 at energy $\overline{E_0}(x_i)$ in the layer Δx at x_i. In this experiment, the incident ion beam is ^{12}C and so the differential cross-section is described by the Rutherford formula Eq. (69):

$$\frac{d\sigma(\bar{E}_0(x_i),\beta)}{d\Omega} = \frac{\left[Z_1 Z_2 e^2 (M_1 + M_2)\right]^2}{\left[2M_2 \bar{E}_0(x_i)\right]^2 \cos^3\beta} \tag{69}$$

Note: If using alpha particles as the ion beam, the cross-section is non-Rutherford!

In the two-body collision of an incident ion of mass M_1 with an atom of element j (mass M_2), the energy of the recoiled atom $E_2(x_i)$ is the kinematic factor K_{ERDA}:

$$E_2(x_i) = K_{ERDA} E_0(x_i) = \frac{4M_1 M_2 \cos^2\beta}{(M_1 + M_2)^2} E_0(x_i) \tag{70}$$

The recoiled atoms lose energy as they travel through the sample, and exit with energy $E'_2(x_i)$ given by Eq. (71):

$$E_2^{'}(x_i) = E_2(x_i) - \int_{x_i}^{d} \frac{1}{\cos\beta}\left(\frac{dE_2(x)}{dx}\right)_{out} dx \tag{71}$$

Where d is the total sample thickness and $\left(\frac{dE_2(x)}{dx}\right)_{out}$ is the stopping power of the recoiled ion on the way out from the target. A stopping foil is placed in front of the detector which has a thickness x_{foil}, chosen to just stop the incident ^{12}C ion beam at its primary energy E_0. Thus, the energy of the recoiled hydrogen atoms measured by the charged particle detector $E'_2(x_i)_{det}$ is given by Eq. (72):

$$E_2'(x_i)_{det} = E_2'(x_i) - \int_0^{x_{foil}} S_{foil}(E)\, dE \tag{72}$$

Where $S(E)_{foil}$ is the stopping power of the recoiled ions in the stopper foil. The resulting idealised spectrum for a thin homogenous sample with constant hydrogen distribution is shown in Figure 29.

4.3.2. Experimental procedure

The measurements must be carried out in a vacuum chamber. The chamber should be light tight as the charged particle detector is sensitive to light (when bias is applied). In this experiment a collimated beam of 10 MeV $^{12}C^{+3}$ ions was used to recoil hydrogen atoms from a (2.9 ± 0.1) μm thick Mylar™ foil in transmission geometry (Figure 28a). The charged particle detector was placed at 45° forward angle with the measured ERDA spectrum shown in Figure 30. This figure shows the spectrum obtained (a) when no stopping foil is placed in front of the particle detector and (b) with a stopping foil. With no stopping foil, the spectrum contains overlapping spectra from recoiled hydrogen, oxygen and carbon ions together with scattered carbon ions. A 6 μm thick Mylar™ foil used as the stopping foil in front of the particle detector clearly removes all ions except hydrogen. It can be also seen that hydrogen peak is shifted towards the lower energies in spectrum due to the energy loss of hydrogen ions in the foil. In both cases, the spectra were collected to the same number of incident particles i.e. to the same collected charge (Q = 0.1 μC).

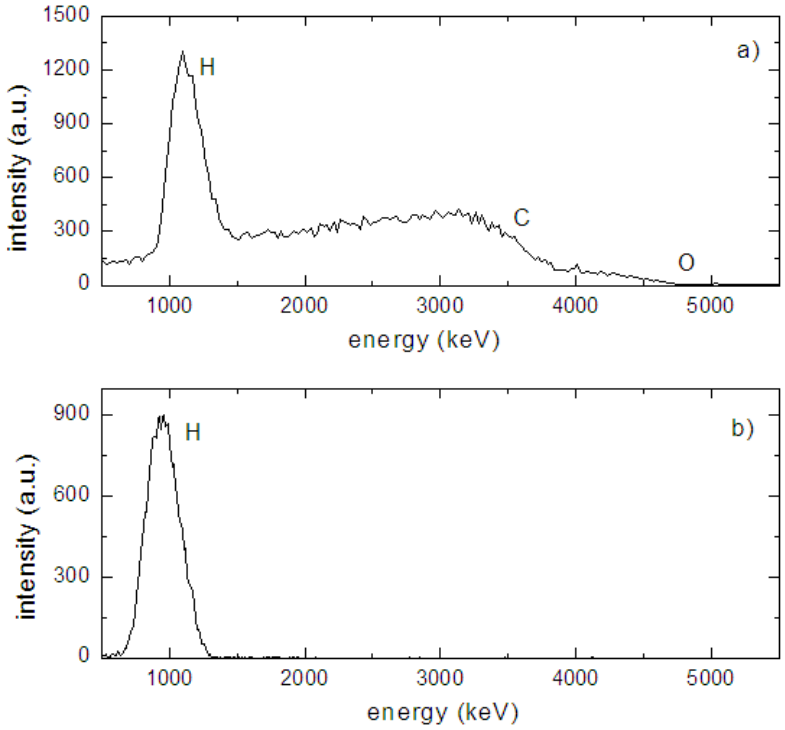

FIG. 30. Top: Spectrum of 10 MeV ^{12}C ions scattered from Mylar together with recoiled C, O and H ions from the target (without foil in front of the particle detector); Above: Spectrum of recoiled H atoms when 6 μm thick Mylar foil is placed in front of the particle detector.

The concentration of hydrogen atoms n_H in the Mylar™ foil can be calculated using Eqs. (67)-(69). If the sample is thick enough such that the energy loss of incident ions in the target cannot be neglected, as it is in this case, the calculation can proceed more easily by sub-dividing the thick sample into several thin slabs, and approximating the continually changing energy of the incident ion beam to be a constant in each of the slabs.

In this experiment, the thickness d of Mylar™ foil is ~28000×10^{15} at/cm^2. The total energy loss of 10 MeV C ions in this foil was calculated to be 2985 keV using SRIM [14]. The sample is divided into 10 slabs, each slab with thicknesses of $\Delta x = 2800\times10^{15}$ at/cm^2. The yield of hydrogen atoms from each slab with a thickness Δx can be calculated by using the cross-section at the mean energy in the slab. The differential cross-section $\frac{d\sigma(\bar{E}_0(x_i),45^\circ)}{d\Omega}$ used for calculation in each slab is tabulated in Table 23. The values have been calculated by the utility subroutines incorporated into SIMNRA [20].

The total yield of hydrogen ions is obtained by summing the yields from all 10 slabs. The hydrogen depth profile is coarsely represented by the concentrations calculated for each slab.

TABLE 23. CROSS-SECTIONS USED TO CALCULATE YIELD OF RECOILED HYDROGEN IONS IN EACH SUBLAYER IN THE MYLAR™ SAMPLE

x_i (10^{15} at/cm^2)	$E_0(x_i)$ (keV)	ΔE (keV)	$\overline{E}$ (keV)	$\frac{d\sigma}{d\Omega}(\overline{E}, 45^\circ)$ (mb/sr)
0	10000	283	9859	904
2800	9719	286	9574	958
5600	9431	288	9287	1018
8400	9143	291	8998	1085
11200	8852	294	8705	1159
14000	8558	296	8410	1242
16800	8262	299	8112	1335
19600	7963	302	7807	1441
22400	7661	304	7509	1557
25200	7357	307	7204	1692

As we wish to obtain a bulk-averaged hydrogen concentration in the Mylar™ film, the experimentally obtained total hydrogen yield is taken from spectrum that is shown in Figure 30b. The yield Y is the area under the peak (22640 counts). The total collected charge was 0.1 μC which for q=+3 charge state, corresponds to 2.08×10^{11} incident carbon ions. The solid angle of the particle detector at 45° is Ω = (8.76 ± 0.26) msr. If the solid angle of the particle detector is not known, it can be determined from a forward scattering spectrum of protons from some other thin transmission foil of heavy element such as Au, Cu, Ni, etc. for which cross-sections are Rutherford.

The bulk-averaged atomic concentration of H atoms in Mylar™ sample is calculated using Eq. (68) which is:

$$n_H = \frac{Y}{Q\Omega \sum \frac{d\sigma}{d\Omega}(\overline{E_0}(x_i), \beta)\Delta x}$$

$$= \frac{22640}{2.08\times10^{11}\cdot 8.76\times10^{-3} sr \cdot 2800\times10^{15} at/cm^2 \cdot 12391\times10^{-27} cm^2} = 0.3579$$

This result is in excellent agreement with the atomic concentration of hydrogen in Mylar™ obtained from its well-known stoichiometry $C_{10}H_8O_4$:

$$n_H = \frac{8}{10+8+4} = 0.3636$$

4.3.3. Concluding remarks

ERDA spectroscopy is very efficient technique using small accumulated charges (0.1 μC), and due to high recoil cross-sections, high yields can be obtained. By using a simple stopping foil, the unwanted background due to scattering events can be eliminated and the sensitivity for hydrogen detection enhanced. Analytical codes such as SIMNRA [20], NDF [21] or RUMP [22] are useful programs that can simulate elastic scattering experiments in various geometries (including RBS and ERDA) and are routinely used to obtain concentrations as well as depth profiles of unknown elements in the sample from the experimental spectrum.

Radiation induced damage occurs in polymeric materials and numerous other hydrogen containing materials in which hydrogen is lost during the measurements. The hydrogen loss can be significant and depends on many parameters such as ion type, ion current or total collected ion dose on the sample. To minimise losses, it is recommended to keep beam currents low, to have a large solid angle for the charged particle detector, and to keep the measurement charge low, measuring only until sufficient statistics have been collected under the hydrogen peak.

4.3.4. Recommended equipment

- A particle detector positioned at forward angle with stopper foil;
- A preamplifier, bias supply, spectroscopy amplifier, ADC and MCA;
- Reliable charge integration;
- A thin target foil with well-known stoichiometry and hydrogen concentration;
- SRIM;
- An ion beam with mass >1. Helium (~2 MeV) or carbon beams are most commonly used.

4.3.5. Safety precautions

The proton beam can produce high yields of X rays from collimators and beam-defining apertures if high currents are used and large amounts of the proton beam are incident on these beam trajectory defining components. A radiation survey should be made prior to undertaking measurements and if necessary, use the appropriate shielding and working distance to minimise any potential exposure risks.

4.4. PROTON-INDUCED GAMMA RAY EMISSION ANALYSIS OF Na AND Al

When a beam of particles hits the sample surface layer, nuclear reactions are induced, and gamma radiation is emitted. In PIGE, the radiation is detected during irradiation (prompt gamma emission instead of activation). The PIGE method is used in similar way as the PIXE method. PIGE enables the detection of the light elements with good sensitivity. The use of different bombarding particles and energies offers varying sensitivity for different elements, which makes this technique trickier to use than the PIXE method. The common bombarding particles used in PIGE analyses are protons, deuterons and alpha-particles. In this experiment, protons are employed for detection of aluminium and sodium.

4.4.1. Theoretical background

The observed gamma ray yield (or interaction products in general) is directly dependent on the cross-section (which defines the probability of a specific type of interaction) and the density of atoms of the kind to be determined. For thick samples (sample thickness greater than the incident ion range) and provided that the product radiation is not significantly attenuated when passing through the rather thin layer to the detector, the observed yield may be expressed as:

$$Y_i = n\varepsilon f_{wi} \int_0^{E_o} \sigma_i(E) / S_m(E) dE \tag{73}$$

Where i is the measured nuclide, m the matrix, n the number of bombarding particles, ε the detection efficiency including the solid angle, E_p the incident ion energy, f_{wi} the weight fraction of nuclide i, S_m the stopping force (or stopping power) for the matrix, and $\sigma_i(E)$ the cross-section for the specific reaction. In addition, we assume that the nuclide to be measured is evenly spread through the matrix. Also, straggling effects are ignored and smooth cross-section curves without resonance structures are assumed.

The complicating factors are that accurate cross-section data are not always available (within the energy region from incident energy to zero) and that the major element composition of the sample is needed to calculate the stopping forces.

An advantage of the method is that the gamma ray peaks are generally well isolated, and the energy is high enough that absorption corrections are not needed. The high penetrability of the gamma rays also simplifies the experimental arrangements.

The available literature for absolute thick-target gamma ray yields (per solid angle in steradians, and microCoulombs of collected charge) have been collected [23]. In several studies, the atlas of appropriate gamma ray spectra for light elements is also provided.

Detailed prescriptions for light element analyses by particle-gamma reactions may be found in the IBA Handbook [23]. Additionally, several important factors (e.g. geometry, background and interferences as well as peak broadening effects) to be taken into account for accurate element analyses by the PIGE method are described in this reference and the reader should consult Refs [23, 24] for more in-depth discussion on the method details. In this experiment only analysis of aluminium and sodium is considered.

An advantage of PIGE is the high penetrability of gamma rays, thus diminishing matrix effects. The detector can be positioned immediately behind the sample, providing a maximum solid angle for improved sensitivity. The experimental setups are simple, and with external beams, the usability of the technique can be enhanced. As a rule, very small amounts of sample material are needed. Also, surface topography does not significantly influence the determinations. The technique is fast and non-destructive. Using PIGE in combination with other ion beam techniques, nearly all elements can be detected simultaneously. On the other hand, PIGE can be used only for the analysis of selected isotopes, and its sensitivity for many elements is only moderate. Because the optimal conditions, such as the bombarding particles and their energy, depend on the matrix and the isotope to be detected, no universal “best” conditions and physical parameter choices can be provided.

4.4.2. Use of standards

Concentrations of elements distributed homogeneously in thick samples can be obtained by comparison to standards. Many multi-element standards exist for the analysis of geological, biological, and medical samples [e.g., National Institute of Standards and Technology (NIST), Institute for Reference Materials and Measurements (IRMM), International Atomic Energy Agency (IAEA)]. In many cases proper standards can be prepared by mixing a known amount of the element to be determined into a matrix similar to the one being studied. For example, the determination of carbon, nitrogen, and oxygen can be carried out with organic compounds as standards. The known stoichiometry for C, N, and O of the compounds can be used directly. As a restriction, the selected organic compounds should not have very high concentrations of any single element (above about 40 wt%).

4.4.3. PIGE analysis of Na and Al

An experimental set-up consisting of a vacuum target chamber (alternatively an external beam set-up may be used) with appropriate charge integration possibility is shown in Figure 31.

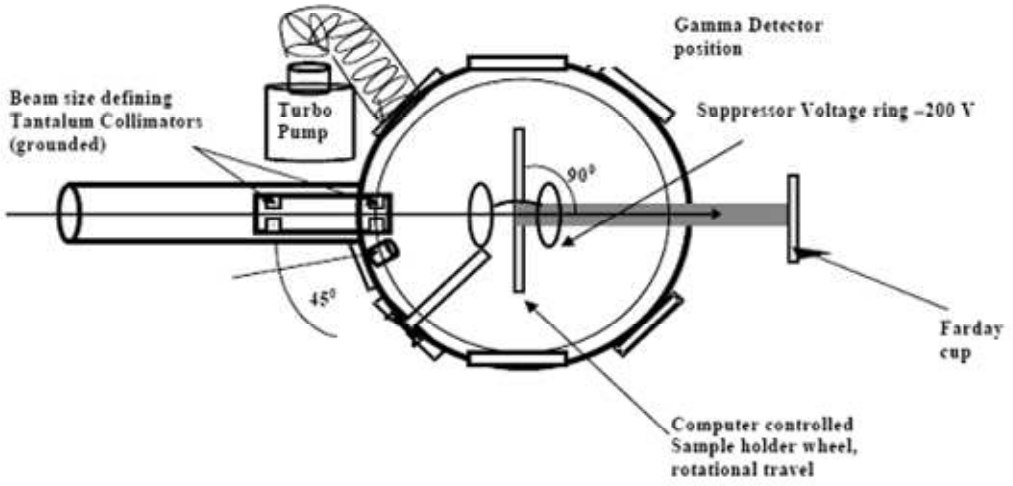

FIG. 31. Typical PIGE set-up used for in-vacuum measurements. In case of a thin sample the integrated charge can be collected from the Faraday cup. For thick samples the current integration is carried out directly from the sample.

The feasible gamma ray lines for elemental analyses of sodium and aluminium are discussed below.

Sodium has one stable isotope, ^{23}Na.
A good sensitivity for sodium analysis is obtained by detecting the 440 keV γ rays originating from the reaction ^{23}Na(p,p'γ)^{23}Na. The γ ray line at 1636 keV is somewhat Doppler-broadened.

Aluminium has one stable isotope, ^{27}Al.
Aluminium has several strong γ ray lines; at 844 keV and 1014 keV originating from the reaction ^{27}Al(p,p'γ)^{27}Al, at 1369 keV from the reaction ^{27}Al(p,αγ)^{24}Mg, and at 1779 keV originating from the reaction ^{27}Al(p,γ)^{28}Si (only at E_p<3 MeV). The 1369 keV line might have interference from sample magnesium. The 1779 keV line may contain interference from sample silicon and phosphorus. Also, the 844 keV and 1014 keV lines which are most suitable for aluminium analysis have interference from magnesium, ^{26}Mg(p,γ)^{27}Al, but fortunately the magnesium yields are rather low.

Typical gamma ray spectra obtained by 1.0 and 2.4 MeV proton bombardments of thick Na and Al samples are shown in Figures 32 and 33.

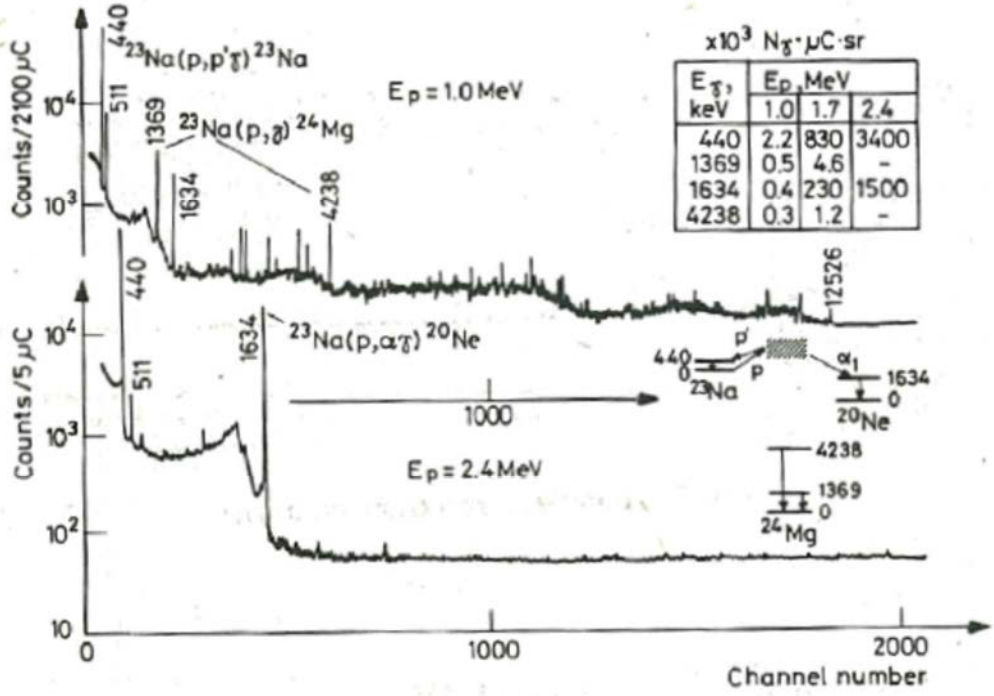

FIG. 32. Typical gamma ray spectra obtained from a thick sodium sample by 1.0 and 2.4 MeV protons. [25]

FIG. 33. Typical gamma ray spectra obtained from a thick aluminium sample by 1.0 and 2.4 MeV protons. [25]

4.4.4. Experimental procedure

(1) The standard sample and the "unknown" sample are bombarded with a proton beam of selected energy and the corresponding gamma ray spectra are recorded.
(2) The measurements should be normalised to correspond to the same collected charge.
(3) The calculated 440 keV and 844 keV peak area ratios (standard sample/"unknown" sample) and the concentrations stated in the standard sample certificate provide the Na and Al concentrations of the "unknown" sample. The deducted data can be collected in Table 24 to facilitate the analysis.
(4) For comparison determine the concentrations using the other gamma ray peaks (1636 keV for Na and 1014, 1369 and 1779 keV for Al). Be careful of possible interferences!
(5) Compare the obtained Na and Al concentration values with the certified values given in the "unknown" sample certificate.

TABLE 24. *DATA FOR Na AND Al CONCENTRATION DETERMINATION FROM AN "UNKNOWN" SAMPLE*

Sample	Collected charge [μC]	Na peak area [normalised by charge]	Al peak area [normalised by charge]	Au/As·Na-std.conc.	Au/As·Al-std.conc.
Standard (S)					
Unknown (U)					

4.4.5. Recommended equipment

- An energy calibrated gamma ray detector;
- Standard electronics for gamma ray spectroscopy;
- Peak fitting software;
- A 2-3 MeV proton beam, energy selected as available and most convenient;
- Two samples with known Na and Al concentrations. One is used as a standard and the other one as the "unknown" sample to be analysed. To check the accuracy of the obtained result, the concentration values should be compared with the values given in the "unknown" sample certificate.

4.4.6. Safety precautions

When energetic protons (above ~2 MeV) are used to bombard light elements (especially Li, Be, B) high neutron yields can occur as well as potentially high fluxes of high-energy gamma rays. The local accelerator related radiation safety rules and regulations must be followed to minimise the generation and exposure to any neutrons and high-energy gamma rays.

4.5. NUCLEAR REACTION ANALYSIS OF LIGHT ELEMENTS

Nuclear reactions induced by bombardment with energetic charged particles causing the emission of other energetic particles (particle-particle reactions) are used for elemental analysis. These methods are best applied to light elements, as nuclear reactions on light nuclei often have large Q-values and high cross-sections. The analysis method consists of the detection of charged particles produced by nuclear reactions during irradiation. In principle any reaction may be used, but with increasing projectile energy the number of outgoing channels becomes so large that the interpretation of the spectra from a complex sample becomes practically impossible. The most commonly used reactions are (p,α), (d,p) and (d,α). Alpha particle induced reactions have had limited use. Incident particle energies from 0.5 to 2 MeV are most useful for minimizing interference from reactions in heavy isotopes.

Bulk composition can be derived from particle-particle measurements assuming a homogeneous sample. The sensitivity is good for light elements, but for heavy elements, the Coulomb barrier reduces the cross-sections, thereby limiting the applications. Reaction cross-sections of 10 to 100 mb/sr are observed for proton and deuteron induced reactions in light isotopes (e.g. Li, Be, B). Sensitivities of the order of 10 μg/g or even less are possible with measuring times of the order of tens of minutes. Depth profiling of light elements is also feasible by this technique.

In this experiment, as an example, oxygen analysis via the $^{18}O(p,\alpha)^{15}N$ reaction is shown.

4.5.1. Theoretical background

The choice of optimum experimental parameters is an essential part of the design of an NRA measurement. Analysis using particle-particle reactions involves choices such as:

- choice of reaction;
- incident particle energy;
- detection angle.

Usually there is no analytical form of the nuclear cross-sections, so reliable experimental design and data analysis depends largely on the availability of measured cross-sections in the energy range and at angles of interest [19, 26].

The energy spectrum method is the main profiling technique used with particle-particle reactions. It is a relatively quick method since the necessary data are obtained during one irradiation with fixed incident particle energy. The product particle is usually different from the incident particle and higher in energy which has an important influence on the choice of experimental conditions and the performance achieved. Many variations of the method have been developed and the reader is asked to consult one of the references for more details.

NRA spectra are sometimes difficult to interpret as peaks of different particles (or the same particles with different energies) can overlap. Nuclear level diagrams showing nuclear structure and properties of nuclear levels can be found from the Nuclear Physics journal series [27].

Depth information is always obtained from the product particle spectrum if the depth exceeds that corresponding to the energy resolution. The energy interval to the next lower group in the spectrum sets the maximum depth that can be profiled. It should be noted that these

parameters are unique for each reaction. The maximum depth is usually limited to the order of 1 μm. At depths greater than approximately 100 nm, the effects of multiple scattering and energy loss straggling on both incident and product particles degrade the resolution.

4.5.2. Experimental procedure

Most particle-particle reaction measurements are made with very simple experimental arrangements. The basic NRA geometry is shown in Figure 34.

To avoid high count rate from elastically scattered primary particles, it is necessary to filter this large flux. The most common way to do this is to place a foil in front of the detector (absorber foil technique). The thickness of the foil should be equal to the range of the scattered particles so that these are absorbed while the higher energy reaction products pass through. Mylar or Kapton are common absorber foil materials. The major disadvantage of this absorber foil technique is that energy straggling takes place in the foil, resulting in poor energy resolution in the measured spectrum. As an example, the typical particle detector energy resolution of 10-15 keV may be degraded to 50-100 keV. This is not a problem if there is a sufficient energy difference between particle groups from different reactions or different target nuclides. Inhomogeneities in the absorber foil thickness affect the energy resolution.

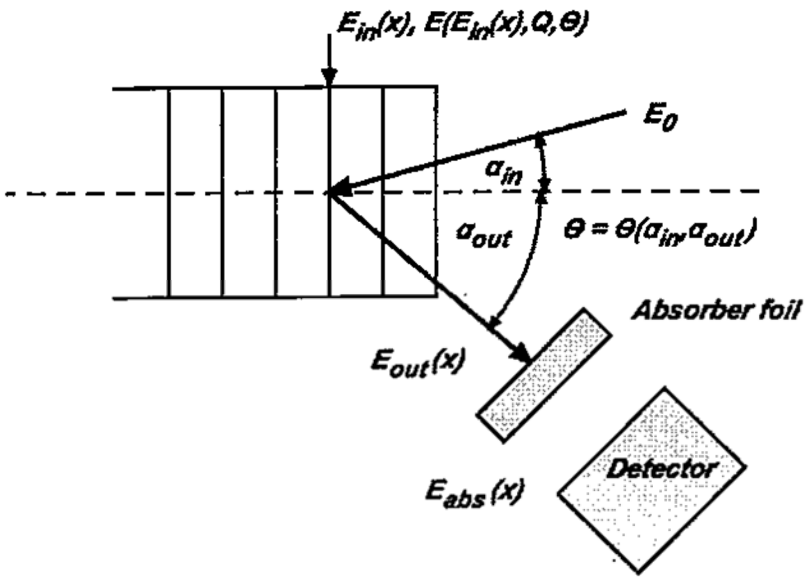

FIG. 34. Typical scattering geometry used in NRA experiments. E_o is the incident energy, E_{in} is the incident particle energy at reaction site, E_{out} is the reaction product energy after traversing out of the sample and E_{abs} is the particle energy after passing through the absorber foil. The conventional scattering angle is θ, which is the angle between the incident and exiting beams. The figure has been adopted from Ref. [23].

Practical information related to the detection of the light elements and a comprehensive list of proton and deuteron induced reactions feasible for light elements characterisation via particle-particle reactions is provided in Ref. [23].

The following brief list is only indicative and excludes reactions exhibiting simultaneous gamma ray and particle emission, as analyses based on detection of gamma rays are often more convenient than on detection of the charged particles.

TABLE 25. BRIEF LIST OF LIGHT ELEMENT NUCLEAR REACTION ANALYSIS

^{6}Li	the (d,α) reaction provides reasonable performance.
^{9}Be	the (p,α) reaction is useful for depth profiling.
^{11}B	the (p,α) reaction is useful for profiling and boron detection.
^{12}C	the (d,p) reaction is most used. It can be used for simultaneous C, N and O determinations in thin layers.
^{13}C	the (d,p) reaction can be used for carbon detection and C isotope ratio measurements.
^{14}N	the (d,p) and (d,α) reactions can be used.
^{15}N	the (p,α) reaction is useful.
^{16}O	the (d,p) reaction is most used for profiling purposes (simultaneous C, N and O analyses).
^{18}O	the (p,α) reaction utilizing narrow resonances is commonly used for depth profiling. The (d,p) and (d,α) reactions can also be used.
^{23}Na	the (p,α) reaction may be used for depth profiling.
^{28}Si	the (d,p) reaction can be used with reasonable sensitivity.
^{31}P	the (p,α) reaction gives the best sensitivity.
^{32}S	the (d,p) reaction has been used for sulphur determination and profiling.

4.5.3. Experiments and calculations

(1) A fixed proton energy between 500-700 keV is selected; these are the most commonly adopted energies.
(2) A detection angle θ of 165^{o} is selected and fixed.
(3) Calculate the alpha particle energy as a function of incident proton energy (E_p) using Eq. (74), the kinematic formula for a two-body nuclear reaction, from initial proton energy downwards.

$$E_{\alpha}^{1/2} = B \pm (B^2 + C)^{1/2}, \tag{74}$$

Where $B = \frac{(M_p M_\alpha E_p)^{1/2}}{(M_\alpha + M)} \cos\theta$ and $C = \frac{\{MQ + E_p(M - M_p)\}}{(M_O + M)}$. M is the product nucleus mass. The Q-value for the reaction is 3.9804 MeV.

(1) Test (using the sample to be analysed) the effects of different absorber foil thicknesses and find the absorber foil thickness sufficient to exclude the scattered incident particles.
(2) Compare the adopted Mylar thickness value with the calculated value obtained by the SRIM program [14].
(3) Estimate the cut-off energy (for the selected absorber) for the emitted alpha-particles (by SRIM program).
(4) Using this value, estimate the approximate depth from which information is still obtainable (taking into account the energy loss of the alpha-particles in the sample material itself). First, based on calculations using Eq. (74), estimate the validity of using constant alpha-particle energy for this approximation.

(5) Measure the sample and note the obtained spectrum shape. Discuss the specific features according to the following points.

Notes:

- The measured alpha-particle energy depends on the energy loss of the protons when reaching depth x (α_{in} = 0) and the energy loss of the emitted alpha-particles when traversing a distance x × sec α_{out} in the sample before reaching the detector. The alpha-particle energy thus specifies the depth. The highest energy corresponds to the nearest surface region.
- The number of alpha-particles with specific energy depends on the reaction cross-section at fixed proton energy. Since the ^{18}O concentration is constant, the shape of the spectrum should be closely related to the cross-section curve (Figure 35) (ignoring the effects of straggling and detector energy resolution).
- The easiest procedure for composition determination by NRA is to use a standard sample. This is feasible if the standard and the unknown sample are both bulk samples (measurements under same experimental conditions). Then the composition at the surface can be obtained by applying the surface-energy approximation.

4.5.4. Recommended equipment

The experimental arrangement required for particle-particle analysis is similar to that for RBS and is shown schematically in Figure 35.

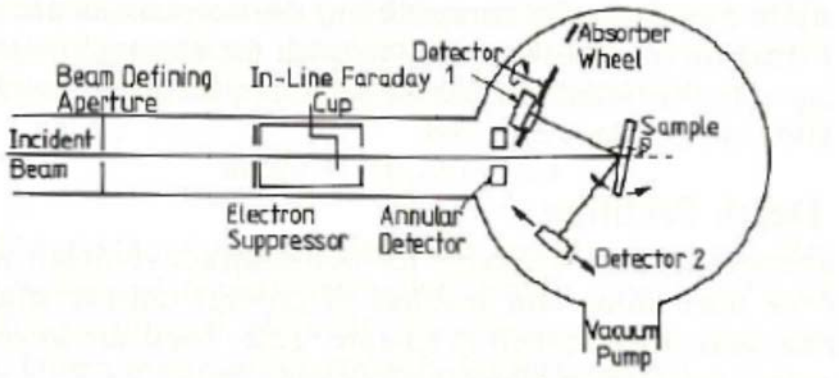

FIG. 35. Schematic layout of particle-particle analysis facility.

The experimental geometry consists of:

- A scattering chamber (light tight), with current integration;
- A particle detector with standard electronics for spectroscopy;
- Absorber foils of various thicknesses;
- A sample with constant oxygen concentration.

As an example of the use of particle-particle reactions for elemental analysis of light elements, the reaction $^{18}O(p,\alpha)^{15}N$ for oxygen determination is demonstrated. The straightforward method of using an absorber foil is employed. The relevant cross-sections as a function of proton energy are provided in Figure 36.

Several excellent presentations on the technique covering the principles and details are available. The reader should consult the list of references at the end of this experiment. In this experiment only the conventional use of RBS is treated and experimented via thin film stoichiometry and thickness determination.

4.6.1. Theoretical background

Only the main points related to the data analysis of this experiment are briefly discussed. Figure 37 shows the typical RBS geometry, the equations of ion transport and typical backscattering spectrum from a homogeneous single-element thick sample.

In the equations ε is the stopping cross-section factor and N is the atomic density of the sample material. H_o is the height (counts/channel) of the leading edge of an elemental peak corresponding to scattering from the sample surface. δE is the energy width per channel and ε_o is the surface-energy approximation of the stopping cross-section factor evaluated at the incident energy. $\sigma(E_o)$ is the scattering cross-section value at the incident energy. The other symbols are defined in the text below. Note that the equations above refer to a single-element sample.

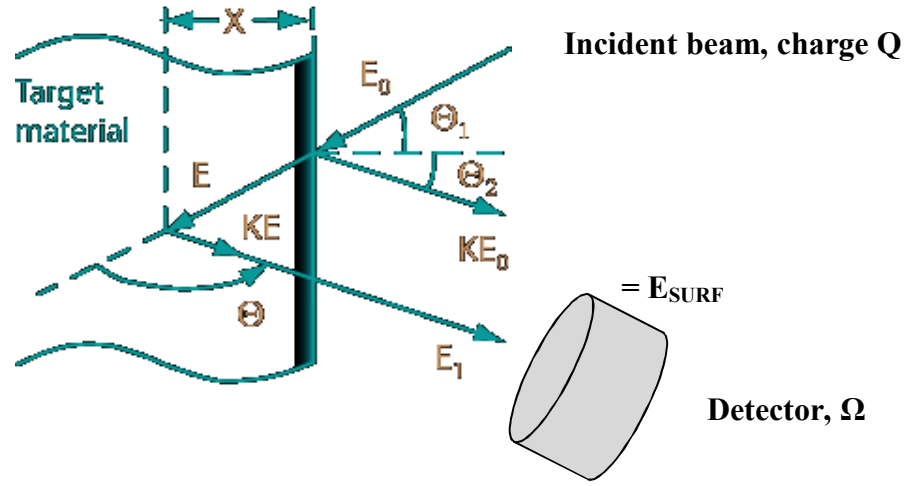

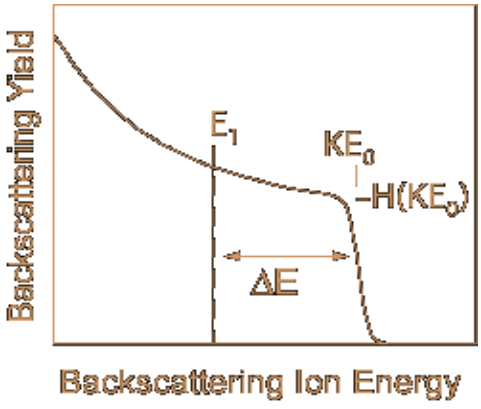

$$\Delta E = K \cdot E_o - E_1 = [\varepsilon]\, N\, x$$

$$[\varepsilon] = \frac{K}{\cos\Theta_1}\varepsilon_{in} + \frac{1}{\cos\Theta_2}\varepsilon_{out}$$

$$H(KE_o) \equiv H_o = \sigma(E_o)\Omega Q \frac{\delta E}{[\varepsilon_o]\cos\Theta_1}$$

FIG. 37. RBS geometry.

The kinematic factor is the ratio of the scattered ion energy E_1^i (from element i) to the initial ion energy E_0.

$$K_i = \frac{E_1^i}{E_0} \tag{75}$$

From the conservation of energy and momentum applied to the two-body collision between isolated particles of masses M_1 (incident particle) and M_2 (target) we obtain:

$$K = \left[\frac{\left(M_2^2 - M_1^2 \sin^2\theta\right)^{1/2} + M_1 \cos\theta}{M_1 + M_2}\right]^2 \tag{76}$$

Where θ is the scattering angle in the laboratory system. As the other parameters are fixed, M_2 can be determined from this relation and the target element can be identified.

The areal density $(Nt)_i$ in atoms per unit area for element i is obtained by using the following equation:

$$(Nt)_i = \frac{A_i \cos\theta_1}{Q\Omega\sigma_i(E,\theta)} \tag{77}$$

The use of this equation requires knowledge of the detector solid angle (Ω), integrated peak count A_i, the collected charge Q and the Rutherford scattering cross-section $\sigma_i(E,\theta)$. θ_1 is the angle of incidence of the bombarding particles with respect to the sample normal. The Rutherford scattering cross-sections are calculated directly by the employed simulation programs used for the spectrum analysis. In Eq. (77) N_i is the atomic density (atoms per unit volume) of element i and t is the film thickness.

The average stoichiometric ratio for the sample film (A_mB_n) can be now calculated by using Eq. (77):

$$\frac{n}{m} = \frac{N_B}{N_A} = \frac{A_B}{A_A}\frac{\sigma_A(E,\theta)}{\sigma_B(E,\theta)} \tag{78}$$

Note that the result depends only on the ratios of the peak area counts and of the cross-sections. It is not dependent on the collected charge or the detector solid angle which are clearly more difficult entities to be determined accurately.

Conversion of $(Nt)_i$ to thickness t requires information on the film density (ρ_{AB}). The atomic densities N_A^{AB} and N_B^{AB} can then be obtained from:

$$N_A^{AB} = \frac{m\rho_{AB}N_o}{M_{AB}} \quad \text{and} \quad N_B^{AB} = \frac{n\rho_{AB}N_o}{M_{AB}} \tag{79}$$

Where N_o is Avogadro's number and $M_{AB} = mM_A + nM_B$ is the molecular weight of the compound A_mB_n.

From Eq. (77) we obtain the film thickness:

$$t = \frac{(Nt)_A}{N_A^{AB}} = \frac{(Nt)_B}{N_B^{AB}} \tag{80}$$

The factors $(Nt)_i$ are obtained from Eq. (77) and the atomic densities N_i^{AB} from Eq. (79).

4.6.2. Experimental procedure

The employed set-up is similar to the one used for nuclear reaction analysis described in experiment 4.5. Typical arrangements are shown in Figures 35 and 38.

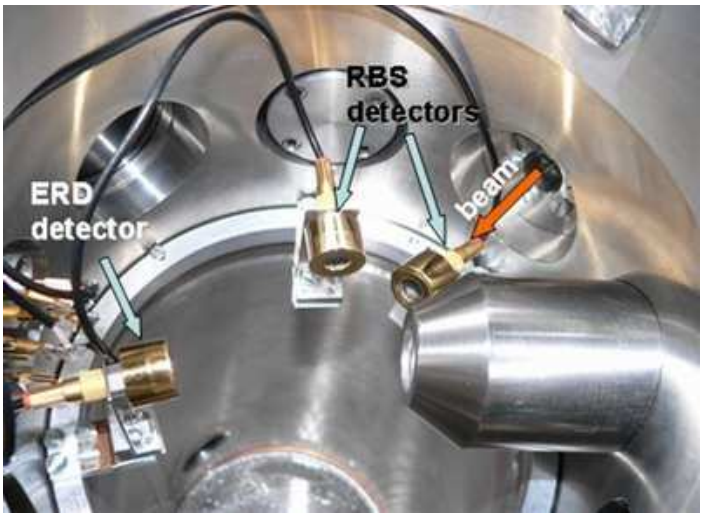

FIG. 38. Experimental set-ups for RBS measurements.

Two detection geometries are commonly used. They are referred to as the IBM and Cornell geometries. The incident beam is always horizontal and the sample surface is vertical. In the IBM geometry the detector is also placed in the same horizontal plane. In the Cornell geometry the detector is placed directly below the incident beam. For both arrangements, the charged particle detector is placed at a backward angle (e.g. 170^{o}). The most typical particle beam for conventional RBS measurements is a ^{4}He beam with energy of 1-2 MeV. A very basic energy spectrometry system for charged particle detection is employed, as shown in Figure 39. Thin film samples are prepared e.g. by the Atomic Layer Deposition (ALD) method, and are characterised by the RBS technique. In this experiment a two component thin film sample on a silicon backing is measured and analysed (here a Sn_xBi_y thin film grown on silicon substrate was chosen to demonstrate the spectrum analysis, but in fact any thin film sample available will do).

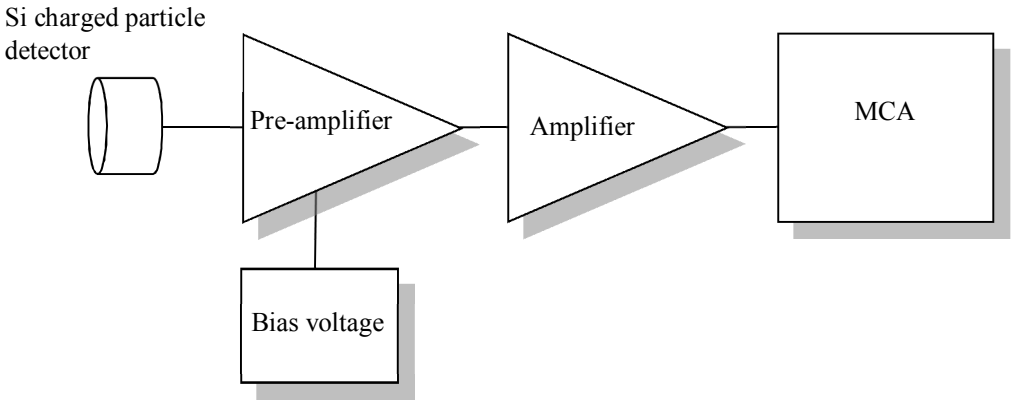

FIG. 39. Detection system used in conventional RBS measurements.

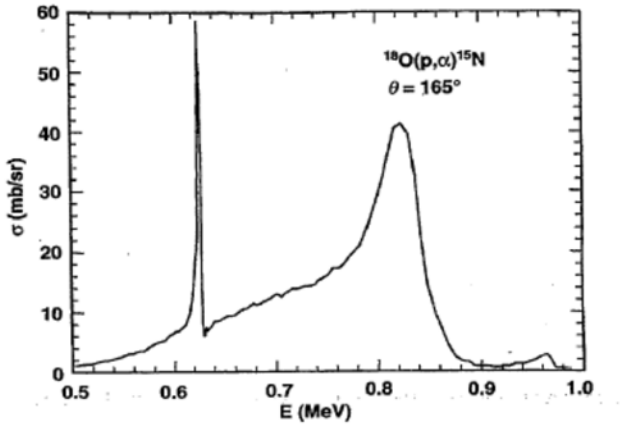

FIG. 36. Cross-sections of the $^{18}O(p,\alpha)^{15}N$ reaction at the indicated laboratory angle of 165°. Ref. [23].

4.5.5. Safety precautions

Even though charged particles are detected in this experiment it should be always kept in mind that energetic gamma rays and in some cases also neutrons are emitted during the sample bombardment. Specifically note that whenever deuterons are used as bombarding particles, a clear possibility for radiation hazard exists due to the high neutron yields. A radiation survey should be made prior to undertaking measurements and if necessary, use the appropriate shielding and working distance to minimise any potential exposure risks. In addition, whenever deuterons are used as bombarding particles and due to high neutron fields created, the surrounding metal structures can become activated increasing additional radiation risk. In such cases, continuous monitoring of neutron and gamma dose rate might need to be installed, and the entrance in the experimental room might be permitted only after decay of activation products.

4.6. RUTHERFORD BACKSCATTERING SPECTROMETRY OF HEAVY ELEMENT LAYERS ON A SILICON SUBSTRATE

Rutherford Backscattering Spectrometry (RBS) [28] is the most widely used ion beam technique. The technique is based on the determination of the number and energy distribution of particles backscattered from the sample atoms. The most common applications include the determination of sample stoichiometry, elemental areal density, and impurity depth profiling in thin films.

Presently many specific variations of RBS are used, such as:

- Heavy ion backscattering HIBS. This option provides improved mass and depth resolution;
- Utilisation of the ion channelling feature. This special feature is commonly used for the detection of displaced atoms in crystalline structures;
- Utilisation of non-Rutherford elastic scattering. This improves the sensitivity for several light element detection and profiling.

4.6.3. Energy calibration

The energy of the detected particles is converted to a charge pulse and after suitable amplification to a voltage pulse. The height of the analogue voltage pulse is converted further to the digital output of the ADC (channel number). The energy E of the detected particle is linearly proportional to the channel number ch of the MCA:

$$E = k_{ch} \times ch + E_0 \tag{81}$$

Where k_{ch} (energy/channel) and E_0 (zero offset) are the energy calibration coefficients. These parameters are needed for the evaluation of the spectra or for fitting a theoretical spectrum to the experimental one. In RBS analysis the energy of the particles scattered from known surface elements can be calculated. Therefore, one can use standard samples with known elements at the surface for energy calibration. From the position of the surface peaks (very thin films) or steps (thick samples) and the corresponding energy values, the calibration coefficients (k_{ch} and E_0) are then evaluated through linear regression.

4.6.4. Measurements

Accurate ^{4}He ion beam energy can be determined by employing nuclear resonance reactions (see another experiment in these series). An example of such a reaction is $^{24}Mg(\alpha,\gamma)^{28}Si$ and its three resonances at energies of 2435, 2866 and 3198 keV [23]. If the initial energy of the ion beam is already sufficiently accurately known this step can be omitted.

The conversion of the pulse height analyser channel number to backscattered ion energy can be carried out by bombarding pure elemental thin film targets (same bombarding energy, same geometry, and several elements should be measured to warrant wide calibrated energy range). Typical calibration samples could be: Ti/Si substrate, Ag/Si substrate, Au/Si substrate and so on.

To get the RBS spectrum of the thin film:

(1) Collect the RBS spectrum of the sample to be analysed.
(2) Record the collected charge used in the sample RBS measurement.

Note: In all measurements adjust the detector count rate to a reasonable level to exclude detection dead-time-corrections.

Sn-Bi thin film sample spectrum:

As a sample case a thin bi-elemental Sn-Bi alloy film grown on a Si substrate is characterised. The RBS spectrum obtained from the sample by 3 MeV alpha particles is shown in Figure 40. The experimental parameters in the measurements were as follows:

(1) detection angle 165^o (Cornell geometry);
(2) ion energy 3 MeV $He^{+;}$
(3) collected charge 37 nC;
(4) detection solid angle 43.48 msr;
(5) energy resolution 18 keV;
(6) detector energy calibration E_o = -85.3 keV and k = 8.188 keV/channel;
(7) area of experimental Si yield 19274 counts;
(8) area of experimental Sb yield 768 counts;
(9) area of experimental Bi yield 812 counts;
(10) area of simulated Si yield 19604 counts;

(11) area of simulated Sb yield 954 counts;
(12) area of simulated Bi yield 1047 counts.

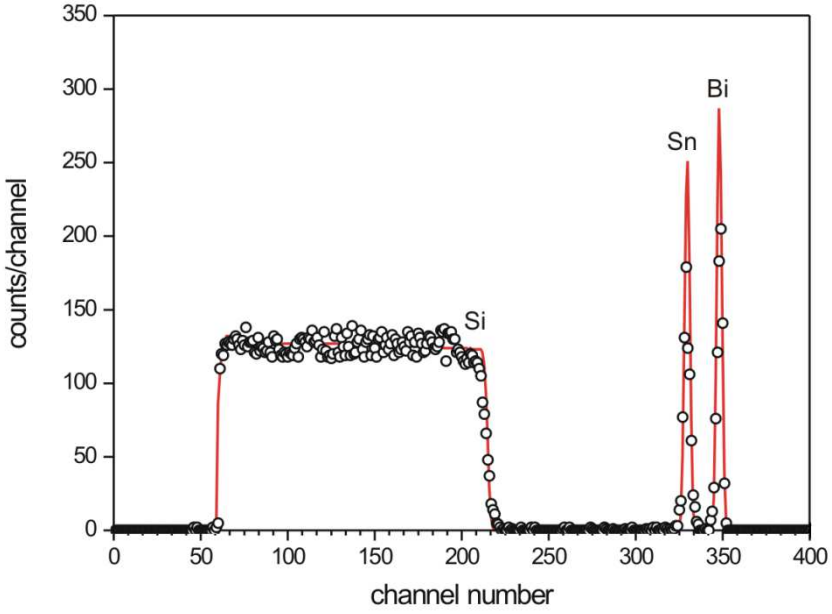

FIG. 40. RBS spectrum obtained of a thin film of Sn_xBi_y alloy grown on Si substrate. For experimental parameters see the text.

4.6.5. Data analysis

Using the guidelines and equations provided in the theoretical part of these instructions:
(1) Identify the sample elements by using Eqs. (75) and (76);
(2) Calculate the average stoichiometry of the film using Eq. (78);
(3) Calculate the sample film areal density by Eq. (77).

The corresponding simulated spectrum obtained by using the computer code RBX [29] is shown by the solid red line. The experimental parameters were used as input to the program. The simulation yields a stoichiometry of $Sn_{0.74}Bi_{0.26}$ and a film areal density of approximately 1.2×10^{17} atoms/cm^2.

Some other commonly utilised RBS computer codes besides RBX are SIMNRA [20], NDF [21] and RUMP [30].

4.6.6. Concluding remarks

The most common RBS computer codes are listed in Ref. [23] along with proper references and the code distribution modes. A comprehensive presentation of the various simulation programs can also be found in Ref. [23]. Finally, it should be noted that by taking advantage of the increased, non-Rutherford, cross-sections at high He ion energies, the sensitivity for the detection of light elements can be improved significantly. The procedures of utilising the enhanced cross-sections in analytical work (including utilisation of the cross-section resonances for light element depth profiling) may be found in Ref. [23] along with appropriate cross-section data.

4.6.7. Recommended equipment

- Scattering chamber (light tight), with current integration;
- Particle detector with standard electronics for spectroscopy;
- A thin film sample deposited on a light substrate (e.g. silicon).

4.6.8. Safety precautions

In case the sample contains significant concentrations of light elements, one should note the possibility for prompt gamma ray and neutron emission. Radiation level should be measured prior to the experiment, and constantly monitored throughout. If necessary, use the appropriate shielding and working distance to minimise any potential exposure risks.

5. ACCELERATOR NUCLEAR INSTRUMENTATION EXPERIMENTS

5.1. MEASUREMENT OF THE EFFICIENCY CURVE OF AN X RAY DETECTOR

Contrary to charged particle detectors where the detection efficiency is 100% and is not dependant on ion energy, the intrinsic detection efficiency for Si(Li) X ray detectors strongly depends on the X ray energy. The non-constant detection efficiency of a Si(Li) detector must be taken into consideration when making elemental analysis using PIXE. For low-energy X rays (1–3 keV), the intrinsic detection efficiency is very low and thus the sensitivity for PIXE measurements of Al, Si, P and Cl using their characteristic K_α X ray lines is low. This experiment will measure the intrinsic detection efficiency in the region 1–10 keV.

5.1.1. Theoretical background

A Si(Li) X ray detector can be geometrically modelled, as shown in Figure 41. The sensitive detection volume is a silicon crystal. A gold contact layer is deposited on the crystal and beneath this is an inactive silicon dead layer. The Si crystal is maintained at liquid nitrogen temperatures in a cryostat which has a thin Be window to allow the X rays to pass through. These four thicknesses are normally provided by the detector manufacturer in the detector's specifications. In addition, the presence of the ice layer at the surface of a Si(Li) detector should be also taken into account. This layer is formed due to condensation of the water molecules onto the Si crystal that is kept at the liquid nitrogen temperature and can be a few tens of μm thick after a few years of operation.

X rays incident on this system are attenuated by the Be window, ice layer, Au contact and Si dead layers. The transmitted X rays are then absorbed by the Si crystal, producing electron-hole pairs which generate an electrical pulse of amplitude proportional to the energy of the X ray.

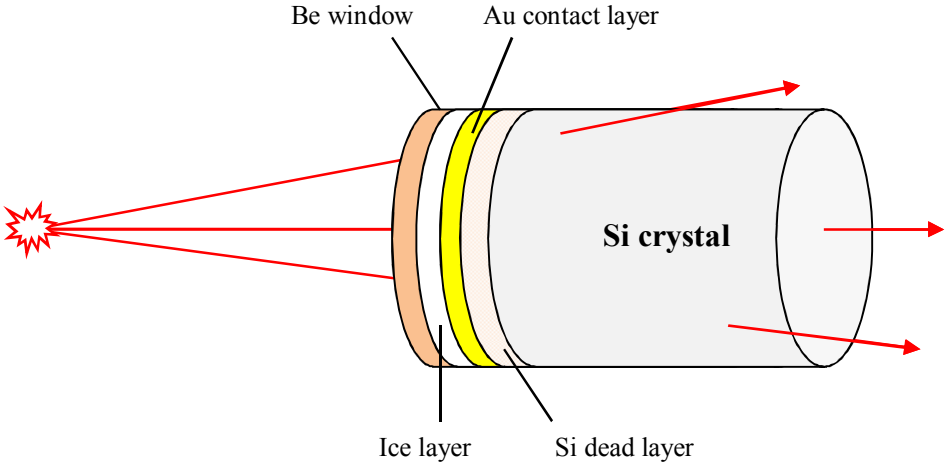

FIG. 41. Schematic model of a Si(Li) X ray detector.

Using this model, the detector efficiency $\varepsilon(E)$ at energy E can be described by Eq. (82):

$$\varepsilon(E) = T(E) \times A(E) \tag{82}$$

Where T(E) is the fraction of X rays transmitted through the Be window, ice layer, gold contact and Si dead layers, and A(E) is the fraction of X rays absorbed by the Si crystal.

$$T(E) = \exp\ [-\mu_{Be}x_{Be} - \mu_{ice}x_{ice} - \mu_{Au}x_{Au} - \mu_{Si}x_{Si}^{d}] \tag{83}$$

$$A(E) = 1 - \exp[-\mu_{Si}^{p}x_{Si}] \tag{84}$$

Where μ_{Be}, μ_{ice}, μ_{Au} and μ_{Si} are the total mass attenuation coefficients for X ray of energy E in the Be window, ice layer, Au contact and Si dead layer and x_{Be}, x_{ice}, x_{Au} and x_{Si}^{d} are the thicknesses of those materials. μ_{Si}^{p} is the photoelectric absorption coefficient at energy E and x_{Si} is the thickness of the active Si crystal. The absorption coefficients can be found in Ref. [31] or obtained from the XCOM program [32]. For our detector x_{Be} = 25 μm, x_{Au} = 10 nm, x_{ice} = 0 nm, x_{Si}^{d} = 0 nm and x_{Si} = 3 mm. The calculated detector efficiency using this data is shown in Figure 42.

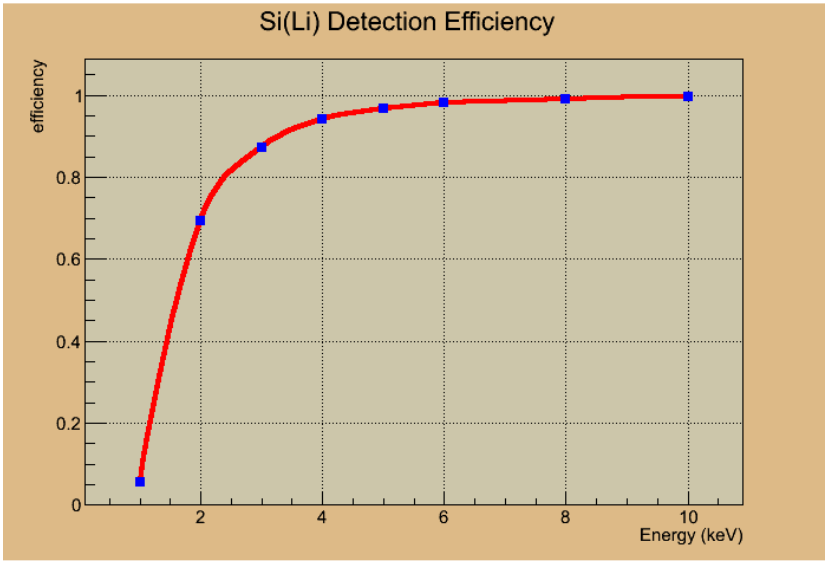

FIG. 42. Calculated intrinsic Si(Li) detector efficiency using XCOM Photo Cross-Sections.

In this low-energy region, *A(E)* = 1.0 (i.e. transmitted X rays are completely absorbed by the Si crystal). Here, the shape of the efficiency curve is completely determined by the attenuation of X rays through the Be window, ice layer, Au contact layer and Si dead layer.

Following the method proposed by Lennard and Phillips [33], the Si(Li) detector efficiency can be measured by detecting proton induced X rays from a set of thin calibration targets simultaneously with the elastically backscattered projectiles. The spectrum of elastically backscattered projectiles can be used to determine the target thickness. It is assumed that the X ray production cross-sections as well as non-Rutherford backscattering cross-sections are well-known for used elements. As the yield of backscattered particles and X rays are both proportional to the product of the number of incident protons and the target thickness, the ratio of X ray yield to proton backscattered yield is independent of these two quantities. Thus, the detector X ray efficiency can be determined without knowing them, as will now be described.

The experimental geometry is shown at Figure 43.

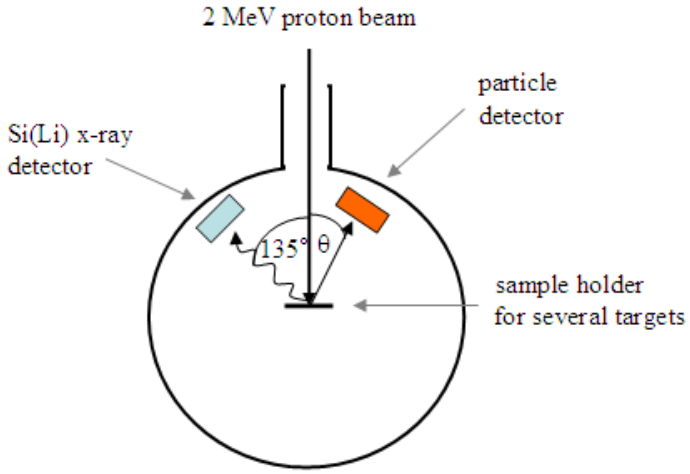

FIG. 43. Experimental setup for Si(Li) detector efficiency determination.

The target thickness N_x, in at/cm^2 is given by Eq. (85):

$$N_x = \frac{A_x}{Q\Omega_{RBS}\frac{d\sigma_x}{d\Omega}(E-\frac{\Delta E_x}{2},\theta)} \tag{85}$$

Where A_x is the area under the peak of element x in the backscattering spectra, Q is the number of incident particles, Ω_{RBS} is the detector solid angle, $\frac{d\sigma_x}{d\Omega}(E-\frac{\Delta E_x}{2},\theta)$ differential cross-section for backscattering of protons from element x, and ΔE_x is the energy loss of protons in the target. It should be checked if the backscattering cross-sections are Rutherford using the IBANDL web site [19] or SigmaCalc.

The number of counts under the K_α characteristic X ray line of an element x is the yield $Y_{xK\alpha}$ and can be calculated from Eq. (86):

$$Y_{xK\alpha} = \frac{\Omega_x}{4\pi} Q N_x \sigma_{IK} \omega_K f_{K\alpha} \varepsilon_x \tag{86}$$

Where Ω_x is the solid angle of X ray detector (in this case 3.3 msr), Q is the number of incident protons, N_x is the target thickness, in at/cm^2, σ_{IK} is the ionisation cross-section for the K^{th} shell of element x, ω_K is fluorescence yield for the K^{th} shell, $f_{K\alpha}$ is relative width of K_α X ray line and ε_x is the intrinsic detection efficiency for X ray line of element x.

It can be seen that the quantities Q and N_x are common in both equations. The intrinsic detection efficiency is calculated from Eq. (87):

$$\varepsilon_x = \frac{4\pi Y_{xK\alpha}}{Q\Omega_x N_x \sigma_{IK} \omega_K f_{K\alpha}} \tag{87}$$

5.1.2. Experimental procedure

The measurements must be carried out in a vacuum chamber. The chamber should be light tight as the charged particle detector is sensitive to light (when bias is applied). All spectra are collected to the same number of incident particles i.e. to the same collected charge (Q = 0.5 μC in this case). For this system $\Omega(\theta)$ is 7.6 ± 0.3 msr. The list of targets used in present experiment with calculated thicknesses from the backscattering spectra is given in Table 26.

TABLE 26. TARGETS USED FOR THE MEASUREMENTS WITH THICKNESSES CALCULATED USING RUTHERFORD BACKSCATTERING SPECTROMETRY

Z	element/compound	K_α X ray energy (keV)	thickness (10^{15} at/cm^2)
13	Al	1.49	788
14	SiO (Si)	1.74	664
15	GaP (P)	2.01	427
17	NaCl (Cl)	2.62	500
20	CaF_2 (Ca)	3.69	348
22	Ti	4.51	350
24	Cr	5.41	439
26	Fe	6.40	533
27	Co	6.93	460
28	Ni	7.47	390
31	GaP (Ga)	9.24	103
32	Ge	9.88	379

The spectrum of characteristic K X ray lines and backscattered protons from a thin Cr target is shown in Figure 44.

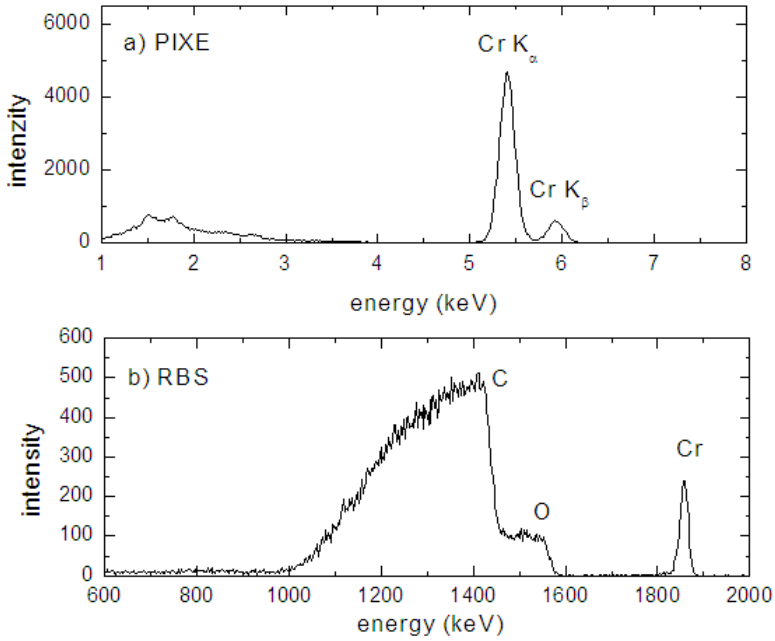

FIG. 44. a) Proton induced X ray spectrum of Cr K X ray lines, b) backscattered protons from the Cr target.

Fluorescence yields ω_K for the K^{th} shell are taken from [34], relative line widths $f_{K\alpha}$ from [35] and the ionisation cross-sections $\sigma_{IK\alpha}$ can be taken from [36]. In this experiment, reference ionisation cross-sections were calculated using the GUPIX subroutine GUCSA. Experimental yields of X ray lines are determined using the spectrum fitting routine in the program AXIL. The GUPIX program as well as any other program that can fit X ray peak shapes can be used as well. All parameters needed for calculation are given in Table 27 together with the calculated detector efficiency using Eq. (87).

TABLE 27. IONIZATION CROSS-SECTIONS FOR K SHELL σ_{IK}, FLUORESCENCE YIELDS ω_K, RELATIVE WIDTHS OF K_α X RAY LINE $F_{K\alpha}$ AND Si(Li) DETECTOR EFFICIENCY ε_X FOR ELEMENTS USED IN PRESENT WORK

Z	$E_{K\alpha}$ (keV)	σ_{IK} (b)	ω_K	$f_{K\alpha}$	ε_x
13	1.487	29401	0.039	0.986	0.33 ± 0.03
14	1.74	19483	0.05	0.976	0.51 ± 0.04
15	2.013	12910	0.064	0.960	0.64 ± 0.05
17	2.622	5923.9	0.099	0.922	0.68 ± 0.05
20	3.691	1916.4	0.169	0.887	0.85 ± 0.05
22	4.509	941.3	0.226	0.884	0.89 ± 0.05
24	5.412	476.2	0.288	0.882	0.99 ± 0.06
26	6.399	247.8	0.355	0.882	0.95 ± 0.06
27	6.925	179.9	0.388	0.881	1.01 ± 0.05
28	7.472	131.7	0.421	0.880	0.99 ± 0.05
31	9.243	52.7	0.517	0.873	1.02 ± 0.05
32	9.876	39.2	0.546	0.868	0.91 ± 0.05

The final result is plotted in Figure 45 with the detector efficiency values (symbols) calculated from experimental X ray spectra as a function of X ray energy, and the theoretical efficiency curve (Eqs. (82)-(84)) calculated using the subroutine GUCSA (full line) in the GUPIX software package. It is seen that the detector efficiency is significantly less than 100% in the low-energy region and is strongly dependent on the detector parameters. The uncertainty of calculated detector efficiency is between 6% for higher and 9% for lower energies due to higher uncertainty in the fluorescence yield at low energies (10–5% for $10 < Z < 20$ and 5–3% for $20 < Z < 30$).

This convenient technique can be successfully used for measurements of the intrinsic X ray detector efficiency if thin single element standards are available. If the Si(Li) detector efficiency is not known, then the above procedure will yield the absolute detection efficiency instead. The relationship between the absolute and intrinsic efficiencies is given by Eq. (88):

$$\varepsilon_{abs} = \frac{\Omega}{4\pi}\,\varepsilon_{int} \tag{88}$$

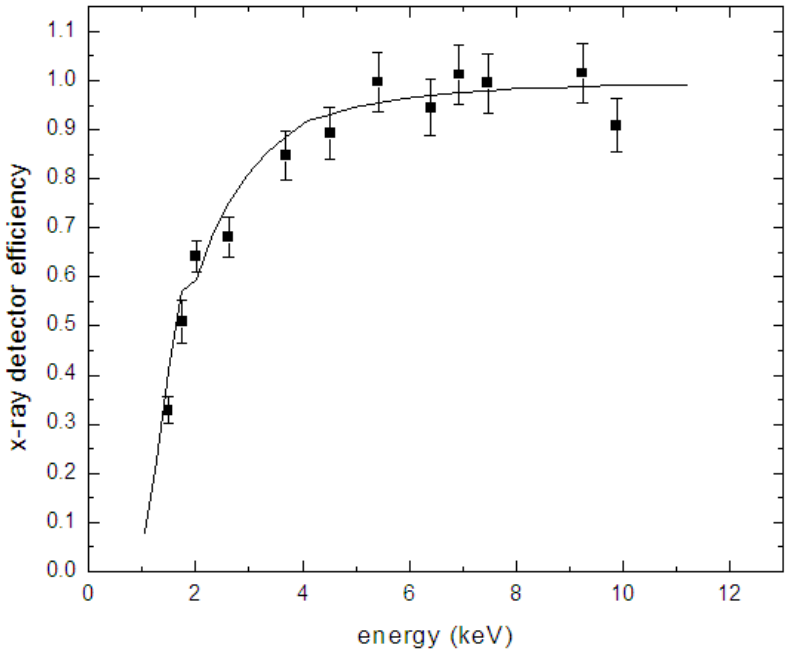

FIG. 45. Si(Li) detector efficiency as a function of the X ray energy (symbols) together with the theoretical efficiency calculated using Eqs. (66)-(68) and GUPIX subroutine GUCSA.

5.1.3. Recommended equipment

- Si(Li) detector;
- Si(Li) detector bias supply;
- spectroscopy amplifier (2 of);
- Charged particle detector;
- Charged particle detector bias supply;
- Analogue to digital converters (2 of) and multichannel analyser to record dual spectra;
- Set of thin calibration foils from $Z = 12$ to $Z = 35$;
- Graphical plotting software;
- X ray spectrum analysis software (e.g. AXIL, GUPIX or GUPIXWIN).

5.1.4. Safety precautions

The proton beam can produce high yields of X rays from collimators and beam-defining apertures if high currents are used and large amounts of the proton beam are incident on these beam trajectory defining components. A radiation survey should be made prior to undertaking measurements and if necessary, use the appropriate shielding and working distance to minimise any potential exposure risks.

5.2. ENERGY AND EFFICIENCY CALIBRATION OF A GAMMA RAY DETECTOR

In order to carry out multi-elemental PIGE analyses, a calibrated (for energy) gamma ray detector is required. For single (and in rare cases for determination of few elements simultaneously) element determinations, a detector with poorer energy resolution than a high purity germanium (HPGe) detector, such as NaI(Tl) or BGO, may be employed. The gamma ray detection system is typically calibrated for energy and efficiency using radioactive point sources for the low-energy gamma rays. In the first part of this experiment HPGe detector is calibrated for energy. This enables practical PIGE measurements of unknown samples for their light element composition. The actual PIGE measurements utilising multi-elemental standard samples for deducing the absolute concentrations are carried out in a separate example. The second part of this experiment deals with determination of the detector efficiency curve.

It should be noted that practical problems may be encountered if very high energy gamma rays are of interest as no common radioisotopes providing such gamma quanta are available. If required, the energy calibration can be easily performed by utilising nuclear reaction induced gamma rays of several light element targets, for example, $^{19}F(p,\alpha\gamma)^{16}O$, $E_\gamma = 6129$ keV. Note that the Doppler broadened gamma ray peaks cannot be used for energy calibration.

5.2.1. Theoretical background

Efficiency is often subdivided into two classes; *absolute and intrinsic*. Intrinsic efficiency does not include the solid angle subtended by the detector as an implicit factor. The two efficiencies are related as:

$$\varepsilon_{int} = \varepsilon_{abs}(4\pi/\Omega) \tag{89}$$

Where Ω is the solid angle of the detector seen from the radiation source position. In this experiment, it is assumed that the detector-source distance is significantly larger than the detector-crystal radius. In this case $\Omega \approx A/d^2$ (A is the detector frontal area and d is the detector-source distance). Determination of intrinsic efficiency is clearly more convenient than absolute efficiency determination. The intrinsic efficiency of a detector usually depends primarily on the detector material, radiation energy, and the physical thickness of the detector in the direction of the incident radiation.

For efficiency calibration one can use any source with known nuclide activity and gamma ray emission probability. Gamma radiation is emitted by excited nuclei in their transition to lower-lying nuclear levels. As an example, the decay scheme of ^{137}Cs is shown in Figure 46. From such decay schemes, the probabilities of various de-excitation transitions (branching ratios) and the number of gamma ray photons per disintegration may be found.

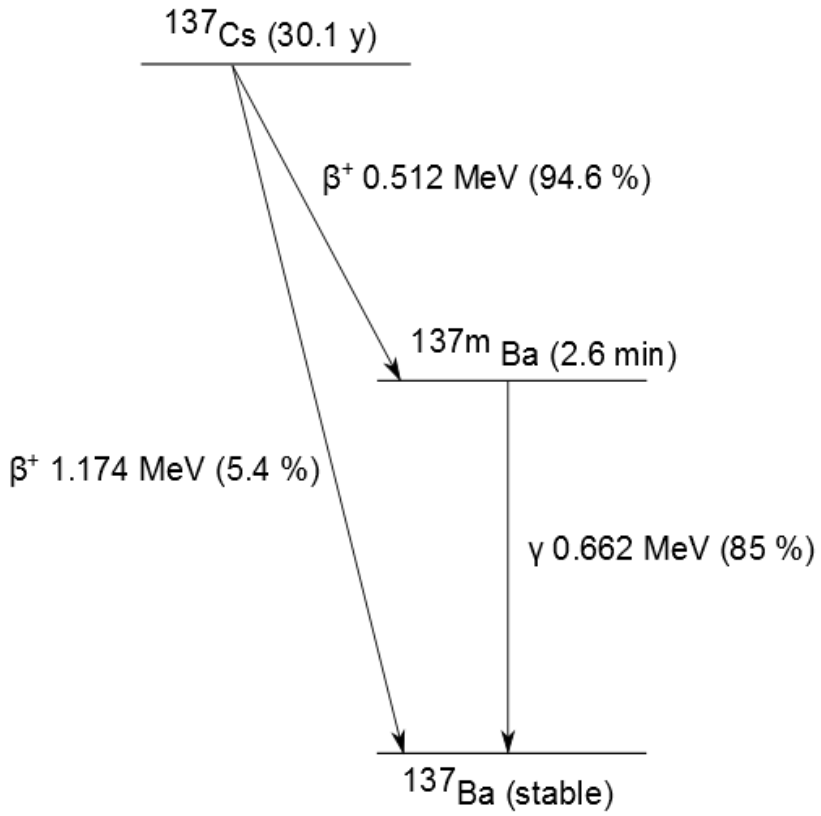

FIG. 46. Decay scheme of ^{137}Cs showing the corresponding branching ratio which should be taken into account in the efficiency determination.

Detector (intrinsic peak) efficiency is the ratio of the detected counts in a full energy peak to the number of the corresponding gamma rays emitted by the source:

$$\varepsilon(E_\gamma) = N_\gamma/N_s = N_\gamma/tpA_o \tag{90}$$

Where N_γ is the number of counts in the photo-peak, N_s is the number of photons emitted from the source. A_o is the activity of the source on the reference date, p is the branching ratio corresponding to energy E_γ and t is the real time of the successive measurements. For simplicity it is also assumed that the source emits radiation isotropically, and that no attenuation takes place between the source and the detector.

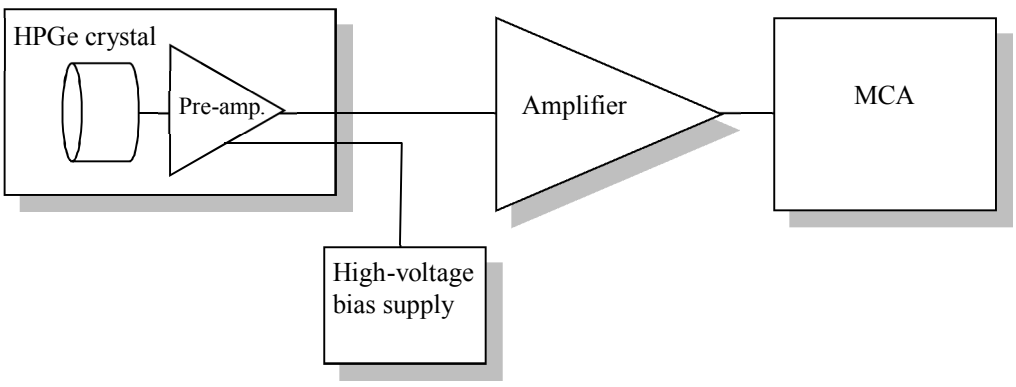

FIG. 47. Gamma ray energy spectrometry system.

5.2.2. Experimental procedure

Prior actual measurements some important points to be considered are:

- check the bias voltage polarity;
- select proper amplifier shaping time;
- adjust the amplifier gain;
- check if pole zero adjustment is necessary;
- check whether unipolar or bipolar pulse shape provides the best energy resolution;
- adjust proper gain for the amplification! Usually an energy region up-to about 6.5 MeV is sufficient (enables determination of fluorine via the reaction $^{19}F(p,\alpha\gamma)^{16}O$), if only low-energy gamma rays are to be detected, the gain can be increased;
- measure gamma ray spectra for all sources and insert the data in Table 28.

The measurement time is not important; it should only be sufficiently long to provide an accurate determination of the peak position.

TABLE 28. PEAK ENERGY VERSUS CHANNEL NUMBER

Source	Gamma ray line energy [keV]	Channel number

Feed the data of Table 28 into the MCA energy calibration program. For details consult the program manuals. Now instead of channel number, the x-axis shows the gamma ray energy.

- Check the source absolute activity at the specified date provided by the source manufacturer (source set specifications sheets);
- Calculate the source activity at the date of the efficiency curve determination;
- Measure each source for good statistics and record the measurement time accurately;
- Determine the peak areas of the gamma ray lines using the peak fitting program;
- Using the calculated source activity, determine the number of gamma rays emitted by the source during the measurement time. Insert the data in Table 29;
- Calculate the solid angle suspended by the detector in order to deduce the absolute efficiency curve;
- Calculate the ratio measured/emitted according to Eq. (90).

TABLE 29. DATA FOR EFFICIENCY CURVE DETERMINATION

γ-energy [keV]	Peak area [counts]	Measurement time [seconds]	Photons emitted by the source	$\varepsilon(E_\gamma)$

In common elemental analysis by the PIGE method, the efficiency of the detector is not required if elemental standard samples are employed. But there are times when efficiency is needed, e.g., when absolute thick target gamma ray yield determinations are of interest. In such cases the detector efficiency multiplied by the solid angle is used as entity and they need not be separated. Now, absorption effects of the low-energy gamma rays are also incorporated intrinsically in the efficiency curve. For such cases, place the sources at the position of the sample in the PIGE set-up.

The branching ratios and relative gamma transition intensities should be taken into account in the calculations (when extracting the number of photons emitted during the measurement) according to the procedure described in the fundamentals part of these instructions. Detector solid angle influence (4π steradians/solid angle of experiment in steradians) should be taken into account when calculating the number of photons emitted by the source.

- Plot the data of Table 29 as energy versus efficiency curve;
- Fit a higher order polynomial ($\varepsilon(E\gamma) = \sum a_i E_i$) to the obtained data.

A typical absolute efficiency curve is shown in Figure 48.

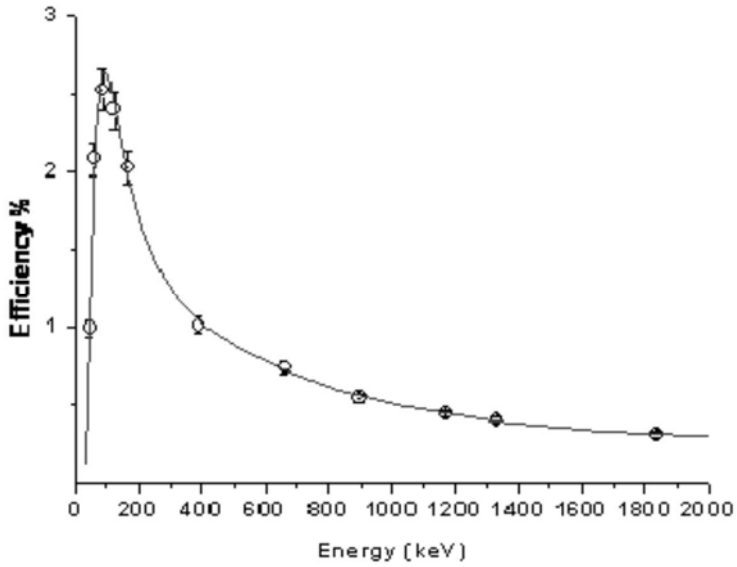

FIG. 48. A typical absolute efficiency curve for HPGe detector.

5.2.3. Concluding remarks

If required, the detection efficiency for the high energy gamma ray energies can be determined by using well-known gamma ray resonance transitions, e.g., the 992 keV resonance of the reaction $^{27}Al(p,\gamma)^{28}Si$ [37].

Despite extremely accurate and careful measurements, the data points in the efficiency curve may scatter somewhat. The curve should be smoothed out for practical use (by the polynomial fit). The data points also include the stated uncertainty of the reference source certified activity.

To improve the accuracy of the absolute efficiency curve, several source-detector distances (solid angles) should be utilised.

If high-activity sources are employed, proper corrections for detector dead time should be conducted when determining the efficiency curve.

The measurement geometry should be arranged so that detection of scattered gamma quanta is prevented.

5.2.4. Recommended equipment

- Detector (with integrated preamplifier);
- Detector bias supply (high voltage);
- Spectroscopy amplifier;
- Analogue to digital converter (ADC) and multichannel analyser (MCA);
- A set of gamma ray reference point sources, e.g. ^{57}Co, ^{137}Cs, ^{60}Co, ^{226}Ra, ^{152}Eu, ^{207}Bi and ^{208}Tl cover the energy range from 0.1 MeV to 3.0 MeV. Also ^{133}Ba, ^{110}Ag sources are commonly employed. The appropriate gamma ray energies and intensity ratios may be found in [23, 38];
- A peak fitting program such as those provided by the MCA vendors (e.g. Gamma Vision by Ortec or Genie-2000 Spectroscopy System by Canberra) is required.

5.2.5. Safety precautions

Even though the required source activities are low and sealed sources are used, the relevant safety regulations must be followed. With knowledge of the source activity and the type of radiation, together with a wise compromise between shielding, distance and exposure time, the risks can be minimised when working with the radioactive sources normally encountered in the laboratory environment.

5.3. ENERGY CALIBRATION OF A SILICON CHARGED-PARTICLE DETECTOR

Charged particle detectors must be calibrated for the detected particle energy in accordance with ion beam methods which are based on particle detection. Such techniques are discussed in the present series of experiments, namely, Rutherford backscattering spectrometry (RBS) and nuclear reaction analysis (NRA) with particle-particle reactions. The detector should be calibrated for the same type of particle as is involved in the actual application.

The most common particle detector used for ion beam analysis has traditionally been Si surface-barrier detectors, where a thin gold layer is used as an electrode. The newer detector type employs ion implantation to form accurately controlled junctions necessary for low reverse leakage currents and thin entrance windows (Passivated Implanted Planar Silicon, (PIPS)). The advantages of these over the surface-barrier detectors (SSB) are discussed in more detail later in these instructions. For light ions (protons and alpha-particles) the detector response is typically quite linear. The overall resolution is typically in the range of 8–15 keV at E_α = 5.486 MeV.

5.3.1. Detector choice

When selecting the proper detector type for each experiment, the vendors detector catalogues are of significant help. In the selection one should be careful to pick a detector with a sufficiently thick depletion region to stop the highest expected energy particles, or the energy of these particles will not be measurable. A nomogram shown in Figure 49 may be used to determine the depletion-layer thickness in a Si surface-barrier detector when protons, alpha particles or electrons are to be detected. Note that the depletion layer thickness, silicon resistivity and the required bias voltage are interconnected. As long as the depletion layer is thicker than the particle range, 100% detection efficiency is achieved.

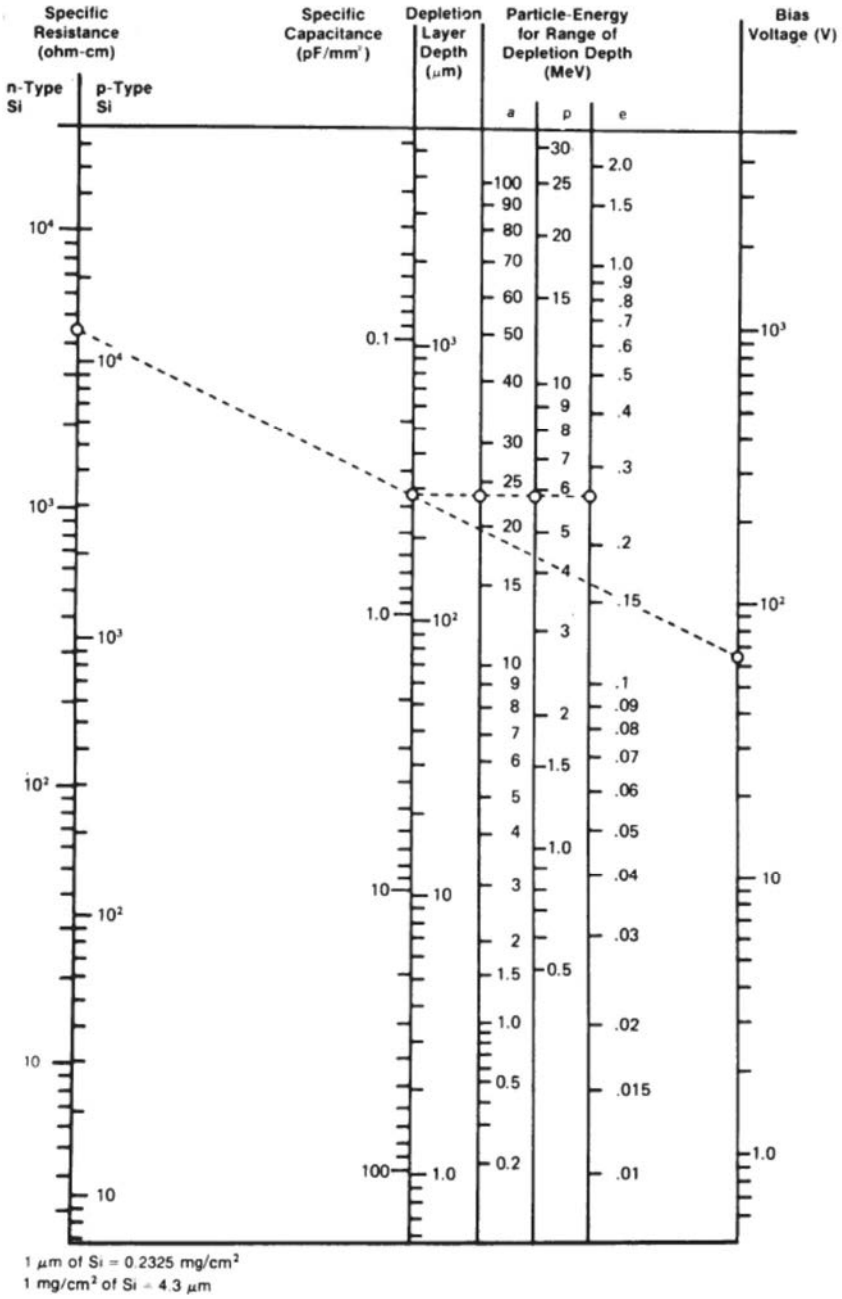

FIG. 49. Silicon surface-barrier detector nomogram showing the relationship between bias, depletion depth and resistivity.

The dotted line of Figure 49 shows that 13000 Ω-cm, n-type Si requires a bias voltage of 65 V to fully stop a 23 MeV alpha-particle, a 6 MeV proton or a 2.5 MeV electron.

In most applications, the PIPS detector can be used to replace silicon surface barrier (SSB) detectors and diffused junction (DJ) detectors, both of which are still made the same way they were made in 1960. The PIPS detector has a number of advantages over SDB and DJ types:

- All junction edges are buried - no epoxy edge sealant is needed or used;
- Contacts are ion-implanted to form precise, thin, abrupt junctions for good alpha resolution;
- Entrance window is stable and rugged — it can be cleaned readily and reliably;
- Leakage current is typically 1/8 to 1/100 of that of SSB and DJ detectors;
- Dead layer (window) thickness is less than that of comparable SDB or DJ detectors reducing the energy loss and straggling;
- Standard detectors can be annealed up to 100 °C and even higher for special models.

The PIPS detector has an entrance window that is substantially thinner than in conventional SSB detectors. A comparison is shown in Table 30.

TABLE 30. COMPARISON OF DETECTOR ENTRANCE WINDOW THICKNESS

Detector	Window Thickness (eq. Si)
PIPS	< 50 nm
SSB (Au Window)	≈ 80 nm
SSB (Al Window)	> 200 nm

In Figure 50 a simple energy spectrometry system setup for charged particle defections is shown.

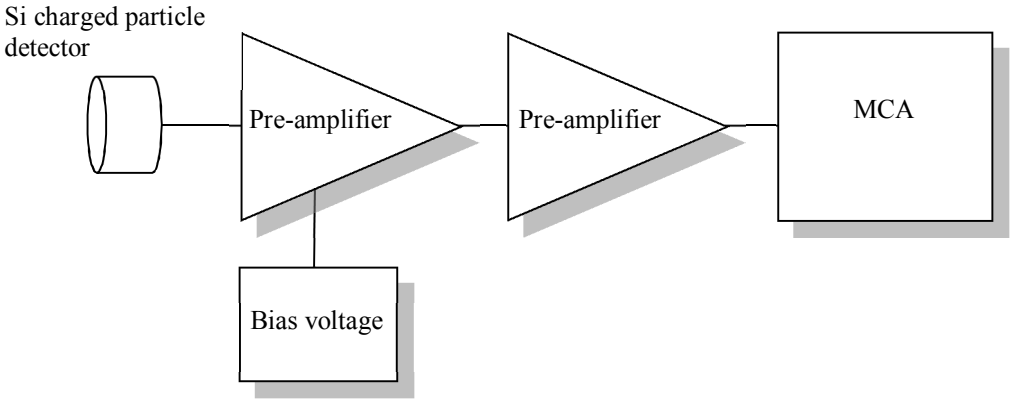

FIG. 50. Energy spectrometry system for charged particle measurements.

The most common radioactive source used for charged particle detector performance testing is the alpha emitting ^{241}Am source (see Figure 51). The main emitted alpha particle energies are 5.486 MeV (84.4%) and 5.443 MeV (13.6%). The energy resolution stated in the detector vendor specifications refers to the 5.486 MeV alpha particles emitted by this source. For accurate energy calibration of the energy loss of the alpha particles in the source itself, any

material between the source and the detector and in the detector dead layer should be corrected for. Alternatively, a ^{228}Th source can be employed.

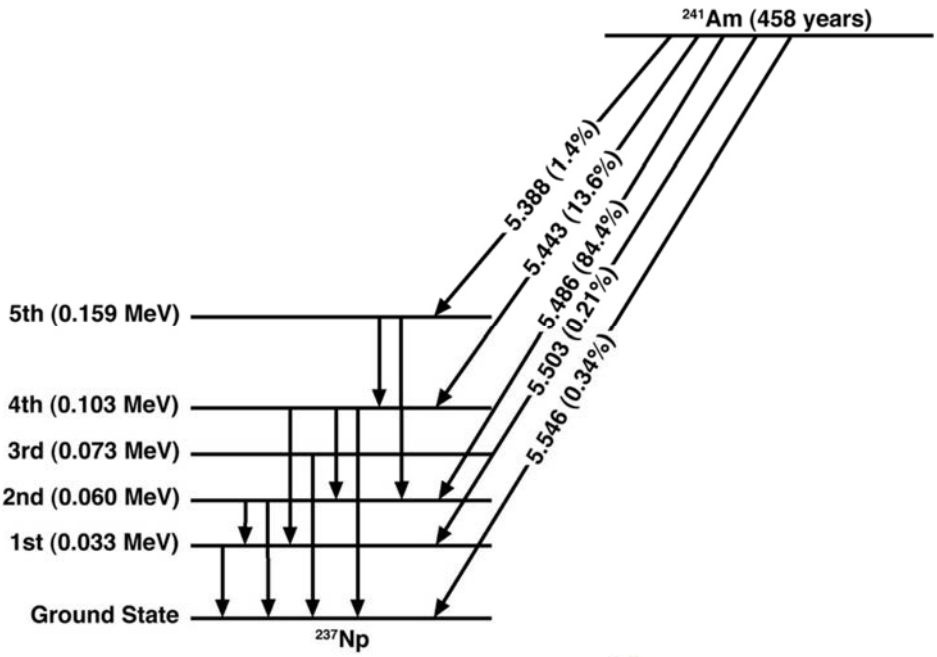

FIG. 51. Decay scheme for ^{241}Am.

The measurements must be carried out in a vacuum chamber. The chamber should be light tight as the detectors are sensitive to light (when bias is applied). A vacuum created by a fore-vacuum pump is sufficient.

5.3.2. Measurements

(1) Carefully place the alpha-source in the vacuum chamber and pump it until a constant pressure reading is achieved.
(2) Increase the detector bias voltage steadily to the specified value. The maximum operating voltage must be kept below the breakdown voltage. The detector specifications provide the maximum voltage rating. Additional protection can be provided by monitoring the leakage current during the experiments.
(3) Measure the energy spectrum for the alpha particles and use the MCA calibration program for channel to energy conversion. Plot the calibration line. A linear response should be noted. Note that an off-set is usually observed at zero.

NOTE: The energy calibration of a particle detector for heavy ions is not as straightforward as it is for light ions (such as alpha-particles in this experiment). This is due to the pulse height defect caused by energy loss due to nuclear collisions which also decreases the detector energy resolution. Energy is lost in the entrance window and the detector dead layer. For dense ionisation, recombination can also occur before the electrons and holes are fully separated.

5.3.3. Recommended equipment

The required components are:

- A detector;
- A preamplifier;
- Detector bias supply (with leakage current indication);
- Spectroscopy amplifier;
- Analogue to digital converter (ADC) and multichannel analyser (MCA).

Note the special microdot cable used in connecting the detector and the preamplifier.

5.3.4. Safety precautions

Unsealed alpha-sources often are employed, which must not be touched by hand and must be handled with extreme care. Work with unsealed radioactive sources must be conducted in a manner that reduces the exposure of users and the environment to an absolute minimum, and that involves the lowest possible risk of accidents of radiological significance. The local safety regulations must be followed.

5.4. ACCELERATOR ENERGY CALIBRATION USING THE $^{27}Al(p,\gamma)^{28}Si$ REACTION

5.4.1. Theoretical background

When the proton beam from the accelerator is being directed through an analysing magnet with well-defined and narrow exit slits, and transmitted to the centre of the scattering chamber through a system of beam-defining collimators, it travels along a well-defined trajectory. The relationship between the strength of the magnetic field and the radius of the curvature of the analysing magnet will define the transmitted proton energy which is given by Eq. (91):

$$BR = \frac{1}{cq}\sqrt{2m_p c^2 T + T^2} \tag{91}$$

Where B is the strength of the magnetic field, R is the radius of curvature of the beam trajectory through the magnet, q is the particle charge (for protons is 1), $m_p c^2$ is proton rest mass (938.283 MeV), and T is the proton kinetic energy (MeV). For analytic applications using a few MeV proton energies, the non-relativistic approximation is valid and so Eq. (91) becomes:

$$B = \frac{\sqrt{2m_p}}{eR}\sqrt{T} \tag{92}$$

By defining the constant K, the magnet constant, as:

$$K = \frac{\sqrt{2m_p}}{eR} \tag{93}$$

Eq. (92) becomes:

$$B = K\sqrt{T} \tag{94}$$

The magnet constant K, when determined experimentally, establishes a single-point relationship between the magnetic strength of the analyser magnet and the transmitted proton energy.

For energy calibrations, a comprehensive list of suitable reactions can be found in [23, 39]. The most commonly used reactions are based on:

- neutron threshold measurements such as ^{7}Li(p,n)^{7}Be at 1880.4 keV;
- narrow γ resonances such as ^{19}F(p,αγ)^{16}O at 872.1 keV or ^{27}Al(p,γ)^{28}Si at 991.9 keV;
- resonances in backscattering such as ^{16}O(α,α')^{16}O at 3036 keV.

In this experiment, the γ resonance in ^{27}Al(p,γ)^{28}Si at 991.9 keV is used for a single-point accelerator energy calibration by measuring the yield of 1778 keV γ ray by HPGe detector This γ ray energy of 1778 keV energy corresponds to the transition from the first excited to the ground state of ^{28}Si, and is emitted at the resonant proton energy of 991.9 keV.

5.4.2. Experimental instructions

The experimental geometry is shown in Figure 52 consisting of:

- A proton beam in the energy range from ~980–1010 keV;
- A scattering chamber with a sample holder for aluminium target;
- A HPGe detector placed at the 45°, 90° or 135° scattering angle and as close as practical to the target;
- Reliable charge collection from a target.

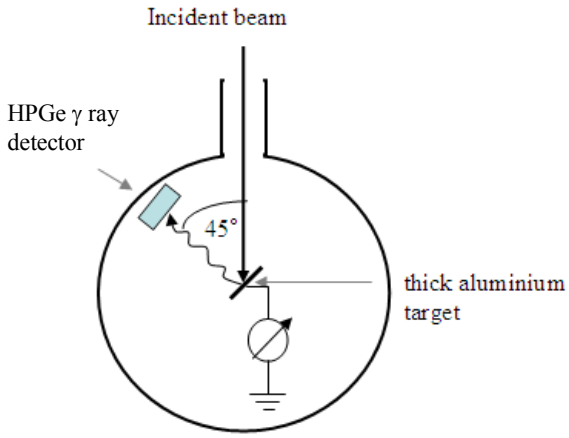

FIG. 52. Experimental setup for accelerator energy calibration using $^{27}Al(p,\gamma)^{28}Si$ reaction and detecting γ rays using HPGe detector.

A thick aluminium target has been used to produce γ rays. In practice it is difficult to use very thin targets because the yield of γ rays, which is proportional to the target thickness, is very small. Therefore it is more common to use a thick target in which the protons are either completely stopped or lose a large percentage of their energy.

The HPGe detector has been placed close to the target and inside the scattering chamber using a recessed access port in the target chamber. The γ ray spectrum for the one of the measurement points (analysing magnet magnetic field B = 0.27492 T) is shown in Figure 53. The total collected proton charge for each spectrum was 20 μC, with current during the measurement being ~20 nA.

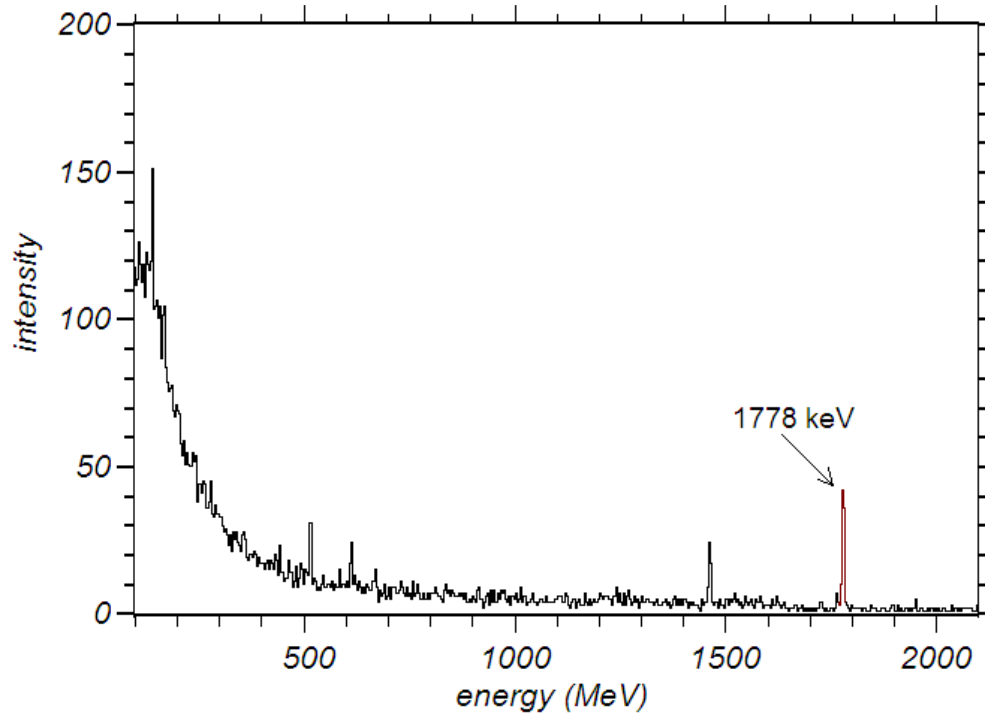

FIG. 53. γ ray spectrum for analysing magnet B=0.27492 T (above the 991.9 keV resonance).

The gamma ray yield, the area (number of counts) under the 1178 keV peak (including the background in this case), is normalised to the total number of protons incident on the target (integrated charge). The excitation function of the ^{27}Al(p,γ)^{28}Si reaction is determined by repeating the measurements at other accelerator energies near 991.9 keV resonance, and plotting the experimental data as shown in Figure 54.

The half-value height of the plateau corresponds to the resonance peak energy 991.9 keV. A fit of the experimental data with a Boltzmann function using the built-in function in the program ORIGIN 6.0, is shown with red line in Figure 54. The fit yielded a value of B = 0.27378 ± 0.00002 T for the half-height corresponding to the resonance energy E_0 = 991.9 ± 0.1 keV. From Eq. (94), the magnet constant K is calculated to be K = 0.27490 ± 0.00003 T/MeV$^{1/2}$ (n.b. the theoretical fitting function to use is the Error function, if available in the fitting software).

For a more accurate accelerator energy calibration, B versus $\sqrt{T}$ is measured at a number of widely-spaced energies using well-known reactions, and then a linear least-squares fit to the data is made to obtain Eq. (95):

$$B = \overline{K}\sqrt{T} + constant \qquad (95)$$

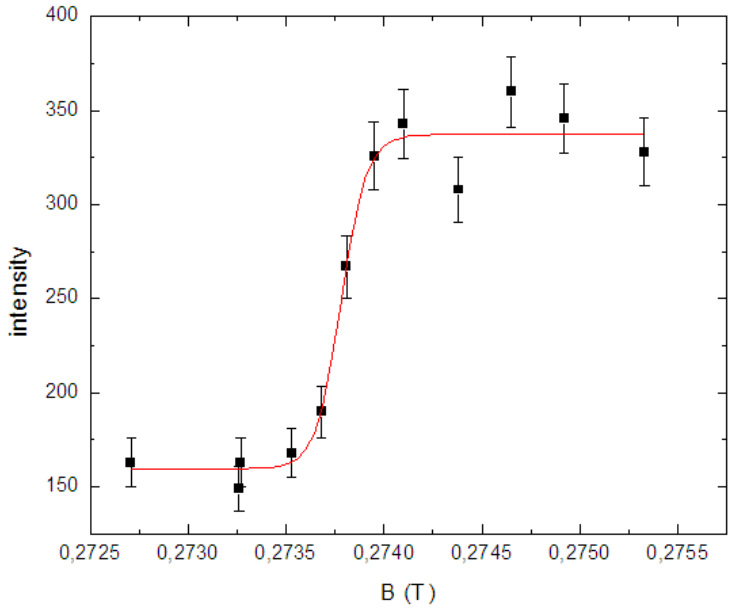

FIG. 54. Thick target γ ray yield for the excitation of $^{27}Al(p,\gamma)^{28}Si$ 991.9 keV resonance as a function of the magnetic field of the analysing magnet.

The front slope of the excitation yield contains information about the energy distribution of the proton beam. By convention, and assuming a Gaussian energy distribution, the energy half-height of the plateau is the energy of the beam (mean of Gaussian), while the region of energies from 10-90% represents the energy width of the beam (Gaussian FWHM).

From the fitted data in Figure 54, the 10% value (B = 0.27367 T) to 90% value (B = 0.273927 T) corresponds to 2 keV at ~1 MeV, or only 0.2 % of the beam energy. This beam width is primarily determined by the accelerator high-voltage instability and finite exit slit opening in the analysing magnet.

5.4.3. Recommended equipment

- Aluminium target;
- HPGe detector;
- Detector bias supply (high voltage);
- Spectroscopy amplifier;
- Analogue to digital converter (ADC) and multichannel analyser (MCA);
- Data fitting and plotting software (e.g. ORIGIN);
- A peak fitting program.

5.4.4. Safety precautions

Certain reactions used for calibration, such as $^{7}Li(p,n)^{7}Be$, produce neutrons in which the yields may be high, depending on the beam current. Additionally, the proton beam can produce high yields of X rays from collimators and beam-defining apertures if high currents are used and large amounts of the proton beam are incident on these beam trajectory defining components. A radiation survey should be made prior to undertaking measurements and if necessary, use the appropriate shielding and working distance to minimise any potential exposure risks.

REFERENCES

[1] INTERNATIONAL ATOMIC ENERGY AGENCY, Research Reactor Database, http://nucleus.iaea.org/RRDB/RR/ReactorSearch.aspx

[2] INTERNATIONAL ATOMIC ENERGY AGENCY, Accelerator Knowledge Portal: http://nucleus.iaea.org/sites/accelerators/Pages/default.aspx

[3] BÖCK, H., VILLA, M., Practical course on Reactor Physics and Reactor Kinetics, Atominstitut/Vienna University of Technology AIAU 26306 (2009).

[4] BÖCK, H., VILLA, M., Practical Course on Reactor Instrumentation. Atominstitut/Vienna University of Technology AIAU 24316, revised (2005).

[5] KHAN, R., KARIMZADEH, S., BÖCK, H., TRIGA fuel burn-up calculations and its confirmation, Nuclear Engineering and Design **240** (2010) 1043–1049.

[6] LAMARSH, J.R., BARATTA, A.J., Introduction to Nuclear Engineering, Prentice Hall, Inc., 3rd edition (2001).

[7] Joint Reactor Laboratory Course, KYOTO UNIVERSITY CRITICAL ASSEMBLY (KUCA), http://www.rri.kyoto-u.ac.jp/CAD/english/training.htm

[8] CANTEACH library, http://canteach.candu.org/

[9] KNOLL, G.F., Radiation Detection and Measurement, John Wiley & Sons Inc., 4th edition (2010).

[10] DUDERSTADT, J.J., HAMILTON, L.J., Nuclear Reactor Analysis, John Wiley & Sons Inc., New York, (1976).

[11] Nuclear Power Fundamentals, Integrated publishing, the most informative site on the internet, http://www.tpub.com/content/doe/h1019v2/css/h1019v2_104.htm

[12] BETHE, H.A., Bremsformel für Elektronen relativistischer Geschwindigkeit, Z. Phys. **76** (1932) 293 (in German).

[13] BLOCH, F., Bremsvermögen von Atomen mit mehreren Elektronen, Z. Phys. **81** (1933) 363 (in German).

[14] Stopping Range of Ions in Matter (SRIM) website, http://www.srim.org/

[15] BOHR, N., DAN, K., The Penetration of Atomic Particles through Matter, Vidensk. Selsk. Mat.-Fys.Medd. **18** (1948) 8.

[16] LIVINGSTON, M.S., BETHE, H.A., Nuclear Physics. C. Nuclear Dynamics, Experimental, Rev. Mod. Phys. **9** (3) (1937) 245.

[17] BERTI, M., et al, $^{12}C(\alpha,\alpha)^{12}C$ Resonant Elastic Scattering at 5.7 MeV as a Tool for Carbon Quantification in Silicon-based Heterostructures, Nucl. Instr. Meth. **B143** (1998) 357.

[18] MIYAGAWA, Y., et al, Oxygen depth profiling in $TiOxSiO_2$ prepared by sol-gel method using $^{16}O(\alpha, \alpha)^{16}O$ resonant backscattering, Nucl. Instr. Meth. **B136-138** (1998) 557.

[19] Ion Beam Analysis Nuclear Data Library (IBANDL) website, https://www-nds.iaea.org/exfor/ibandl.htm

[20] MAYER, M., SIMNRA, User's Guide, Technical Report IPP 9/113, Max-Planck Institut für Plasmaphysik, Garching, Germany (1997), http://home.rzg.mpg.de/~mam/

[21] Ion Beam Analysis DataFurnace website, http://www.surrey.ac.uk/ati/ibc/research/ion_beam_analysis/ndf.htm

[22] Rutherford Universal Manipulation Program (RUMP) website, http://www.genplot.com/RUMP/index.htm
[23] MATERIALS RESEARCH SOCIETY, Handbook of Modern Ion Beam Materials Analysis, 2nd Edition. Editors WANG Y., NASTASI M., Materials Research Society (2009).
[24] BIRD, J.R., WILLIAMS, J.S., Ion Beams for Materials Analysis, Academic Press (1989).
[25] ANTITILA, A., HÄNNINEN, R., RÄISÄNEN, J., Proton-induced thick-target γ ray yields for the elemental analysis of the Z=3-9, 11-21 elements, J. Radioanal. Chem. **62** (1981) 293.
[26] National Nuclear Data Centre, Brookhaven National Laboratory, http://www.nndc.bnl.gov
[27] Nuclear Data Evaluation Project, Triangle Universities Nuclear Laboratory, http://www.tunl.duke.edu/nucldata
[28] CHU, W.K., MAYER, J.W., NICOLET, M.A., Backscattering Spectrometry, Academic Press, New York (1978).
[29] KÓTAI, E., Computer methods for analysis and simulation of RBS and ERDA spectra, Nucl. Instr. Meth. **B85** (1994) 588.
[30] GENPLOT website, www.genplot.com
[31] THIN, T.P, LEROUX J., New basic empirical expression for computing tables of X ray mass attenuation coefficients, X ray Spectrometry **8** (1979) 85.
[32] BERGER, M.J., HUBBELL, J.H., National Bureau of Standards Report NBSIR. 87-3597 (1987), http://www.nist.gov/physlab/data/xcom/index.cfm
[33] LENNARD, W.N., PHILLIPS, D., Absolute measurement of the photopeak efficiency for a Si(Li) detector: 0.52-8.04 keV, Nucl. Instr. Meth. **166** (1979) 521.
[34] KRAUSE, M.O., Atomic radiative and radiationless yields for K and L shells, J. Phys. Chem. Ref. Data **8** (1979) 307.
[35] SCOFIELD, J.H., Exchange Corrections of K X ray Emission Rates, Phys. Rev. **A9** (1974) 1041.
[36] PAUL, H., MUHR J., Review of experimental cross-sections for K-shell ionization by light ions, Phys. Reports **135** (1986) 47.
[37] ANTTILA, A., KEINONEN, J., HAUTALA, M., FORSBLOM, I., Use of the ^{27}Al(p,g) ^{28}Si, E_p = 992 keV resonance as a gamma ray intensity standard, Nucl. Instr. Meth. **147** (1977) 501.FIRESTONE, R.B., SHIRLEY, V.S., BAGLIN, C.M., CHU, S.Y.F, ZIPKIN, J., Table of Isotopes, John Wiley & Sons, Inc. (1996).
[38] FIRESTONE, R.B., SHIRLEY, V.S., BAGLIN, C.M., CHU, S.Y.F, ZIPKIN, J., Table of Isotopes, John Wiley & Sons, Inc. (1996).
[39] MARION, J.B., Accelerator Calibration Energies, Reviews of Modern Physics **38** (1966) 323.

ABBREVIATIONS

ADC	Analogue to Digital Converter
ALD	Atomic Layer Deposition
CICH	Central Irradiation Channel
CIC	Compensated Ionization Chamber
CSC	Control System Computer
CR	Control Rod
DAC	Data Acquisition Computer
DJ	Diffused junction
ERDA	Elastic Recoil Detection Analysis
FC	Fission Chamber
FE	Fuel Elements
FWHM	Full Width Half Maximum
HIBS	Heavy Ion Backscattering
HPGe	High Purity Germanium
IRMM	Institute for Reference Materials and Measurements
I&C	Instrumentation and Control
MTR	Material Testing Reactor
MCA	Multi-channel Analyser
NIST	National Institute of Standards and Technology
NRA	Nuclear Reaction Analysis
PIXE	Particle Induced X ray Emission
PIPS	Passivated Implanted Planar Silicon
PIGE	Proton Induced Gamma ray Emission
RR	Research Reactor
RBS	Rutherford Backscattering Spectroscopy
SPND	Self-Powered Neutron Detector
SDB	Silicon direct bonding
SSB	Silicon surface barrier
TRIGA	Training, Research, Isotope, General Atomic
UIC	Uncompensated Ionization Chamber

CONTRIBUTORS TO DRAFTING AND REVIEW

Böck, H.	Atominstitut, Vienna University of Technology, Vienna, Austria
Bogdanović Radović, I.	Laboratory for Ion Beam Interactions, Ruđer Bošković Institute Zagreb, Croatia
Khan, R.	Atominstitut, Vienna University of Technology, Vienna, Austria
Li, R.	International Atomic Energy Agency
Mulhauser, F.	International Atomic Energy Agency
Räisänen, J.	Department of Physics, University of Helsinki, Helsinki, Finland
Ridikas, D.	International Atomic Energy Agency
Simon, A.	International Atomic Energy Agency
Villa, M.	Atominstitut, Vienna University of Technology, Vienna, Austria
Vyshniauskas Gomez, J.	International Atomic Energy Agency

IAEA
International Atomic Energy Agency

No. 23

ORDERING LOCALLY

In the following countries, IAEA priced publications may be purchased from the sources listed below or from major local booksellers.

Orders for unpriced publications should be made directly to the IAEA. The contact details are given at the end of this list.

AUSTRALIA
DA Information Services
648 Whitehorse Road, Mitcham, VIC 3132, AUSTRALIA
Telephone: +61 3 9210 7777 • Fax: +61 3 9210 7788
Email: books@dadirect.com.au • Web site: http://www.dadirect.com.au

BELGIUM
Jean de Lannoy
Avenue du Roi 202, 1190 Brussels, BELGIUM
Telephone: +32 2 5384 308 • Fax: +32 2 5380 841
Email: jean.de.lannoy@euronet.be • Web site: http://www.jean-de-lannoy.be

CANADA
Renouf Publishing Co. Ltd.
5369 Canotek Road, Ottawa, ON K1J 9J3, CANADA
Telephone: +1 613 745 2665 • Fax: +1 643 745 7660
Email: order@renoufbooks.com • Web site: http://www.renoufbooks.com

Bernan Associates
4501 Forbes Blvd., Suite 200, Lanham, MD 20706-4391, USA
Telephone: +1 800 865 3457 • Fax: +1 800 865 3450
Email: orders@bernan.com • Web site: http://www.bernan.com

CZECH REPUBLIC
Suweco CZ, spol. S.r.o.
Klecakova 347, 180 21 Prague 9, CZECH REPUBLIC
Telephone: +420 242 459 202 • Fax: +420 242 459 203
Email: nakup@suweco.cz • Web site: http://www.suweco.cz

FINLAND
Akateeminen Kirjakauppa
PO Box 128 (Keskuskatu 1), 00101 Helsinki, FINLAND
Telephone: +358 9 121 41 • Fax: +358 9 121 4450
Email: akatilaus@akateeminen.com • Web site: http://www.akateeminen.com

FRANCE
Form-Edit
5 rue Janssen, PO Box 25, 75921 Paris CEDEX, FRANCE
Telephone: +33 1 42 01 49 49 • Fax: +33 1 42 01 90 90
Email: fabien.boucard@formedit.fr • Web site: http://www.formedit.fr

Lavoisier SAS
14 rue de Provigny, 94236 Cachan CEDEX, FRANCE
Telephone: +33 1 47 40 67 00 • Fax: +33 1 47 40 67 02
Email: livres@lavoisier.fr • Web site: http://www.lavoisier.fr

L'Appel du livre
99 rue de Charonne, 75011 Paris, FRANCE
Telephone: +33 1 43 07 50 80 • Fax: +33 1 43 07 50 80
Email: livres@appeldulivre.fr • Web site: http://www.appeldulivre.fr

GERMANY
Goethe Buchhandlung Teubig GmbH
Schweitzer Fachinformationen
Willstätterstrasse 15, 40549 Düsseldorf, GERMANY
Telephone: +49 (0) 211 49 8740 • Fax: +49 (0) 211 49 87428
Email: s.dehaan@schweitzer-online.de • Web site: http://www.goethebuch.de

HUNGARY
Librotade Ltd., Book Import
PF 126, 1656 Budapest, HUNGARY
Telephone: +36 1 257 7777 • Fax: +36 1 257 7472
Email: books@librotade.hu • Web site: http://www.librotade.hu

INDIA
Allied Publishers
1st Floor, Dubash House, 15, J.N. Heredi Marg, Ballard Estate, Mumbai 400001, INDIA
Telephone: +91 22 2261 7926/27 • Fax: +91 22 2261 7928
Email: alliedpl@vsnl.com • Web site: http://www.alliedpublishers.com

Bookwell
3/79 Nirankari, Delhi 110009, INDIA
Telephone: +91 11 2760 1283/4536
Email: bkwell@nde.vsnl.net.in • Web site: http://www.bookwellindia.com

ITALY
Libreria Scientifica "AEIOU"
Via Vincenzo Maria Coronelli 6, 20146 Milan, ITALY
Telephone: +39 02 48 95 45 52 • Fax: +39 02 48 95 45 48
Email: info@libreriaaeiou.eu • Web site: http://www.libreriaaeiou.eu

JAPAN
Maruzen Co., Ltd.
1-9-18 Kaigan, Minato-ku, Tokyo 105-0022, JAPAN
Telephone: +81 3 6367 6047 • Fax: +81 3 6367 6160
Email: journal@maruzen.co.jp • Web site: http://maruzen.co.jp

NETHERLANDS
Martinus Nijhoff International
Koraalrood 50, Postbus 1853, 2700 CZ Zoetermeer, NETHERLANDS
Telephone: +31 793 684 400 • Fax: +31 793 615 698
Email: info@nijhoff.nl • Web site: http://www.nijhoff.nl

Swets Information Services Ltd.
PO Box 26, 2300 AA Leiden
Dellaertweg 9b, 2316 WZ Leiden, NETHERLANDS
Telephone: +31 88 4679 387 • Fax: +31 88 4679 388
Email: tbeysens@nl.swets.com • Web site: http://www.swets.com

SLOVENIA
Cankarjeva Zalozba dd
Kopitarjeva 2, 1515 Ljubljana, SLOVENIA
Telephone: +386 1 432 31 44 • Fax: +386 1 230 14 35
Email: import.books@cankarjeva-z.si • Web site: http://www.mladinska.com/cankarjeva_zalozba

SPAIN
Diaz de Santos, S.A.
Librerias Bookshop • Departamento de pedidos
Calle Albasanz 2, esquina Hermanos Garcia Noblejas 21, 28037 Madrid, SPAIN
Telephone: +34 917 43 48 90 • Fax: +34 917 43 4023
Email: compras@diazdesantos.es • Web site: http://www.diazdesantos.es

UNITED KINGDOM
The Stationery Office Ltd. (TSO)
PO Box 29, Norwich, Norfolk, NR3 1PD, UNITED KINGDOM
Telephone: +44 870 600 5552
Email (orders): books.orders@tso.co.uk • (enquiries): book.enquiries@tso.co.uk • Web site: http://www.tso.co.uk

UNITED STATES OF AMERICA
Bernan Associates
4501 Forbes Blvd., Suite 200, Lanham, MD 20706-4391, USA
Telephone: +1 800 865 3457 • Fax: +1 800 865 3450
Email: orders@bernan.com • Web site: http://www.bernan.com

Renouf Publishing Co. Ltd.
812 Proctor Avenue, Ogdensburg, NY 13669, USA
Telephone: +1 888 551 7470 • Fax: +1 888 551 7471
Email: orders@renoufbooks.com • Web site: http://www.renoufbooks.com

United Nations
300 East 42nd Street, IN-919J, New York, NY 1001, USA
Telephone: +1 212 963 8302 • Fax: 1 212 963 3489
Email: publications@un.org • Web site: http://www.unp.un.org

Orders for both priced and unpriced publications may be addressed directly to:

IAEA Publishing Section, Marketing and Sales Unit, International Atomic Energy Agency
Vienna International Centre, PO Box 100, 1400 Vienna, Austria
Telephone: +43 1 2600 22529 or 22488 • Fax: +43 1 2600 29302
Email: sales.publications@iaea.org • Web site: http://www.iaea.org/books

14-11791

ISSN 1018–5518